

# High-Field EPR and ENDOR Studies of Protein Active Sites

Dissertation  
zur Erlangung des Doktorgrades  
der Naturwissenschaften

Vorgelegt beim Fachbereich 14  
der Johann Wolfgang Goethe-Universität  
in Frankfurt am Main

von  
Melanie M. Hertel  
aus Kaiserslautern

Frankfurt am Main 2006

D30

Vom Fachbereich Chemische und Pharmazeutische Wissenschaften der  
Johann Wolfgang Goethe-Universität Frankfurt als Dissertation angenommen.

Dekan: Prof. Harald Schwalbe

Gutachter: Prof. Thomas Prisner  
Prof. Clemens Glaubitz

Datum der Disputation: 17.11.2007





For You



# Contents

<b>1</b>	<b>Introduction</b>	<b>1</b>
	References . . . . .	8
<b>2</b>	<b>EPR and ENDOR for Structural Studies in Biological Systems</b>	<b>15</b>
	2.1 Theoretical Foundations of Magnetic Resonance . . . . .	15
	2.2 EPR Properties of Mn(II) . . . . .	19
	2.3 EPR and ENDOR Experiments . . . . .	21
	References . . . . .	26
<b>3</b>	<b>In Search of a Radical Intermediate in BCR</b>	<b>27</b>
	3.1 Introduction . . . . .	27
	3.2 Materials and Methods . . . . .	31
	3.3 Multifrequency EPR Studies of BCR . . . . .	33
	3.3.1 Pulsed high-field measurements at 180 GHz . . . . .	34
	3.3.2 CW X- and Q-band studies of BCR . . . . .	35
	3.3.3 Do the observations indicate the presence of a disulfide radical anion? . . . . .	41
	3.4 Summary and Discussion . . . . .	49
	3.5 Outlook . . . . .	54
	References . . . . .	55
<b>4</b>	<b>High-Field ENDOR Studies of the Catalytic Site in Ras</b>	<b>59</b>
	4.1 In Search of a Metal Ion Ligand at the Catalytic Site in Ras . . . . .	59
	4.1.1 Structure of the active site in Ras according to X-ray . . . . .	62
	4.1.2 Protein dynamics . . . . .	64
	4.1.3 Aim of the present study . . . . .	66
	4.2 Pulsed ENDOR at 94 GHz . . . . .	67
	4.3 In Search of an Additional Ligand . . . . .	68

---

4.3.1	In search of a phosphate ligand using $^{31}\text{P}$ -ENDOR . . . . .	68
4.3.2	In search of an amino acid ligand using $^{13}\text{C}$ -ENDOR . . . . .	71
4.4	Summary and Discussion . . . . .	75
4.5	Outlook . . . . .	78
	References . . . . .	79
<b>5</b>	<b>Implementing ENDOR at 180 GHz</b>	<b>85</b>
5.1	Introduction . . . . .	85
5.2	ENDOR Probe and Radio Frequency Circuit . . . . .	87
5.2.1	Design of the Resonator . . . . .	88
5.2.2	The Radio Frequency Field . . . . .	89
5.3	Characterization of the Setup and Performance for $^1\text{H}$ -ENDOR . . . . .	91
5.3.1	The ENDOR setup at 180 GHz . . . . .	92
5.3.2	Performance for $S = 1/2$ Systems: BDPA . . . . .	93
5.3.3	Performance for $S = 5/2$ Systems: Ras•Mn $^{2+}$ •GDP . . . . .	95
5.4	Summary and Outlook . . . . .	98
	References . . . . .	99
<b>6</b>	<b>Summary</b>	<b>103</b>
	References . . . . .	104
<b>7</b>	<b>Zusammenfassung</b>	<b>107</b>
	References . . . . .	112
<b>A</b>	<b>DFT Methods</b>	<b>115</b>
<b>B</b>	<b>Frequency Dependence of VSWR</b>	<b>117</b>
<b>C</b>	<b>Supporting Information for BCR Studies</b>	<b>119</b>
	<b>List of Figures</b>	<b>123</b>
	<b>List of Tables</b>	<b>125</b>
	<b>Abbreviations</b>	<b>127</b>
	<b>Acknowledgment</b>	<b>131</b>
	<b>Curriculum Vitae</b>	<b>133</b>



# Chapter 1

## Introduction

The present work deals with the identification of radical intermediates involved in the reduction of benzoyl-CoA catalysed by benzoyl-CoA reductase (BCR) as well as with structural studies of the active site in the protein Ras using electron paramagnetic resonance (EPR) and electron nuclear double resonance (ENDOR) techniques. The numerous potential advantages of using high fields and frequencies when performing ENDOR experiments, particularly on high-spin systems such as Mn(II), provided the motivation for implementing an ENDOR setup into a home-built pulsed EPR spectrometer operating at 180 GHz [1, 2].

In the past, EPR methods have been shown to be very useful when studying the structure and function of metalloprotein active sites (see e.g. [3, 4]). Hyperfine couplings between the electron spin and the nuclear spins of nuclei close to the metal center are a valuable source of information about catalytic mechanisms, structure, and coordination geometry of paramagnetic metal centers [5, 6]. The corresponding hyperfine coupling constants can either be derived from the splittings observed in the EPR spectrum or alternatively be obtained via double resonance techniques, such as ENDOR spectroscopy. In an ENDOR experiment, the nuclear magnetic resonance (NMR) spectrum of nuclei that interact with the electron spin of the paramagnetic center is recorded by detecting the change in the EPR signal intensity when exciting the nuclear transitions with a radiofrequency (RF) field.

When dealing with biological systems, one often runs into problems with overlapping EPR signals originating from more than one paramagnetic species present in the sample. In the past, the use of higher microwave (MW) frequencies along with pulsed (time-domain) methods has helped to disentangle EPR signals from

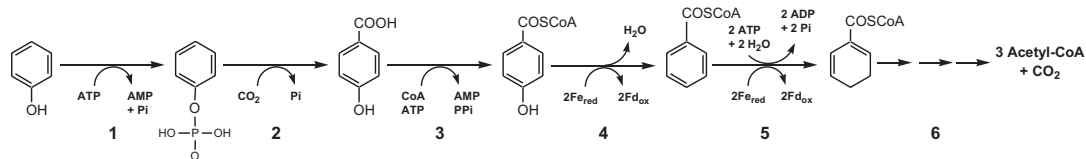


**Figure 1.1** Enzymatic reactions involved in phenol metabolism. Reactions catalyzed by (1) phenylphosphate synthase, (2) phenylphosphate carboxylase, (3) 4-hydroxybenzoate CoA ligase, (4) 4-hydroxybenzoyl-CoA reductase, (5) benzoyl-CoA reductase and (6) enzymes involved in modified  $\beta$ -oxidation reactions.

different paramagnetic centers, taking advantage of the increased spectral resolution at high fields and exploiting the time-domain opened by pulsed experiments, such that paramagnetic species can be separated according to their relaxation behaviour (for recent reviews and monographs see [7–11] and references therein). A key tool in the analysis of EPR spectra is the possibility to simulate the spectra at different microwave frequencies using EPR parameters consistent with a postulated molecular structure.

In the EPR studies described in Chapter 3, multifrequency EPR spectroscopy in combination with rapid freeze-quench (RFQ) techniques is used for identifying radical intermediates involved in catalysis of the reduction of benzoyl-CoA (BCoA) by benzoyl-CoA reductase. The biochemistry of BCR, a central enzyme in the anoxic metabolism of aromatic compounds in anaerobic bacteria [12–15], has been only studied in the anaerobic bacterium *Thauera aromatica*. In contrast to aerobic bacteria, anaerobic microbes use aromatic rings as carbon, energy, or nitrogen source by cleaving the aromatic ring via a reductive rather than an oxidative biochemistry. Since the discovery of anaerobic cleavage of mononuclear aromatics during the 1980s, three key intermediates through which mononuclear aromatic compounds are channeled, have been identified, which are benzoyl-CoA, resorcinol, and phloroglucinol [12]. The benzoyl-CoA pathway appears to be the most important one because a broad variety of compounds enter this path, among them phenol [12, 13, 16]. The initial steps in anaerobic phenol metabolism are shown in Figure 1.1 in which the key intermediate benzoyl-CoA is reduced to a non-aromatic cyclic dienoyl-CoA compound by benzoyl-CoA reductase via an ATP-dependent benzene ring dearomatization.

In analogy to the chemical Birch reduction [17], the reduction of the ring of BCoA by BCR was proposed to proceed via alternate steps of one-electron and

---

proton transfer, involving radical intermediates [18, 19]. In this reaction sequence, the first electron transfer to the aromatic substrate yields a radical anion and is considered rate-limiting requiring a redox-potential as low as  $-1.9$  V. It was shown that in order to overcome this high barrier, BCR couples the two-electron transfer from reduced ferredoxin to the aromatic ring to the hydrolysis of two molecules of ATP to ADP and  $P_i$  [20–22].

Previous single turnover studies of benzoyl-CoA reductase using RFQ EPR spectroscopy, in which radical intermediates were trapped by adding the competitive inhibitor 4-fluorobenzoyl-CoA (4-F-BCoA) to a solution containing one-electron reduced BCR, gave evidence for two transiently formed radical species [21, 23]. From these EPR and stopped-flow UV-Vis studies, the authors suggested a mechanistic model in which a disulfide radical anion was proposed to be a key intermediate in the aromatic ring reduction of BCoA by BCR [24]. The aim of the present EPR study was to identify and further characterize the nature of the radical intermediates postulated from previous EPR studies [21, 23]. Furthermore, the effect of  $^{33}\text{S}$ -labeling of the enzyme on the EPR line shape was used to test the hypothesis that a disulfide radical anion is involved in the reduction process of benzoyl-CoA.

In cases where the splitting of the EPR line caused by the hyperfine coupling is obscured by the line width, the information obtainable from the hyperfine couplings can often be recovered with ENDOR techniques. In comparison to conventional EPR, the resolution of ENDOR may be up to three orders of magnitude higher therefore allowing to detect and characterize electron nuclear hyperfine interactions for systems whose EPR spectra show no resolved hyperfine splittings. Therefore, ENDOR has proved to be a versatile tool for studying the structure and bonding at the active site of metalloproteins throughout the catalytic cycle [4, 25]. Information about the structure and bonding geometry at the active site can be obtained via ENDOR by extracting electron-nuclear hyperfine interaction tensors from the ENDOR spectra [5]. As soon as the point-dipole model (see Chapter 2) holds, the positions of nuclei surrounding the metal center can be calculated using the dipolar part of the hyperfine tensor such that enough geometric constraints are gained to define its structure. In combination with isotope labeling, it may then be possible to characterize every atom associated with a paramagnetic metalloenzyme active site.

As for EPR, many advantages arise when ENDOR is performed at high frequencies and fields [26–30]. Among them are the increased nuclear Zeeman reso-

lution, which leads to a separation of ENDOR signals from different nuclei and in particular improves the detectability of low- $\gamma$  nuclei, as well as the possibility to determine absolute signs of hyperfine coupling constants by exploiting the large thermal electron spin polarization at high fields and low temperatures [31, 32]. Furthermore, the ENDOR spectra may become significantly simplified due to the reduction of second-order-effects at high fields. In particular for high-spin systems, the use of high frequencies brings about several advantages. For Mn(II) in its high-spin  $^6S$  state which possesses a large zero-field splitting (ZFS) (see Chapter 2) and a small  $g$ -tensor the low-field EPR spectra are usually complicated because the Zeeman interaction is smaller than or comparable to the ZFS. At high fields, the EPR spectra are simpler since forbidden transitions are reduced and the central transitions ( $m_S = -\frac{1}{2} \leftrightarrow +\frac{1}{2}$ ) become narrow.

The above mentioned advantages were exploited in the present work for studying the structure at the active site in the human Ras (rat sarcoma) protein as described in Chapter 4. At the active site, a  $Mg^{2+}$  ion binds to guanosine-5'-diphosphate (GDP) in the inactive protein state and to guanosine-5'-triphosphate (GTP) in the active protein state (for recent reviews see [33–44]). As a member of the family of small G proteins (guanine nucleotide-binding proteins or GNBPs) Ras cycles between the GDP-bound inactive and the GTP-bound active state, acting as molecular switch in cellular signal transduction, regulating important processes such as differentiation, proliferation and apoptosis of cells [45]. In the GTP-bound form the protein interacts with and activates downstream targets, so-called "effector" molecules, which in turn regulate their activities within the cell. For the inactive protein to become activated, GDP has to be exchanged for GTP. This reaction requires guanine nucleotide exchange factors (GEFs) [46] to catalyze the release of usually tightly bound GDP, which is subsequently replaced by abundant cellular GTP. The protein is "switched off" again via hydrolysis of GTP either by the intrinsic GTPase-activity of Ras or by GTPase activating proteins (GAPs) [47–49]. This brings Ras•GTP back to its inactive GDP-bound form and results in effector release, thereby terminating downstream signaling [39]. Specific oncogenic variants of Ras contain point mutations at the active site which block the GTPase activity in the presence as well as in the absence of GAPs, leading to accumulation of the protein in the active form and thus contribute to tumor formation [50]. Since the exchange of nucleotides which controls the activation state of the protein occurs at the metal binding site of the protein, the knowledge of the structure at this site is in particular important for

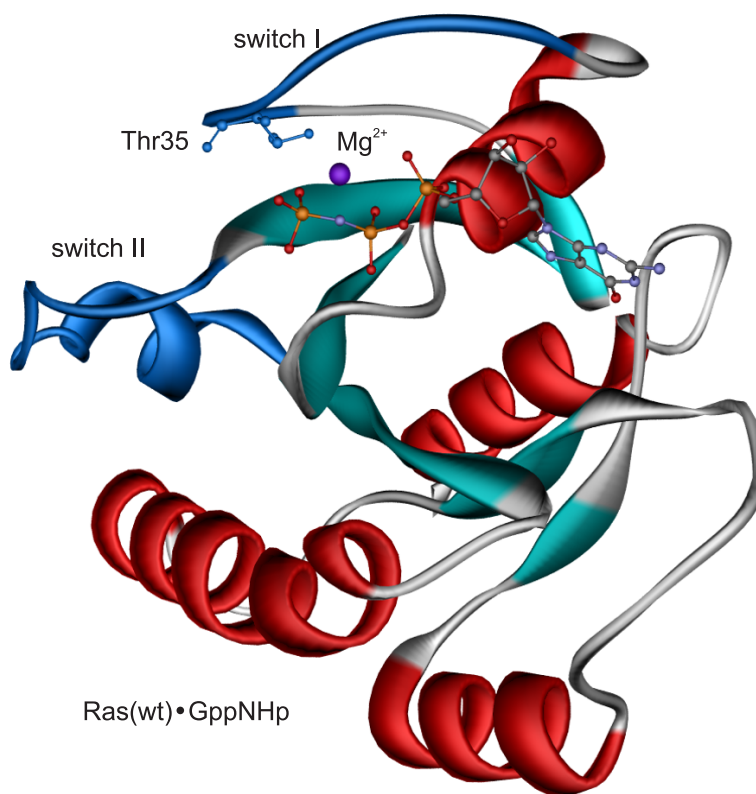


**Figure 1.2** Ribbon plot of Ras in the triphosphate form with the GTP analogue GppNHp according to Pai et al. [51]. The two regions in Ras where the major structural changes occur when the protein switches from the GTP-bound form to the GDP-bound form are the switch I and II regions shown in blue (see Chapter 4).

the understanding of tumor formation.

Surprisingly, the published crystal structures of Ras in the GDP- and GTP-bound forms (see Figure 1.2) did not reveal any difference in the ligation sphere of the metal ion in the wild-type protein in comparison to the oncogenic mutants [51–61]. The structure at the active site has been studied by several groups with EPR spectroscopical methods [62–71], after substitution of the diamagnetic  $\text{Mg}^{2+}$  ion with a paramagnetic  $\text{Mn}^{2+}$  ion. In particular, high-field EPR spectroscopical studies investigating the  $^{17}\text{O}$ -induced inhomogeneous broadening on the  $m_S = +\frac{1}{2} \leftrightarrow -\frac{1}{2}$  EPR transitions of the GDP complexes in  $^{17}\text{O}$ -labeled water displayed differences in the ligation sphere of the wild-type complex as compared to its oncogenic mutant Ras(G12V): only three water ligands were found in the former with respect to four in the G12V mutant [71]. Furthermore, previous  $^{31}\text{P}$ -

NMR studies had demonstrated that in liquid solution different conformational states in the GDP- as well as in the GTP-bound forms coexist [71, 72].

In the present study, high-frequency ENDOR spectroscopy was used to probe the ligand sphere of the metal ion in the GDP- and GTP-bound state. In combination with selective  $^{13}\text{C}$ - and  $^{31}\text{P}$ - isotope labeling the resonances of nuclei in the first ligand sphere of the metal ion were detected with high spectral resolution. The question about the existence of a free phosphate ion ligand or amino acid ligand that would replace a water molecule in the GDP-bound state of the wild-type protein was addressed using  $^{31}\text{P}$ - and  $^{13}\text{C}$ -ENDOR.

The numerous advantages of high-field ENDOR provided the motivation for implementing an ENDOR setup into a home-built pulsed EPR spectrometer operating at 180 GHz [1, 2] as described in Chapter 5. Therein, the incorporation of a broadbanded RF circuit for performing ENDOR experiments at 180 GHz is described and the performance of the setup for  $^1\text{H}$ -ENDOR is illustrated for the model system bisdiphenylene-phenyl-allyl (BDPA) using the Mims [73] as well as the Davies [74] pulse sequences. The applicability of the ENDOR setup to biological systems was tested using Ras • Mn $^{2+}$  • GDP.

## Publications and Conference Contributions

Parts of this work have also been published or presented in poster contributions<sup>1</sup> on conferences or meetings.

### Publications

*“High-Field 94 GHz ENDOR characterization of the metal binding site in wild type RasGDP and its oncogenic mutant G12V in frozen solution”*

Marina Bennati, Melanie M. Hertel, Jörg Fritscher, Thomas F. Prisner, Norbert Weiden, Roland Hofweber, Michael Spörner, Gudrun Horn, Hans-Robert Kalbitzer *Biochemistry* **2006**, *45*, 42–50.

*“Conformational studies of human H-Ras detected by High-field EPR, ENDOR and  $^{31}\text{P}$ -NMR Spectroscopy”*

Michael Spörner, Thomas F. Prisner, Marina Bennati, Melanie M. Hertel, Norbert Weiden, Thomas Schweins, Hans-Robert Kalbitzer *Magn. Reson. Chem.* **2005**, *43*, 74–83.

---

<sup>1</sup>The first author is the presenting author.

---

*“Pulsed 180-GHz EPR/ENDOR/PELOR Spectroscopy”*

Melanie M. Hertel, Vasyl P. Denysenkov, Marina Bennati, Thomas F. Prisner  
*Magn. Reson. Chem.* **2005**, *43*, 248–255.

*“Resolving Mn framework sites in large cage aluminophosphate zeotypes by high-field EPR and ENDOR spectroscopy”*

Dafna Arieli, Thomas F. Prisner, Melanie Hertel, Daniella Goldfarb  
*Phys. Chem. Chem. Phys.* **2004**, *6*, 172–181.

## Poster Contributions

*“Studies of the catalytic site in Ras with high-field ENDOR”*

M. M. Hertel, M. Bennati, N. Weiden, R. Hofweber, T. F. Prisner, K.-P. Dinse,  
M. Spörner, H.-R. Kalbitzer *24<sup>th</sup> GIF Meeting*, En Ghedi, Israel, 2005.

*“ENDOR and PELDOR at 180 GHz”*

M. M. Hertel, V. Denysenkov, M. Bennati, T. F. Prisner *Abschlußkolloquium des DFG Schwerpunkt-Programms 1051 High-field EPR in Biology, Chemistry and Physics*, Hünfeld, 2005.

*“Studies of the catalytic site in Ras with high-field ENDOR”*

M. M. Hertel, M. Bennati, N. Weiden, R. Hofweber, T. F. Prisner, K.-P. Dinse,  
M. Spörner, H.-R. Kalbitzer *Bunsentagung*, Frankfurt a. M., 2005.

*“High-field ENDOR studies of the catalytic site in Ras”*

M. M. Hertel, T. F. Prisner, N. Weiden, J. Fritscher, R. Hofweber, M. Spörner, H.-  
R. Kalbitzer, M. Bennati ", *European EPR Summer School*, Naurod (Wiesbaden),  
2005.

*“High-field ENDOR studies of the catalytic site in Ras”*

M. M. Hertel, T. F. Prisner, N. Weiden, J. Fritscher, R. Hofweber, M. Spörner,  
H.-R. Kalbitzer, M. Bennati *27<sup>th</sup> GDCh Magnetic Resonance Meeting*, Mainz,  
2005.

*“High-field ENDOR studies of the metal binding site of Ras in frozen solution”*

M. M. Hertel, N. Weiden, J. Fritscher, T. F. Prisner, M. Spörner, R. Hofweber,  
H.-R. Kalbitzer, M. Bennati *First European Conference on Chemistry for Life Sciences*, Rimini, Italy, 2005.

*“High-field ENDOR at 180 GHz”*

M. M. Hertel, M. Bennati, V. Denysenkov, T.F. Prisner *Workshop “High-Field Spectroscopy: Technology and Applications”*, Leiden, Netherlands, 2004.

*“Studies of the p21ras G protein with high-field ENDOR”*

M. M. Hertel, M. Bennati, N. Weiden, R. Hofweber, T.F. Prisner, K.-P. Dinse, M. Spörner, H.-R. Kalbitzer *26<sup>th</sup> GDCh Magnetic Resonance Meeting*, Aachen, 2004.

*“180 GHz EPR studies of Benzoyl-CoA reductase”*

M. M. Hertel, M. Penning de Vries, T. F. Prisner, H. Möbitz, M. Boll, M. Bennati *25<sup>th</sup> GDCh Magnetic Resonance Meeting*, Leipzig, 2003.

*“A high-field EPR spectrometer operating in pulsed and continuous-wave mode at 180 GHz”*

M. M. Hertel, O. Brüggemann, M. Rohrer, M. Bennati, T.F. Prisner *24<sup>th</sup> GDCh Magnetic Resonance Meeting*, Bremen, 2002.

*“Pulsed and continuous-wave EPR at 180 GHz”*

M. M. Hertel, O. Brüggemann, M. Rohrer, M. Bennati, T. F. Prisner *European EPR Summer School*, Retie, Belgium, 2002.

## References

- [1] Rohrer, M.; Brüggemann, O.; Kinzer, B.; Prisner, T. F. *Appl. Magn. Res.* **2001**, *21*, 257–274.
- [2] Hertel, M. M.; Bennati, M.; Denysenkov, V.; Prisner, T. *Magn. Res. Chem.* **2005**, *43*, 248–255.
- [3] Hoff, A. J. *Advanced EPR*; Elsevier, Amsterdam: 1990.
- [4] Hoffman, B. M. *Acc. Chem. Res.* **2003**, *36*, 522–529.
- [5] Abragam, A.; Bleaney, B. *Electron Paramagnetic Resonance of Transition Ions*; Dover Publications, New York: 1986.
- [6] Atherton, N. M. *Electron Spin Resonance*; Halstead, New York: 1973.
- [7] Bennati, M.; Prisner, T. F. *Rep. Prog. Phys.* **2005**, *68*, 411–448.



- [8] Grinberg, O.; Berliner, L. *Very High Frequency ESR/EPR*; volume 22 Plenum: New York, 2005.
- [9] Andersson, K. K.; Schmidt, P. P.; Katterle, B.; Strand, K. R.; Palmer, A. E.; Lee, S.-K.; Solomon, E. I.; Gräslund, A.; Barra, A.-L. *J. Biol. Inorg. Chem.* **2003**, *8*, 235–247.
- [10] Freed, J. H. *Annu. Rev. Phys. Chem.* **2000**, *51*, 655–689.
- [11] Prisner, T. F. *Adv. Magn. Opt. Res.* **1997**, *20*, 245–300.
- [12] Heider, J.; Fuchs, G. *Eur. J. Biochem.* **1997**, *243*, 577–596.
- [13] Harwood, C. S.; Burchardt, G.; Herrmann, H.; Fuchs, G. *FEMS Microbiol. Rev.* **1999**, *22*, 439–458.
- [14] Schink, B.; Philipp, B.; Müller, J. *Naturwissenschaften* **2000**, *87*, 12–23.
- [15] Gibson, J.; Harwood, C. S. *Annu. Rev. Microbiol.* **2002**, *56*, 345–369.
- [16] Schink, B.; Brune, A.; Schnell, S. In *Microbial degradation of natural compounds*; Winkelmann, G., Ed.; VCH, Weinheim: 1992.
- [17] Birch, A. J.; Hinde, A. L.; Radom, L. *J. Am. Chem. Soc.* **1980**, *102*, 3370–3376.
- [18] Koch, J.; Eisenreich, W.; Bacher, A.; Fuchs, G. *Eur. J. Biochem.* **1993**, *211*, 649–661.
- [19] Buckel, W.; Keese, R. *Angew. Chem. Int. Ed.* **1995**, *34*, 1502–1506.
- [20] Boll, M.; Fuchs, G. *Eur. J. Biochem.* **1995**, *234*, 921–933.
- [21] Boll, M.; Laempe, D.; Eisenreich, W.; Bacher, A.; Mittelberger, T.; Heinze, J.; Fuchs, G. *J. Biol. Chem.* **2000**, *275*, 21889–21895.
- [22] Boll, M.; Albracht, S. J. P.; Fuchs, G. *Eur. J. Biochem.* **1997**, *244*, 840–851.
- [23] Boll, M.; Fuchs, G.; Lowe, D. J. *Biochemistry* **2001**, *40*, 7612–7620.
- [24] Boll, M.; Fuchs, G. *Biol. Chem.* **2005**, *386*, 989–997.
- [25] Bennati, M.; Stubbe, J.; Griffin, R. G. *Appl. Magn. Reson.* **2001**, *21*, 389–410.

- [26] Rohrer, M.; Plato, M.; MacMillan, F.; Grishin, Y.; Lubitz, W.; Möbius, K. *J. Magn. Res.* **1995**, *116*, 59–66.
- [27] Disselhorst, J. A. J. M.; van der Meer, H.; Poluektov, O. G.; Schmidt, J. *J. Magn. Res.* **1995**, *116*, 183–188.
- [28] Gromov, I.; Krymov, V.; Manikandan, P.; Arieli, D.; Goldfarb, D. *J. Magn. Res.* **1999**, *139*, 8–17.
- [29] Bennati, M.; Farrar, C. T.; Bryant, J. A.; Inati, S. J.; Weis, V.; Gerfen, G. J.; Riggs-Gelasco, P.; Stubbe, J.; Griffin, R. G. *J. Magn. Res.* **1999**, *138*, 232–243.
- [30] Goldfarb, D.; Krymov, V. In *Very High Frequency ESR/EPR*, Vol. 22; Grinberg, O.; Berliner, L., Eds.; Plenum: New York, 2005.
- [31] Epel, B.; Manikandan, P.; Kroneck, H.; Goldfarb, D. *Appl. Magn. Res.* **2001**, *21*, 287–297.
- [32] Bennebroek, M.-T.; Schmidt, J. *J. Magn. Res.* **1997**, *128*, 199–206.
- [33] Wittinghofer, A.; Herrmann, C. *FEBS Lett.* **1995**, *369*, 52–56.
- [34] Maegley, K. A.; Admiraal, S. J.; Herschlag, D. *Proc. Natl. Acad. Sci. USA* **1996**, *93*, 8160–8166.
- [35] Wittinghofer, A.; Nassar, N. *TIBS* **1996**, *21*, 488–491.
- [36] Wittinghofer, A.; Scheffzek, K.; Ahmadian, M. R. *FEBS Lett.* **1997**, *410*, 63–67.
- [37] Wittinghofer, A. *Nature* **1998**, *394*, 317–320.
- [38] Sprang, S. *Curr. Opin. in Struct. Biol.* **1997**, *7*, 849–856.
- [39] Sprang, S. R. *Annu. Rev. Biochem.* **1997**, *66*, 639–678.
- [40] Geyer, M.; Wittinghofer, A. *Curr. Opin. Struct. Biol.* **1997**, *7*, 786–792.
- [41] Vetter, I. R.; Wittinghofer, A. *Science* **2001**, *294*, 1299–1304.
- [42] Takai, Y.; Sasaki, T.; Matozaki, T. *Physiol. Rev.* **2001**, *81*, 153–208.

- [43] Ehrhardt, A.; Ehrhardt, G. R. A.; Guo, X.; Schrader, J. W. *Experimental Hematology* **2002**, *30*, 1089–1106.
- [44] Scheffzek, K.; Ahmadian, M. R. *Cell. Mol. Life Sci.* **2005**, *62*, 3014–3038.
- [45] Wittinghofer, A.; Waldmann, H. *Angew. Chem. Int. Ed.* **2000**, *39*, 4173–4390.
- [46] Cherfils, J.; Chardin, P. *Trends. Biochem. Sci.* **1999**, *24*, 306–311.
- [47] Boguski, M. S.; McCormick, F. *Nature* **1993**, *366*, 643–654.
- [48] Scheffzek, K.; Ahmadian, M. R.; Wittinghofer, A. *Trends Biochem. Sci.* **1998**, *23*, 257–262.
- [49] Bernards, A. *Biochim. Biophys. Acta* **2003**, *1603*, 47–82.
- [50] Barbacid, M. *Annu. Rev. Biochem.* **1987**, *56*, 779–827.
- [51] Pai, E. F.; Krenzel, U.; Goody, R. S.; Kabsch, W.; Wittinghofer, A. *EMBO J.* **1990**, *9*, 2351–2359.
- [52] Tong, L.; deVos, A. M.; Milburn, M. V.; Brunger, A.; Kim, S.-H. *J. Mol. Biol.* **1991**, *217*, 503–516.
- [53] Milburn, M. V.; Tong, L.; de Vos, A. M.; Brünger, A.; Yamaizumi, Z.; Nishimura, S.; Kim, S.-H. *Science* **1990**, *247*, 939–945.
- [54] Schlichting, I.; Almo, S. C.; Rapp, G.; Wilson, K.; Petratos, K.; Lentfer, A.; Wittinghofer, A.; Kabsch, W.; Pai, E. F.; Petsko, G.; Goody, R. S. *Nature* **1990**, *345*, 309–315.
- [55] Prive, G. G.; Milburn, M. V.; Tong, L.; de Vos, A. M.; Yamaizumi, Z.; Nishimura, S.; Kim, S.-H. *Proc. Natl. Acad. Sci. USA* **1992**, *89*, 3649–3653.
- [56] De Vos, A. M.; Tong, L.; Milburn, M.; Matias, P. M.; Jancarik, J.; Noguchi, S.; Nishimura, K.; Miura, K.; Ohtsuka, E.; Kim, S. J. *Science* **1988**, *239*, 888–893.
- [57] Krenzel, U.; Schlichting, I.; Scherer, A.; Schumann, R.; Frech, M.; John, J.; Kabsch, W.; Pai, E. F.; Wittinghofer, A. *Cell* **1990**, *62*, 539–548.

- [58] Wittinghofer, F.; Krenzel, U.; John, J.; Kabsch, W.; Pai, E. F. *Environ. Health Perspect.* **1991**, *93*, 11–15.
- [59] Franken, S. M.; Scheidig, A. J.; Krenzel, U.; Rensland, H.; Lautwein, A.; Geyer, M.; Scheffzek, K.; Goody, R. S.; Kalbitzer, H.; Pai, E.; Wittinghofer, A. *Biochemistry* **1993**, *32*, 8411–8420.
- [60] Scheidig, A. J.; Sanchez-Lorente, A.; Lautwein, A.; Pai, E. F.; Corrie, J. E. T.; Reid, G. P.; Wittinghofer, A.; Goody, R. S. *Acta. Cryst.* **1994**, *D50*, 512–520.
- [61] Hall, B. E.; Bar-Sagi, D.; Nassar, N. *Proc. Natl. Acad. Sci. USA* **2002**, *99*, 12138–12142.
- [62] Feuerstein, J.; Kalbitzer, H. R.; John, J.; Goody, R. S.; Wittinghofer, A. *Eur. J. Biochem.* **1987**, *162*, 49–55.
- [63] Smithers, G. W.; Poe, M.; Latwesen, D. G.; Reed, G. H. *Arch. Biochem. Biophys.* **1990**, *280*, 416–420.
- [64] Latwesen, D. G.; Poe, M.; Leigh, J. S.; Reed, G. H. *Biochemistry* **1992**, *31*, 4946–4950.
- [65] Larsen, R. G.; Halkides, C. J.; Redfield, A. G.; Singel, D. J. *J. Am. Chem. Soc.* **1992**, *114*, 9608–9611.
- [66] Halkides, C.; Farrar, C. T.; Larsen, R. G.; Redfield, A. G.; Singel, D. J. *Biochemistry* **1994**, *33*, 4019–4035.
- [67] Halkides, C. J.; Farrar, C. T.; Redfield, A. G.; Singel, D. J. In *Biological Structure and Dynamics*, Vol. 1; Sarma, R. H.; Sarma, M. H., Eds.; Adenine Press: 1995.
- [68] Haller, M.; Hoffmann, U.; Schanding, T.; Goody, R. S.; Vogel, P. D. *J. Biol. Chem.* **1997**, *48*, 30103–30107.
- [69] Farrar, C. T.; Halkides, C. J.; Singel, D. J. *Structure* **1997**, *5*, 1055–1066.
- [70] Bellew, B.; Halkides, C. J.; Gerfen, G. J.; Griffin, R. G.; Singel, D. J. *Biochemistry* **1996**, *35*, 12186–12193.

- 
- [71] Rohrer, M.; Prisner, T.; Brüggmann, O.; Käss, H.; Spörner, M.; Wittinghofer, A.; Kalbitzer, H. R. *Biochemistry* **2001**, *40*, 1884–1889.
- [72] Geyer, M.; Schweins, T.; Herrmann, C.; Prisner, T. F.; Wittinghofer, A.; Kalbitzer, H. R. *Biochemistry* **1996**, *35*, 10308–10320.
- [73] Mims, W. B. *Proc. R. Soc. London* **1965**, *283*, 452–457.
- [74] Davies, E. *Phys. Lett.* **1974**, *47A*, 1–2.



# Chapter 2

## EPR and ENDOR for Structural Studies in Biological Systems

The present chapter provides a short introduction into the theoretical background of EPR and ENDOR spectroscopy along with the experimental techniques used in this thesis. The first part introduces the basic concepts of EPR and ENDOR spectroscopy and the spin Hamiltonian leading to the observed EPR and ENDOR frequencies. In the second part, the EPR properties of the high-spin system Mn(II) are briefly described along with the resulting EPR and ENDOR spectra. The last part deals with the EPR and ENDOR techniques employed in the present work.

### 2.1 Theoretical Foundations of Magnetic Resonance

A particle with charge  $q$  and mass  $m$  precessing in a plane yields an angular momentum  $\mathbf{L}$  which is connected with a magnetic moment  $\boldsymbol{\mu}$  via

$$\boldsymbol{\mu} = -\frac{q}{2m}\mathbf{L}. \quad (2.1)$$

Similarly, one can ascribe to an electron with charge  $e$  a magnetic moment  $\boldsymbol{\mu}_e$  which is connected to its "inner" angular momentum, its spin  $\mathbf{S}$ , via

$$\boldsymbol{\mu}_e = -\beta_e g_e \mathbf{S}, \quad (2.2)$$

where  $\beta_e$  is the Bohr magneton given by  $\beta_e = e\hbar/2m$ .  $g_e$  is the free-electron  $g$ -value or *Landé  $g$ -factor* ( $g_e = 2.002319\dots$ ), which is proportional to the size of

the gyromagnetic ratio between the electron spin  $\mathbf{S}$  and its magnetic moment  $\boldsymbol{\mu}_e$ .

When put into an external magnetic field  $\mathbf{B}_0$ , an electron with spin  $\mathbf{S}$  and magnetic moment  $\boldsymbol{\mu}_e$  therefore experiences a torque  $\mathbf{T} = \boldsymbol{\mu}_e \times \mathbf{B}_0$ , which causes the magnetic moment to precess about the direction of the external magnetic field with a *Larmor frequency*  $\omega_L$ . The size of this interaction is given by the potential energy

$$E_{\text{pot}} = -\boldsymbol{\mu}_e \mathbf{B}_0. \quad (2.3)$$

The Stern-Gerlach experiment had demonstrated that the spin of the electron is quantized, taking only two orientations in a static magnetic field. Its quantum mechanical properties are described by the spin quantum numbers  $s$  and  $m_s$ , with  $m_s = -s, -s + 1, \dots, +s$  given by  $s = \frac{1}{2}$  and  $m_s = \pm\frac{1}{2}$ . They are connected with the spin operator  $\hat{\mathbf{S}}$  as follows:

$$\hat{\mathbf{S}}_z |s, m_s\rangle = \hbar m_s |s, m_s\rangle \quad (2.4)$$

$$\hat{\mathbf{S}}^2 |s, m_s\rangle = \hbar^2 s(s+1) |s, m_s\rangle, \quad (2.5)$$

where  $z$  defines e.g. the direction of the external magnetic field. In an external magnetic field  $\mathbf{B}_0$ ,  $\hat{\mathbf{S}}_z$  is the projection of  $\mathbf{S}$  along the  $z$ -axis of  $\mathbf{B}_0$ , and  $\hat{\mathbf{S}}^2$  yields the length of  $\mathbf{S}$ . The size of the interaction of the spin  $\mathbf{S}$  with a magnetic field is given by the *Zeeman energy*

$$E_Z = -\beta_e g_e B_0 m_s. \quad (2.6)$$

The transition between the two spin states with  $m_s = \frac{1}{2}$  and  $m_s = -\frac{1}{2}$  can be excited by applying an alternating microwave field of the size

$$\Delta E = \beta_e g_e B_0 = h\nu_{\text{MW}}, \quad (2.7)$$

where  $\nu_{\text{MW}}$  is the frequency of the applied microwave field.

In an atomic or molecular environment, the electron spin  $\mathbf{S}$  experiences a *spin-orbit coupling* with the orbital angular momentum  $\mathbf{L}$ , whose size depends on the nucleus and the molecule and which causes the magnetic moment  $\boldsymbol{\mu}_e$  to be no longer parallel to its spin  $\mathbf{S}$ . Therefore, the electron Zeeman interaction is no longer independent of the orientation of the spin in the outer magnetic field, such that this orientation dependence is described through the  $g$ -tensor  $\mathbf{g}$ . Since



the orientation dependence of the  $g$ -tensor is strongly influenced by the molecular structure of the paramagnetic center as well as its environment e.g. in a protein, the knowledge of  $\mathbf{g}$  can provide valuable information about the nature and the structure of a paramagnetic species, as well as structural information about its environment. In solution, this orientation dependence is averaged out by the random tumbling motion, reducing the  $g$ -tensor to an orientation-independent isotropic  $g$ -value given by one third of the trace of  $\mathbf{g}$

$$g_{\text{iso}} = \frac{1}{3}(g_{xx} + g_{yy} + g_{zz}). \quad (2.8)$$

### The spin Hamiltonian

The energy levels of a paramagnetic center with one or more unpaired electrons coupled to several nuclei of ligated atoms which determine the frequencies observed in the EPR and the ENDOR spectrum are calculated from the *spin Hamiltonian*  $\hat{\mathcal{H}}$ :

$$\hat{\mathcal{H}} = \beta_e \mathbf{B} \mathbf{g}_e \hat{\mathbf{S}} + \hat{\mathbf{S}} \mathbf{D} \hat{\mathbf{S}} + \sum_j \hat{\mathbf{S}} \mathbf{A}^{(j)} \hat{\mathbf{I}}^{(j)} - \beta_n \sum_j \mathbf{B} g_n^{(j)} \hat{\mathbf{I}}^{(j)} + \sum_j \hat{\mathbf{I}}^{(j)} \mathbf{Q}^{(j)} \hat{\mathbf{I}}^{(j)}. \quad (2.9)$$

The first three terms dominate the observed frequencies in an EPR spectrum, whereas the last three terms govern the observed ENDOR frequencies. The first term represents the electronic Zeeman interaction described above. The second term is called the *zero-field splitting* (ZFS) interaction and accounts for the interaction with surrounding electron spins, described by the zero-field tensor  $\mathbf{D}$ . This term is only non-zero for systems with  $S \geq 1$ , i. e. systems containing more than one unpaired electron (such as Mn(II)), in which  $i$  electron spins couple to a total spin  $\mathbf{S} = \sum_i \mathbf{S}_i$  (see below). The third term describes the *hyperfine coupling*, the interaction of the electron spin with the nuclear spin of its own nucleus or with surrounding nuclei described by  $\mathbf{A}^{(j)}$  with  $\hat{\mathbf{I}}$  being the vector operator for the nuclear spin. The hyperfine tensor is of great importance for the interpretation of the ENDOR spectra since it often allows to extract the distance between the paramagnetic center and surrounding nuclei as explained below. The following term represents the *nuclear Zeeman interaction*, in analogy to the electron Zeeman interaction, with  $\beta_n$  being the nuclear magneton and  $g_n$  the nuclear  $g$ -value. The last term describes the *nuclear quadrupole interaction*

for systems with  $I > \frac{1}{2}$  given by the nuclear quadrupole tensor  $\mathbf{Q}$ . For the interpretation of the EPR and ENDOR spectra reported in the present work, the nuclear quadrupolar interaction does not play a role and will therefore not be considered any further.

### The hyperfine tensor

At sufficiently high fields where the hyperfine interaction is much smaller than the nuclear Zeeman interaction ( $\nu_n \gg \mathbf{A}^{(j)}$ ), the off-diagonal elements in the hyperfine tensors  $\mathbf{A}^{(j)}$  can be neglected (*high-field approximation*). The orientation of the hyperfine tensors  $\mathbf{A}^{(j)}$  with respect to  $\mathbf{g}$  are given by a set of *Euler angles*  $\alpha$ ,  $\beta$  and  $\gamma$  and in cases where  $\mathbf{A}^{(j)}$  and  $\mathbf{g}$  are collinear, the Euler angles are equal to zero such that the hyperfine tensor  $\mathbf{A}^{(j)}$  becomes diagonal in the principal axis system of the  $g$ -tensor. For a particular nucleus,  $\mathbf{A}$  can be decomposed into two components, the *isotropic* contribution  $a_{\text{iso}}$  and the *anisotropic* contribution  $\mathbf{T}$ . In its principal axis system,  $\mathbf{A}$  is given by the diagonal components

$$A_{xx} = a_{\text{iso}} + T_{xx}, \quad A_{yy} = a_{\text{iso}} + T_{yy}, \quad A_{zz} = a_{\text{iso}} + T_{zz}. \quad (2.10)$$

The isotropic term is proportional to the *spin density* at the nucleus, whereas the anisotropic term originates from the through-space dipolar interaction between the magnetic moments of the electron and the nuclear spin. For an axially symmetric hyperfine interaction,  $T_{xx} = T_{yy} = T_{\perp} = -T_{\text{dip}}$  and  $T_{zz} = T_{\parallel} = 2T_{\text{dip}}$ , such that

$$A_{\perp} = a_{\text{iso}} + T_{\perp} = a_{\text{iso}} - T_{\text{dip}} \quad (2.11)$$

$$A_{\parallel} = a_{\text{iso}} + T_{\parallel} = a_{\text{iso}} + 2T_{\text{dip}}. \quad (2.12)$$

At large enough distances between the electron and the nucleus, (e.g. for protons at  $r \geq 2.5 \text{ \AA}$  [1]), the electron  $i$  and the nucleus  $j$  can be considered as point dipoles (*point-dipole-model*) such that their distance can be extracted from the dipolar part  $T_{\text{dip}}$  of the hyperfine tensor  $\mathbf{A}^{(j)}$  via

$$T_{\text{dip}} = \frac{1}{r_{ij}^3} \cdot \frac{\mu_0 \rho_j}{4\pi} g_e \beta_e g_n \beta_n, \quad (2.13)$$

where  $\rho_j$  is the spin density on the respective nucleus. Therefore, as soon as the point-dipole-model holds, the distance between the electron and the  $j$ th nucleus can be calculated via

$$r_{ij} = \sqrt[3]{\frac{1}{T_{dip}} \cdot \frac{\mu_0 \rho_j}{4\pi} g_e \beta_e g_n \beta_n}. \quad (2.14)$$

Alternatively, when the distance is known Equation 2.13 allows one to extract the spin density  $\rho_j$  at the nucleus. In solution, the dipolar interaction is averaged out by the random tumbling motion, such that the hyperfine tensors  $\mathbf{A}^{(j)}$  only consist of the isotropic hyperfine component  $a_{\text{iso}}$  which is given by one third of the trace of  $\mathbf{A}^{(j)}$ :

$$a_{\text{iso}} = \frac{1}{3}(A_{xx}^{(j)} + A_{yy}^{(j)} + A_{zz}^{(j)}). \quad (2.15)$$

### The energy level diagram

The energy level diagram for the most simple case of an electron coupled to a nucleus with nuclear spin  $I = \frac{1}{2}$  assuming isotropic hyperfine interaction  $a_{\text{iso}} > 0$  is depicted in Figure 2.1 in the high-field approximation along with the allowed EPR and NMR transitions. The frequencies observed in the respective EPR and ENDOR spectra are centered around the electron and nuclear Larmor frequencies  $\nu_e$  and  $\nu_n$ , respectively, and split by the hyperfine coupling  $a_{\text{iso}}$ . In a more general case with  $S > \frac{1}{2}$  and with a non-isotropic hyperfine interaction described by  $\mathbf{A}^{(j)}$ , the resonance frequencies observed in the ENDOR spectrum of the  $j$ th nucleus are given by

$$\nu_j = |\nu_n + m_S \mathbf{A}^{(j)}|. \quad (2.16)$$

For  $\nu_n > \mathbf{A}^{(j)}$ , the observed resonances are centered around  $\nu_n$  and split by the hyperfine coupling constant and for  $\nu_n < \mathbf{A}^{(j)}$ , the two resonances emerge around  $\frac{\mathbf{A}^{(j)}}{2}$  with a splitting of  $\nu_n$ .

## 2.2 EPR Properties of Mn(II)

Although manganese occurs in the oxidation states  $-III$  to  $+VII$ , in the following only the EPR properties of Mn(II) will be described since the Ras protein investigated in this thesis contains Mn(II) (for reviews about EPR properties of Mn(II) in disordered systems see e.g. [2, 3]). The EPR properties of Mn(II) strongly depend on the distribution of unpaired electrons around the  $^{55}\text{Mn}$  nucleus and therefore its coordination environment. In the oxidation state  $+II$ , the electronic

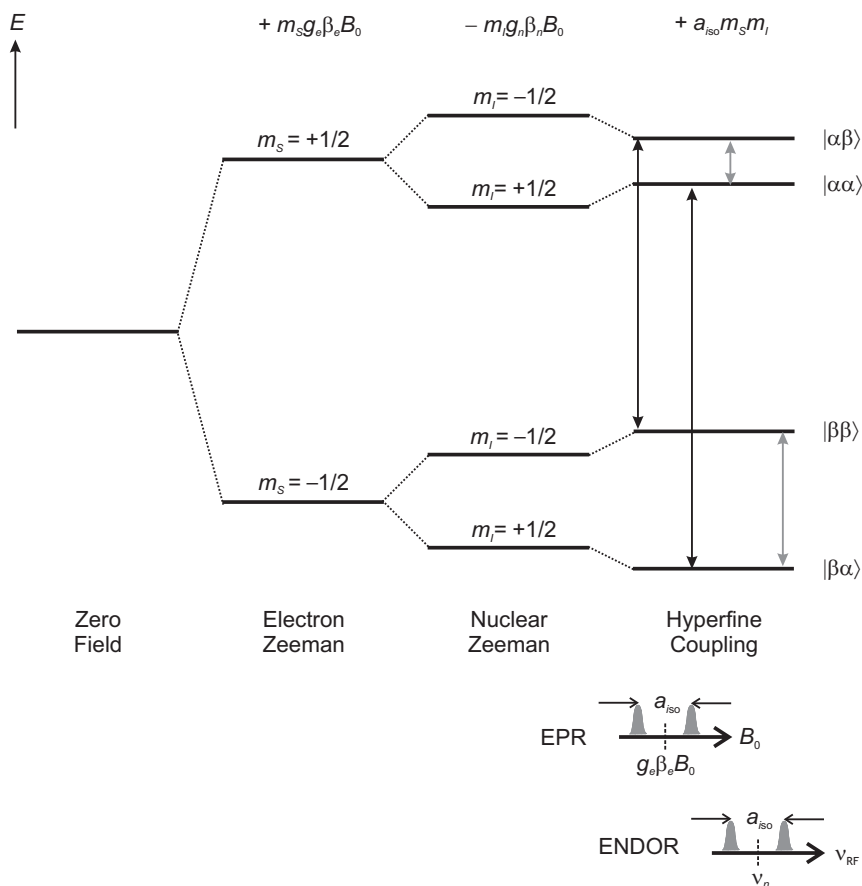


**Figure 2.1** Energy level diagram for an electron ( $S = \frac{1}{2}$ ) coupled to a nucleus with nuclear spin  $I = \frac{1}{2}$  assuming an isotropic hyperfine coupling  $a_{\text{iso}} > 0$  in the high-field approximation ( $\nu_n \gg |a_{\text{iso}}|$ ). The arrows indicate the allowed EPR (black) and NMR (gray) transitions, respectively, yielding the EPR and ENDOR spectra depicted schematically underneath.

configuration of the ion is  $3d^5$  and the five unpaired electrons fill the  $3d$  orbitals by one half. In the ground state, the orbital angular momentum is zero, and the resulting state is  ${}^6S_{5/2}$ , with spherical distribution of the electrons around the nucleus. When the ion is surrounded by ligands, this spherical distribution is removed due to the interaction between the  $d$  electrons, such that the  $3d$  orbitals are no longer degenerate. The resulting splitting between the orbitals is called the *ligand field splitting*, whose size determines whether the ion occurs in a *low-spin* state with total spin  $S = \frac{1}{2}$ , or in the *high-spin* state with  $S = \frac{5}{2}$ . However, most systems contain Mn(II) in its high-spin state, whereas the low-spin state is only found when very strong ligands are bound (e.g. CN or NO [2]).

The assymetry of the distribution of the electrons caused by the ligand field lifts the degeneracy of the electron spin levels even in the absence of a magnetic field (*zero-field splitting* (ZFS)). The reason for this can be found in the total spin being aligned with respect to the orbital angular momentum causing the three Kramers doublets ( $\pm\frac{5}{2}, \pm\frac{3}{2} \pm \frac{1}{2}$ ) to split even in the absence of an outer magnetic field. It is small for a perfect octahedral or tetrahedral distribution of identical ligands, and increases when the electronic symmetry around the ion is smaller than octahedral or tetrahedral. In a crystal field with octahedral symmetry, the electronic state of Mn(II) becomes  ${}^6A_{1g}$ .

The interaction of the electron spin  $S = \frac{5}{2}$  with the nuclear spin of  ${}^{55}\text{Mn}$   $I = \frac{5}{2}$  causes in an octahedral environment a hyperfine splitting of about  $-95$  G [2], resulting in 36 possible energy states (see Figure 2.2). The EPR spectrum then consists of five allowed electron transitions ( $\Delta m_S = \pm 1$ ) each split into a sextet of hyperfine transitions ( $\Delta m_I = 0$ ), resulting in 36 allowed transitions. At high fields where the size of the ZFS is small in comparison to the Zeeman energy, the EPR spectrum is dominated by the central  $m_S = +\frac{1}{2} \leftrightarrow m_S = -\frac{1}{2}$  EPR transition with resolved hyperfine transitions, whereas the higher EPR transitions are not resolved but form a broad background signal (see Figure 2.2, left hand side). This allows to record an ENDOR spectrum exciting one of the central transitions, therefore facilitating the interpretation of the ENDOR spectra (see Figure 2.2, right hand side).

## 2.3 EPR and ENDOR Experiments

In the following, the EPR and ENDOR techniques employed in the present thesis will be briefly introduced. CW and pulsed EPR methods were used to separate EPR signals from different radical intermediates in BCR (see Chapter 3) according to their relaxation behaviour and to resolve their  $g$ - and hyperfine tensor components. In order to discriminate between  $g$ -anisotropy and hyperfine couplings it is mostly advantageous to measure at different microwave frequencies, since the former depends on the magnetic field strength whereas the latter does not. For detecting hyperfine couplings, as a first approach one often uses conventional CW X-band (9 GHz) EPR spectroscopy. However, in cases where the hyperfine coupling is too small to be resolved in a field-swept EPR spectrum, they may be measured with hyperfine spectroscopy techniques, such as ESEEM (electron-

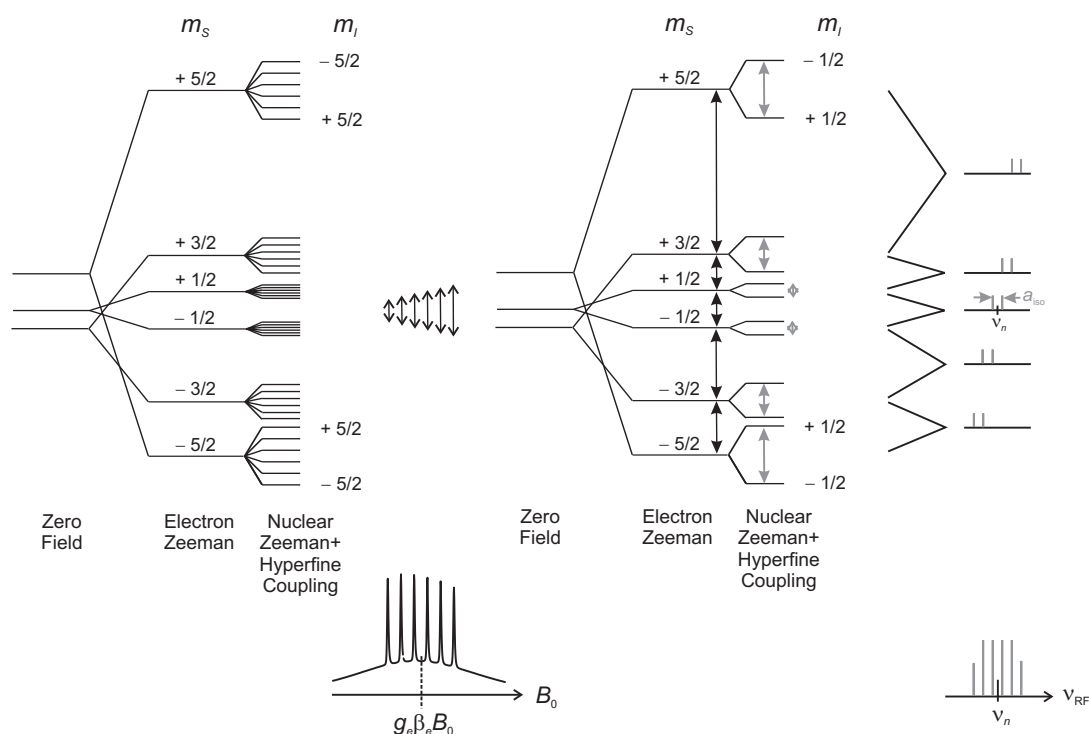


**Figure 2.2** Schematic representation of the electron spin energy levels of Mn(II) with hyperfine coupling to a nuclear spin  $I = \frac{5}{2}$  such as  $^{55}\text{Mn}$  (left) and to a nucleus with  $I = \frac{1}{2}$  (e.g.  $^1\text{H}$ ) (right), both with an isotropic hyperfine coupling  $a_{\text{iso}} > 0$ , at zero field and at high field in a noncubic environment. Left: At high fields, the resulting EPR spectrum (bottom left, experimental spectrum) is dominated by the six hyperfine transitions of the central  $m_S = +\frac{1}{2} \leftrightarrow -\frac{1}{2}$  EPR transition whereas the higher transitions form the broad background signal. Right: For simplicity, the hyperfine energy levels from the  $^{55}\text{Mn}$  nucleus are not shown. The frequencies in the ENDOR spectrum (bottom right) appear at  $\nu_j = |\nu_n + m_S a_{\text{iso}}|$ .

spin echo envelope modulation) or HYSORE (hyperfine sublevel correlation) spectroscopy, or alternatively via ENDOR (electron nuclear double resonance) spectroscopy. The latter was used in the present work to detect the hyperfine couplings of nuclei ligated to Mn(II) in Ras (see Chapter 4), employing the Mims and the Davies ENDOR sequence introduced below.

### Separation of overlapping EPR signals according to their relaxation behaviour

One distinguishes between *longitudinal relaxation* and *transverse relaxation*, which are associated with the relaxation times  $T_1$  and  $T_2$ , respectively. The former is connected with the lifetime of the electron spin state, which is coupled to the en-

ergy exchange with the surrounding (*spin-lattice relaxation*), proceeding through different mechanisms depending on the environment. In contrast, processes leading to transverse relaxation are not associated with an exchange of energy but with a loss of coherence, originating from spin flips (*spin-spin relaxation*).

In a CW EPR experiment, the relaxation behaviour of the observed paramagnetic center is connected with the product  $T_1 \times T_2$ , rendering the separation of the signals according to their longitudinal relaxation and transverse relaxation time difficult. In such an experiment, the change of temperature as well as the use of different microwave power may help to separate the observed EPR signals according to the product  $T_1 \times T_2$ . In contrast, using pulsed EPR techniques allows the separation of EPR signals from different paramagnetic centers according to their longitudinal as well as their transverse relaxation behaviour. Separation of overlapping signals according to their longitudinal relaxation times  $T_1$  is in principle possible using the *saturation recovery*, *inversion recovery* as well as the *stimulated echo* sequences (see Figure 2.3), by recording the echo intensity depending on the pulse separation time  $T$ , while all other experimental parameters are kept constant. For separation of EPR signals according to their transverse relaxation times  $T_2$  the so-called *Hahn-echo* sequence is used, where the pulse spacing time  $\tau$  is changed, while the pulse lengths are kept fixed (see Figure 2.3). It should be noted that in practice, processes like *spin diffusion*, *spectral diffusion* as well as anisotropic relaxation behaviour render the separation of EPR signals even with pulsed techniques demanding. The interested reader is referred to the many articles and monographs which have been dedicated to this subject (see e.g. [4, 5]).

### Pulsed ENDOR sequences

In an ENDOR experiment, the NMR spectrum of nuclei coupled to the unpaired electron is obtained by recording the change of the echo intensity in dependence of the applied RF frequency. In such a manner, hyperfine couplings which are buried under the EPR line width in the EPR spectrum can often be recovered. In comparison to an EPR experiment, the number of observed lines in an ENDOR spectrum is reduced from  $2^N$  to  $2N$  (with  $N$  being the number of equivalent coupled nuclei), yielding an increased resolution. The two most frequently used pulse sequences for recording ENDOR spectra are the Mims [6] as well as the Davies [7] ENDOR sequence, which may be separated into three periods, the

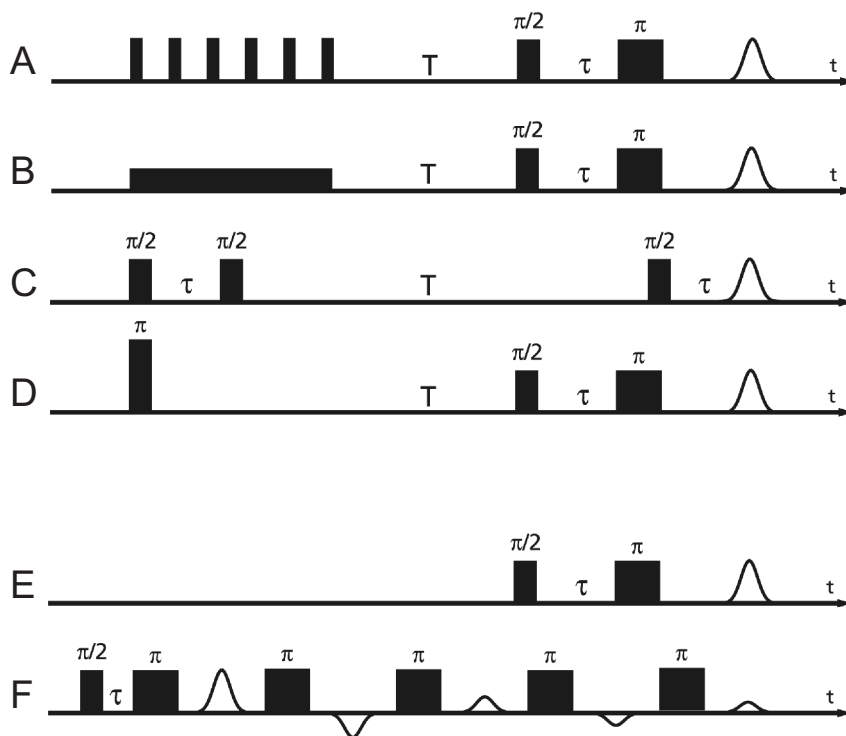


**Figure 2.3** Pulse sequences which may be used for separating overlapping EPR signals according to their longitudinal relaxation times  $T_1$  (A, B, C and D) or their transverse relaxation times  $T_2$  (E and F). (A) *Saturation-recovery sequence* with picket-fence preparation, (B) *saturation recovery sequence* with long saturation pulse, (C) *stimulated echo sequence*, (D) *inversion recovery sequence*, (E) *two-pulse echo decay (Hahn-echo sequence)*, (F) *Carr-Purcell pulse sequence*. Figure adapted from T. Maly, with kind permission.

*preparation, mixing, and the detection period* (see Figure 2.4). A more detailed theoretical background of pulsed ENDOR techniques is provided e.g. in Refs. 8–10.

The detection of an ENDOR spectrum is most easily explained for the Davies ENDOR sequence which is based on transfer of spin polarization (see Figure 2.4). In this experiment, a MW  $\pi$ -pulse is first applied to excite an electron transition inverting the electron population of the respective EPR transition. Thereafter, an RF  $\pi$ -pulse is applied and its frequency swept in order to record the NMR spectrum. A change in the echo amplitude, the *ENDOR effect*, does only occur when the RF frequency is on-resonance with one of the NMR transitions. The ENDOR effect is recorded by integrating over the echo intensity using the



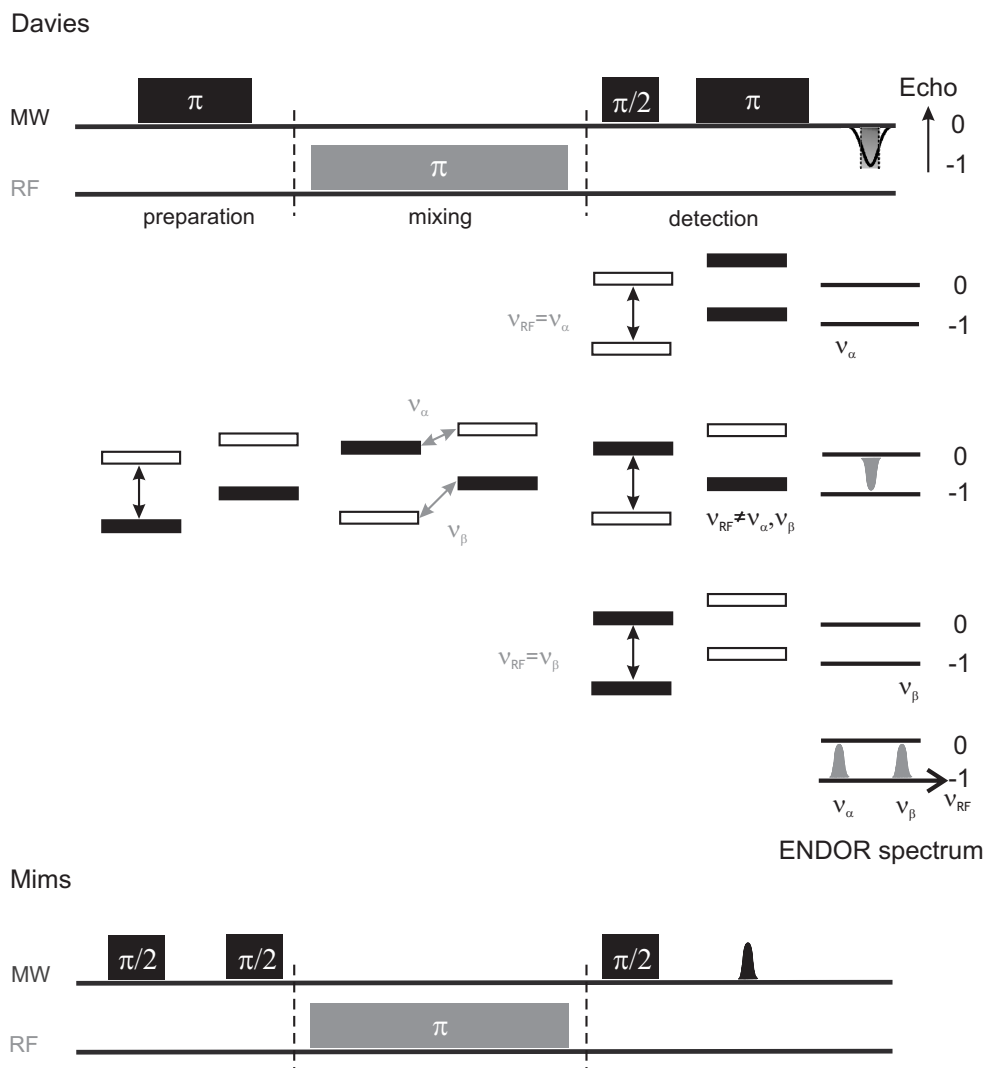


**Figure 2.4** Schematic representation of the Davies (top) and Mims (bottom) ENDOR, along with the respective energy level diagram for an electron coupled to a nuclear spin with  $I = \frac{1}{2}$ . The arrows indicate the excited EPR (black) and NMR (grey) transitions for recording the Davies ENDOR spectrum, which is obtained by integrating over the EPR echo intensity (indicated by the shaded area) as a function of the RF frequency (see text).

detection sequence  $\pi/2 - \pi$ . The Davies ENDOR sequence is most suited for large hyperfine couplings ( $A > 5$  MHz), since it is based on the selective excitation of the electron transitions. Therefore, for an optimum Davies ENDOR effect long MW pulses are necessary, which can be obtained by decreasing the MW power.

In contrast, the Mims ENDOR experiment is based on coherence transfer, employing MW  $\pi/2$ -pulses, and is used when small hyperfine couplings ( $A < 5$  MHz)

are expected. For a successful Mims ENDOR experiment, unselective excitation of the electron transitions is necessary which can only be achieved with sufficient MW power. The Mims ENDOR sequence suffers from blind spots originating from the polarization pattern created on the EPR spectrum by the two preparation pulses. The distance between the blind spots in the ENDOR spectrum depends on the pulse spacing time  $\tau$ , with blind spots showing up at frequencies  $\nu = 2n\pi/\tau$ .

## References

- [1] Goldfarb, D.; Arieli, D. *Annu. Rev. Biophys. Biomol. Struct.* **2004**, *33*, 441–468.
- [2] Reed, G. H.; Markham, G. D. *Biol. Magn. Res.* **1984**, *6*, 73–142.
- [3] Misra, S. K. *Appl. Magn. Res.* **1996**, *10*, 193–216.
- [4] Poole, C. P.; Farach, H. A. *Relaxation in Magnetic Resonance*; Academic Press, N. Y. and London: 1971.
- [5] Atkins, P. W. *Electron Spin Relaxation in Liquids*; Plenum Press, New York and London: 1972.
- [6] Mims, W. B. *Proc. R. Soc. London* **1965**, *283*, 452–457.
- [7] Davies, E. *Phys. Lett.* **1974**, *47A*, 1–2.
- [8] Grupp, A.; Mehring, M. In *Modern Pulsed and CW Electron Spin Resonance*; Kevan, L.; Bowman, M., Eds.; Wiley: New York, 1990.
- [9] Gemperle, C.; Schweiger, A. *Chem. Rev.* **1991**, *91*, 1481–1505.
- [10] Schweiger, A. *J. Chem. Soc. Faraday Trans.* **1995**, *91*, 179–190.

## Chapter 3

# In Search of a Radical Intermediate in Benzoyl-CoA Reductase with the Aid of Multifrequency EPR

### 3.1 Introduction

Benzoyl-CoA (BCoA) arises as the most prevalent intermediate in the degradation of a diversity of aromatic molecules to acetyl-CoA and carbon dioxide under anaerobic conditions [1]. This compound becomes reduced by benzoyl-CoA reductase (BCR), a central enzyme in the anoxic metabolism of aromatic compounds in anaerobic bacteria. BCR catalyzes the two-electron reduction of benzoyl-CoA to cyclohexa-1,5-diene-1-carbonyl-CoA by reduced ferredoxin [1–7]. In analogy to the chemical Birch reduction [8], the reduction of the ring has been postulated to proceed via alternate steps of one-electron and proton transfer, involving radical intermediates [3, 9]. In this reaction sequence, the first electron transfer to the aromatic substrate yields a radical anion and is considered rate-limiting requiring a redox potential as low as  $-1.9$  V. It was shown that in order to overcome this high barrier, BCR couples the two-electron transfer from reduced ferredoxin to the aromatic ring to the hydrolysis of two molecules of ATP to ADP and  $P_i$  [4, 5, 10].

So far, the biochemistry of the iron-sulfur flavoprotein BCR has exclusively been studied in the denitrifying bacterium *Thauera aromatica*. The enzyme is a 170 kDa heterotetramer [11] with 49, 48, 44 and 29 kDa subunits containing three cysteine-coordinated  $[4Fe\ 4S]^{+1/+2}$  clusters as sole redox cofactors with

$E' < -500$  mV [12]. The architecture of BCR is very similar to that of nitrogenase and remarkable analogies between the ATP-dependent reductions catalyzed by benzoyl-CoA reductase and nitrogenase are found. Both enzymes overcome energetic barriers by coupling electron transfer to a stoichiometric ATP hydrolysis. Notably, in both nitrogenase and BCR transfer of a single electron to active site redox centers does not necessarily depend on ATP hydrolysis. The crystal structure of BCR has so far not been solved, however, amino acid sequence comparison with the monodimeric activating enzyme (activase) of 2-hydroxyglutaryl-CoA dehydratase from *Acidaminococcus fermentans* revealed that the 29 and 49 kDa subunits of BCR ligate a single [4Fe-4S] cluster which is coordinated by two cysteines of each subunit [13], analogous to nitrogenase. The two other subunits (44 and 48 kDa) harbour the two other [4Fe-4S]<sup>+1/+2</sup> clusters which are assigned to the aromatic ring reduction module, binding one benzoyl-CoA. The natural electron donor of the enzyme is a ferredoxin from *Thauera aromatica*, a 9 kDa protein containing 8 mole iron/mol and 8 mole inorganic sulfur/mol. EPR and Mössbauer spectroscopic studies could only identify two of the three clusters (termed cluster I and II) as [4Fe-4S]<sup>+</sup> clusters in BCR reduced with dithionite or deazaflavine/light [12]. In these studies, it was proposed that an ATP hydrolysis switch converts one [4Fe-4S]<sup>+1/+2</sup> cluster from the  $S = \frac{1}{2}$  low-spin into the unusual  $S = \frac{7}{2}$  high-spin state [12, 14]. Calculations revealed that such a switch could lower the redox potential of a [4Fe-4S]<sup>+1</sup> cluster by up to  $-500$  mV [15].

In order to overcome the stability of the aromatic ring, BCR has to provide a very low-potential electron donor and at the same time shield this electron donor from an environment where protons are present in exuberance. In chemistry, these problems are solved by the *Birch reduction* of benzene (see Figure 3.1), which uses sodium as electron donor in liquid ammonia, serving as solvent for the solvatised electrons. Reduction to a cyclohexadiene proceeds in distinct, alternating electron transfer and protonation steps. The rate-limiting step in chemical and biochemical reduction of the aromatic ring is the formation of a radical anion by the donation of a first electron.

In biological systems, electron transfer reactions usually occur between  $E'^{\circ}$ -values from  $+800$  mV to approximately  $-500$  mV. At the low potential limit, usually [4Fe 4S]<sup>+1/+2</sup> clusters with redox potentials from  $-100$  to  $-600$  mV are involved in electron transfer processes. Some enzymatic processes, however, require electron transfer steps at redox potentials below the range accessible by usual [4Fe-4S]<sup>+1/+2</sup> clusters. For these cases, nature has evolved unique designs of

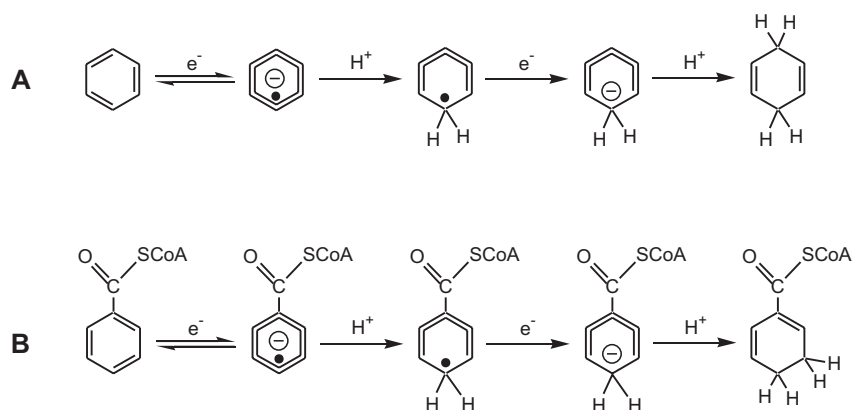


**Figure 3.1** "Chemical" Birch reduction of benzene (A) and "biological" Birch reduction of benzoyl-CoA (B), which is an enzymatic reaction. In both reactions, the rate-limiting step is the first electron transfer yielding a radical anion.

complex metalloclusters containing Fe, S, Ni or Mo [16]. S-Adenosyl-methionine (SAM)/radical enzymes comprise another group of enzymes with an unusual [4F-4S] cluster involved in low-potential redox chemistry [17]. In these enzymes, the unfavorable electron transfer from a  $[4Fe-4S]^{+1}$  cluster to the sulfonium cation of SAM is facilitated by direct coordination of the SAM molecule to the cluster enabling an inner sphere electron transfer [18–20]. Finally, low-potential redox reactions can also be achieved by the unique redox chemistry of sulfur radicals: In the R1-subunit of class I ribonucleotide reductases a disulfide radical anion species was proposed as intermediate and was observed in a E441Q mutant of R1 [21, 22]. Such a species has an extremely low redox potential and is suitable for reduction of a ketone to a 4'-ketyl at the ribose moiety.

In order to gain mechanistic insight about potential radical intermediates, two methods have been frequently used, which are stopped-flow (SF) UV-Vis spectroscopy [23] and rapid freeze-quench (RFQ) EPR spectroscopy [24]. In many cases, use of active-site mutants or alternative substrates has greatly facilitated detection of intermediates, which were quenched on the second time scale for analysis by EPR spectroscopy [25]. The combination of RFQ and EPR spectroscopy was also used in single turnover studies of BCR for identifying potential radical intermediates [5, 14]. In these studies, putative radical intermediates were trapped by adding the competitive inhibitor 4-fluorobenzoyl-CoA (4-F-BCoA) to a solution containing one-electron reduced BCR, which gave evidence for two

transiently formed radical species [5]. The inhibitor prevents the electron transfer to the benzene ring and using 4-F-BCoA as inhibitor the reduction rate was reduced to less than 1% [26]. The decrease of signal intensity of an  $S = \frac{7}{2}$  [4Fe-4S]<sup>2+</sup> cluster in the CW X-band EPR spectra of inhibited BCR was correlated with the rise of two low-field shifted isotropic EPR signals from a radical species in the late phase of the catalytic cycle [14]. The difference EPR spectrum obtained from subtracting spectra of samples recorded in the late phase of the catalytic cycle (2 s) minus spectra acquired at an earlier time point (0.2 s) revealed isotropic EPR signals at  $g_{av} = 2.015$  and a minor one at  $g_{av} = 2.03$  [14]. Due to the fast relaxation of the former EPR signal with maximum intensity around 20 K and since  $g_{av}$ -values  $\leq 2.01$  are characteristic for sulfur-centered radical species [27], this signal was proposed to be due to a disulfide radical anion derived from cysteines [6]. Along with the EPR studies of the cluster signals, these observations suggested the formation of a sulfur-centered protein radical intermediate derived from cysteines, located in the proximity of an [4Fe-4S] cluster.

The aim of the present EPR study was to identify and further characterize the nature of the radical intermediates found by previous CW X-band EPR studies and to provide further evidence for the involvement of a disulfide radical anion in the reduction process of BCoA via BCR. The only disulfide radical anion involved in enzymatic catalysis so far detected was found by Lawrence et al. using high-field EPR spectroscopy [22]. In comparison to conventional X-band EPR spectroscopy, high-field EPR offers the crucial advantage of increased spectral resolution, which is particularly useful for radicals with small  $g$ -anisotropy such as disulfide radical anions. In the present study, pulsed high-field EPR at 180 GHz was chosen as first attempt for resolving the  $g$ -values of the 4-F-BCoA-induced species around  $g = 2.015$ . However, the presence of more than one radical species in the inhibited enzyme solution as observed in the high-field EPR spectra rendered the interpretation of the observed spectral features demanding. Therefore, in addition CW EPR spectroscopy at X- and Q-band (9.4 and 34 GHz, respectively) was performed along with pulsed EPR measurements at Q-band. At X-band, where the spectra are dominated by the hyperfine interaction rather than by  $g$ -anisotropy, the effect of isotope <sup>33</sup>S-labeling on the line shape of the EPR signals was investigated (<sup>33</sup>S nuclear spin  $I = \frac{3}{2}$ ). Furthermore, in order to better resolve the  $g$ -values of the observed radical species, CW and pulsed Q-band EPR spectra were acquired for the labeled and unlabeled enzyme.

## 3.2 Materials and Methods

### Sample preparation

Sample preparation was performed by members of the group of Dr. Matthias Boll, from the Institut für Mikrobiologie, Universität Freiburg. The 4-F-BCoA inhibited samples of unlabeled BCR for high-field EPR measurements were prepared under aerobic conditions by Dr. Henrik Möbitz and under anaerobic conditions by Dr. Matthias Boll. Unlabeled and  $^{33}\text{S}$ -labeled BCR samples for CW X- and Q-band EPR measurements were prepared under anaerobic conditions by Jörg Johannes.

The enzyme was anaerobically oxidized by thionine and desalted as described earlier on in Ref. 26. Unlabeled and  $^{33}\text{S}$ -labeled samples were reduced by 0.5 and 1.0 equivalent of a freshly prepared dithionite stock solution (10 mM in reaction buffer), where the concentration of added dithionite was  $\frac{1}{4}$  and  $\frac{1}{2}$  the enzyme concentration, respectively. The reaction yield was estimated to be approximately 10%.  $^{33}\text{S}$ -labeling of the enzyme was achieved by oxidising elementary sulfur to  $\text{SO}_3^{2-}$  by heating elementary sulfur, leading the produced gas ( $\text{SO}_2$ ) through a gas distillery bottle containing NaOH. The content of the bottle was then autoclaved and added to the fermenter. In order to avoid contaminations from  $^{32}\text{S}$ , the precultur was centrifuged and the cells washed with sulfur-free medium. The reaction was started by addition of 5 mM MgADP and 1 mM or 0.5 mM 4-F-BCoA from appropriate anaerobically prepared stock solution in reaction buffer. Manual freeze quenching was achieved by a home-built manual freeze quenching apparatus consisting of two syringes, such that the two solutions were anaerobically mixed and subsequently frozen in liquid nitrogen for CW X- and Q-band measurements within 1–4 min. For handling of G-band samples see below.

### Multifrequency EPR spectroscopy

**Continuous wave X-band** CW X-band EPR spectra were recorded in Frankfurt on a Bruker spectrometer E500 using a standard ST 8338-R2 cavity (Bruker). The temperature was varied from 10 to 80 K, as indicated in the figure captions. Temperature control in the continuous flow cryostat (ESR 900, Oxford Instruments) was achieved via a temperature controller ITC 503 (Oxford Instruments). The magnetic field was determined with a Hall probe at the position of the sample while the frequency was measured with a frequency counter (6054D,

Systron Donner). The frequency was calibrated via subsequently measuring a DPPH sample, which possesses a nearly isotropic  $g$ -value of 2.0037. The modulation amplitude was optimised to 2 G and a modulation frequency of 100 kHz was used in each measurement. The microwave power was optimized in preliminary measurements to 2 mW.

**Continuous wave Q-band** The CW Q-band EPR spectra were measured in collaboration with Dr. Peter Höfer at Bruker Biospin GmbH in Karlsruhe, on a Bruker spectrometer E500 10/12 using a Q-band resonator ER 5106QT (Bruker). The temperature was kept at 20 K for all measurements, for which temperature control in the continuous flow cryostat (ER 4118CF) was achieved via a temperature controller ITC 503 (Oxford Instruments). As with the X-band measurements, the magnetic field was determined with a Hall probe, whereas the microwave frequency was measured with a frequency counter (5352B, Hewlett-Packard). The modulation amplitude was 2 G and the modulation frequency 100 kHz with a microwave power of 2.3 mW. The conversion time was 50 ms and the time constant 20 ms.

**Pulsed Q-band** Pulsed Q-band EPR spectra were measured in collaboration with Dr. Christian Teutloff in the group of Prof. Robert Bittl at the Free University of Berlin on a Bruker spectrometer E580 using a Bruker Q-band EPR/ENDOR probehead equipped with a dielectric ring resonator (EN 5107D2). The temperature was varied from 5 to 20 K, as indicated in the figure captions, and controlled via a temperature controller integrated in the continuous flow cryostat (CF935, Oxford Instruments). Echo-detected field-swept spectra were obtained using a two-pulse sequence ( $\pi/2 - \pi$ ) with  $\pi/2$  pulse lengths of 20 ns and a pulse spacing of  $\tau = 300$  ns with variable shot repetition time as indicated in the figure captions.

**Pulsed G-band** 180 GHz EPR spectra were acquired on a home-built high sensitivity pulse EPR spectrometer [28, 29]. The use of a high quality ( $Q_{\text{loaded}} = 1000\text{--}2000$ ) cylindrical  $\text{TE}_{011}$  cavity in combination with a corrugated waveguide for microwave transmission and an incident power level at the resonator of about 15 mW allowed for typical  $\pi/2$ -pulse lengths of 50–70 ns. The absolute spin sensitivity was determined to be about  $10^{10}$  spins/Gauss at a temperature of 15 K and allows for detection of micromolar spin concentrations of organic radicals in



volumes of less than a microliter. Echo-detected absorption spectra were acquired with a three-pulse stimulated echo sequence ( $\pi/2 - \pi/2 - \pi/2$ ) by integrating the spin echo in dependence of the magnetic field. The field and  $g$ -values were calibrated measuring a  $\text{Mn}^{2+}/\text{MgO}$  standard directly after the BCR samples and observing the spectrometer frequency with a spectrum analyzer (8563A, Hewlett-Packard). Experimental conditions such as shot repetition time, pulse separation time and shots per point were adjusted as indicated in the figure caption and described in the text.

**G-band samples and loading frozen samples** The enzyme sample solution with a concentration of  $950 \mu\text{M}$  was anaerobically transferred into thin capillary quartz tubes (0.4 mm o.d., Wilmad) suited for the 180 GHz  $\text{TE}_{011}$  cavity. The time for freeze-quenching the small capillaries was about 1.5 min. In order to measure frozen samples on the home-built 180 GHz EPR spectrometer the EPR probe head was equipped with specially designed plungers made out of G10 [29]. The latter is a material with low temperature coefficient which guarantees that the plunger's slot diameter remains constant so that capillaries can be inserted without breaking. The frozen samples were inserted through the plunger into the cavity which was covered by liquid nitrogen. Subsequently the precooled EPR probe containing the frozen sample was inserted into the helium cryostat at 100 K.

**Simulation of EPR spectra** CW X- and Q-band EPR spectra were simulated using the commercial software Simfonia from Bruker. In the simulations, the hyperfine and  $g$ -tensors were assumed to be collinear, with  $A_{x,y}$  being parallel to  $g_{x,y}$  and  $A_z$  parallel to  $g_z$ , and a gaussian line shape with a line width of 10 G was used.

### 3.3 Multifrequency EPR Studies of BCR

As a first attempt for resolving the  $g$ -values of the 4-F-BCoA-induced  $g = 2.015$  species and to identify and further characterize the nature of the radical intermediates postulated from previous EPR studies [5, 14], pulsed EPR spectroscopy was performed at high frequency, namely at 180 GHz. Additionally, CW X- and pulsed Q-band EPR spectra of the inhibited enzyme were acquired in order to

discriminate between  $g$ -anisotropy and hyperfine couplings. In order to disentangle the overlapping signals originating from more than one species present in the samples with respect to their relaxation behaviour, temperature-dependent measurements were performed. However, the spectral components could not be separated since their relaxation times were observed to be very similar. Furthermore, the effect of  $^{33}\text{S}$ -labeling of the enzyme on the EPR line shape at X- and Q-band was used to test the hypothesis of a disulfide radical anion being involved in the reduction process of benzoyl-CoA. Therefore, the temperature-dependent EPR spectra at X- and Q-band of the labeled enzyme were compared with the ones from the unlabeled enzyme with special focus on the signal observed at 20 K.

### 3.3.1 Pulsed high-field measurements at 180 GHz

Preliminary measurements of the freeze-quenched samples (see Section 3.2) performed within a temperature range of 5 up to 30 K revealed that the spectral features exceeded the sweep range of the sweep coils ( $\pm 730$  G). Broader field ranges can be covered sweeping the main field of the superconducting magnet. Figure 3.2 shows the 180 GHz three-pulse echo-detected spectrum of unlabeled BCR obtained sweeping the main coil over a range of 3000 G at a temperature of 5 K. The spectrum extends from  $g = 2.035$  to  $g = 1.96$  with no sharp features but rather a broad absorption with singularities at  $g = 2.034(1)$ ,  $g = 2.027(1)$ ,  $g = 2.010(1)$  and  $g = 2.004(1)$ .

In order to separate EPR signals originating from different paramagnetic species according to their relaxation behaviour, different approaches were used in the present study. First, spectra were recorded varying the shot repetition time (SRT) from 100  $\mu\text{s}$  up to 500 ms (data not shown) in order to separate signals with different longitudinal relaxation times  $T_1$ . However, this proved little efficient possibly because the different species possess very similar relaxation times  $T_1$  ( $\approx 10$  ms at 5 K) and hence separation of the corresponding EPR signals becomes difficult. The spectra measured with the shortest SRT of 100  $\mu\text{s}$  did not resolve any signals, and apart from the vanished singularity at  $g = 2.004$  (with  $T_1 \approx 100$  ms at 5 K) only a broad underground with no significant features remained. Measuring with longer SRTs, only the singularity at  $g = 2.004$  became more pronounced, but no further signals could be separated. In a second attempt, the temperature was raised over 10 and 15 K up to 30 K. However, the signal-to-noise ratio drastically decreased at temperatures above 10 K due to the

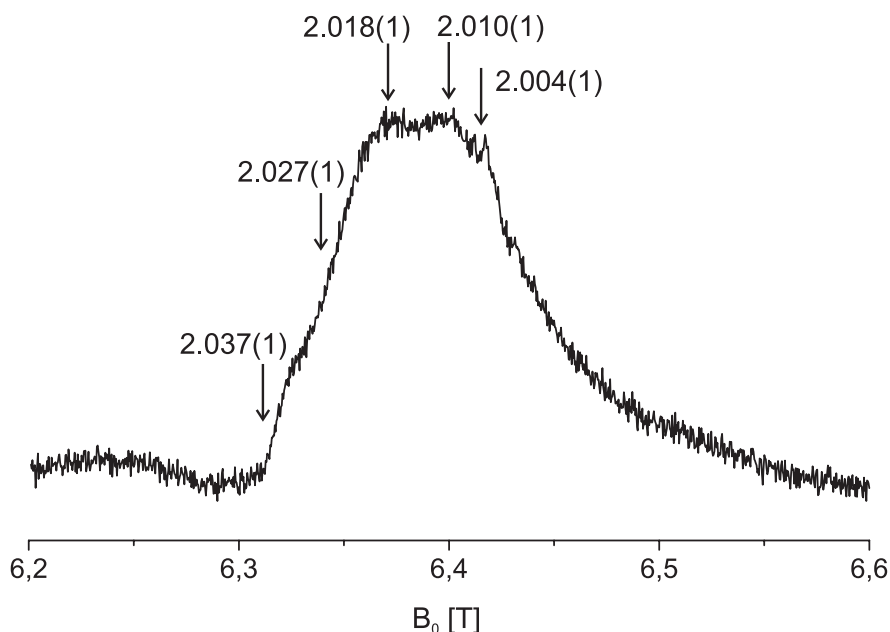


**Figure 3.2** 180 GHz field-swept (via main coil) echo-detected spectra of unlabeled BCR reduced with 0.5 equivalents of dithionite acquired at 5 K. Experimental parameters: MW pulse length  $t_{\pi/2} = 70$  ns, pulse separation time  $\tau = 200$  ns, shot repetition time = 10 ms, shots per point = 25. For further details see Section 3.2. The arrows indicate the observed spectral components also observed in the X- and Q-band studies (see text).

low spin concentration (less than  $100 \mu\text{M}$ ) and the fast relaxation of the paramagnetic species. In another experiment the pulse separation time of a two-pulse Hahn-echo sequence was changed (see Chapter 2) in order to separate the signals with respect to their transverse relaxation times  $T_2$ . However, the decrease of signal-to-noise ratio rendered the experiments little successful.

### 3.3.2 CW X- and pulsed Q-band EPR studies of unlabeled and $^{33}\text{S}$ -labeled BCR

In the following, the temperature-dependent spectral features observed in CW X- and pulsed Q-band EPR spectra of the unlabeled and  $^{33}\text{S}$ -labeled enzyme are described and differences between spectral features observed in the unlabeled and labeled spectra are discussed, along with differences observed in the X- and Q-band spectra. Afterwards, we discuss whether the observed  $g$ -values and broadening in the  $^{33}\text{S}$ -labeled spectra are in agreement with a disulfide radical anion using simulations employing the  $g$ - and hyperfine tensor components reported for

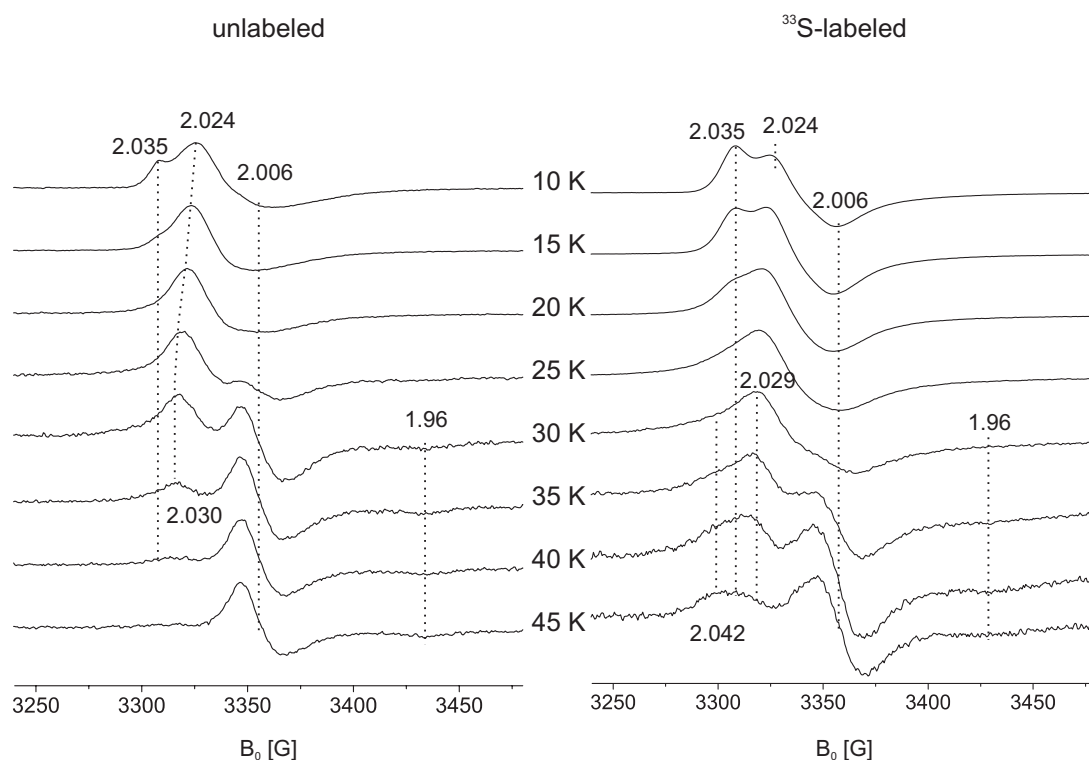


**Figure 3.3** Temperature dependent CW X-band EPR spectra (normalized to the maximum EPR signal in each spectrum) of unlabeled (left) BCR reduced with 0.5 equivalents of dithionite in comparison with spectra from the  $^{33}\text{S}$ -labeled enzyme (right). For experimental parameters see Section 3.2.

disulfide radical anions in the literature.

### Observations at X-band

The spectra acquired in a temperature range from 10 to 45 K obtained from unlabeled and  $^{33}\text{S}$ -labeled enzyme reduced with 0.5 equivalents of dithionite are shown in Figure 3.3.

Overall, as was observed in the pulsed high-field EPR spectra, the spectra reveal more than one radical species present in the sample. In particular at low temperatures, i.e. from 10 to 30 K, the spectra are composed of more than one species. In contrast to pulsed EPR, overlapping signals observed in CW EPR spectra can not be separated according to their longitudinal and transversal relaxation times since the saturation behaviour in CW EPR depends on the product of both. However, if this product differs sufficiently from one species to

the other, one may successfully deconvolute the observed signals with varying the temperature or the microwave power. In the present study, disentanglement of the EPR signals varying the microwave power at constant temperature was not possible (data not shown), and only at high temperatures one signal could be extracted by increasing the temperature to 45 K.

In the low temperature range, the spectra of the unlabeled enzyme are dominated by two singularities at  $g = 2.035$  ("signal I") and  $g = 2.024$ . At 20 K, the latter possesses a maximum around  $g = 2.027$  and will be called "signal II" in the following. At temperatures  $\geq 45$  K, the spectra display two singularities at  $g = 2.006$  and  $g = 1.96$  ("signal III"). In an intermediate temperature regime around 30 K, an intense peak appears at  $g = 2.030$  ("signal IV"), along with the high temperature singularities. From the temperature-dependent spectra, the observed signals can be distinguished via their different relaxation behaviour on a qualitative level. They can be ordered from fast to slow relaxation according to  $g = 2.035 \leq g = 2.024 \leq g = 2.030 \leq g = 2.006, g = 1.96$ .

The observations in the spectra obtained from  $^{33}\text{S}$ -labeled BCR differ in the following points from the ones in the spectra of the unlabeled enzyme: First, at 30 K, the maximum of the broad singularity observed at  $g = 2.030$  in the unlabeled samples is shifted towards  $g = 2.029$ , and only at 35 K, the maximum is observed at  $g = 2.030$  (signal IV). Second, the relative signal intensities differ in the spectra of the labeled enzyme in comparison to the ones observed in the unlabeled enzyme. At 10 K, the  $g = 2.035$  signal (signal I) is more intense than the  $g = 2.024$  signal (signal II), whereas at 30 K, the signal with maximum around  $g = 2.029$  is more pronounced in comparison to the high temperature features centered around  $g = 2.006$  (signal III). Furthermore, at 45 K, an additional signal is visible around  $g = 2.043$  ("signal SV") along with a sharp signal around  $g = 2.030$  which increases when raising the power (data not shown) and therefore originates from a fast relaxing species. Finally, the singularity around  $g = 1.96$  appears to be less resolved or broadened in the spectra from the labeled enzyme.

The EPR signal observed by Boll and coworkers which was proposed to be due to a disulfide radical anion was centered around  $g = 2.015$  with a line width of 25–30 G and developed maximum intensity around 20 K [14]. In order to deconvolute the signal with maximum intensity at 20 K in the present study (signal II), the spectrum recorded at 45 K was subtracted from the 20 K spectrum as depicted in Figure 3.4. The line shape of the extracted signal is similar to the one observed by our collaborators, with a peak-to-peak width of 25 G, whereas the signal is

shifted from  $g = 2.015$  to a slightly higher  $g$ -value of 2.018. This difference might be due to an error from taking difference spectra of weak samples in the single turnover experiment. The narrow line width and the  $g$ -value of the deconvoluted signal at 20 K suggests that it derives from a radical species.

In order to find out whether this signal is due to a sulfur-centered radical, we superimposed the deconvoluted 20 K signal of the  $^{33}\text{S}$ -labeled enzyme as shown in Figure 3.4. The superposition shows that both signals have a maximum at 2.027 and a zero crossing at  $g = 2.018$ . However, the  $g_z$  component appears at 2.011 in the unlabeled samples in comparison to 2.009 found in the labeled samples. Furthermore the deconvoluted line shape of the signal from the  $^{33}\text{S}$ -labeled enzyme appears to be broadened and a shoulder becomes visible around  $g = 2.035$  in comparison to the signal from unlabeled BCR. In order to better resolve the observed spectral features and clarify whether this broadening indeed originates from two hyperfine couplings of nuclear spin  $I = \frac{3}{2}$ , or rather from the superposition of an additional species due to different sample conditions or preparations, but not connected with the  $^{33}\text{S}$ -labeling, we performed measurements at a higher frequency, namely at Q-band, as described in the following.

### Observations at Q-band

The CW and pulsed Q-band spectra shown in Figure 3.5 were obtained from unlabeled and labeled Q-band samples prepared from the same enzyme solution as used for the X-band samples.

For the unlabeled samples, the overall spectral features observed in the CW X-band EPR spectra were also found in the Q-band spectra, however at different temperatures as described in the following. The latter is not surprising since the relaxation behaviour of radicals is known to depend on the frequency range [30]. At low temperatures a sharp singularity at  $g = 2.037$  (signal I) along with a broad signal with maximum around  $g = 2.025$  (signal II) and a long tail at high fields are observed. At increasing temperatures, signal I vanishes while the maximum of signal II is shifted towards  $g = 2.029$  at 15 K and two singularities at 2.008 and 2.003 appear. At 20 K, two broad signals with maxima around 2.030 (signal IV) and 2.012 (signal III) are observed for which  $T_1$ -measurements showed that signal IV is due to a very fast relaxing species ( $T_1 \approx 3 \mu\text{s}$ ) whereas signal III originates from a species relaxing about 100 times slower ( $T_1 \approx 300 \mu\text{s}$ ). In comparison with the CW X-band spectra, the low temperature signal (signal I)

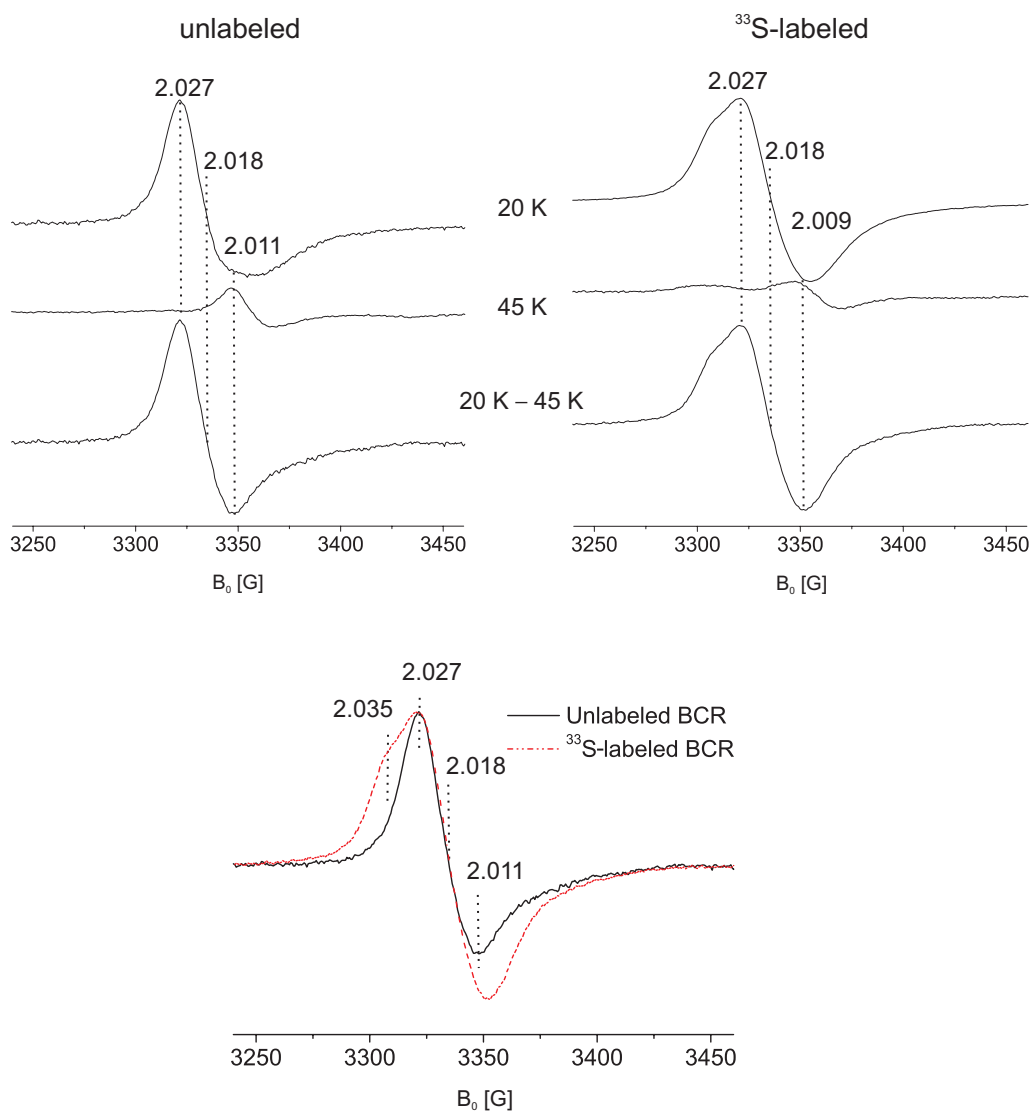


**Figure 3.4** Top: Deconvolution of the 20 K X-band EPR spectrum from unlabeled and <sup>33</sup>S-labeled BCR obtained by subtraction of the high temperature spectrum. The spectra were normalized to the noise dividing by the number of scans performed. Bottom: Superposition of the deconvoluted 20 K signals. For experimental parameters see Section 3.2.

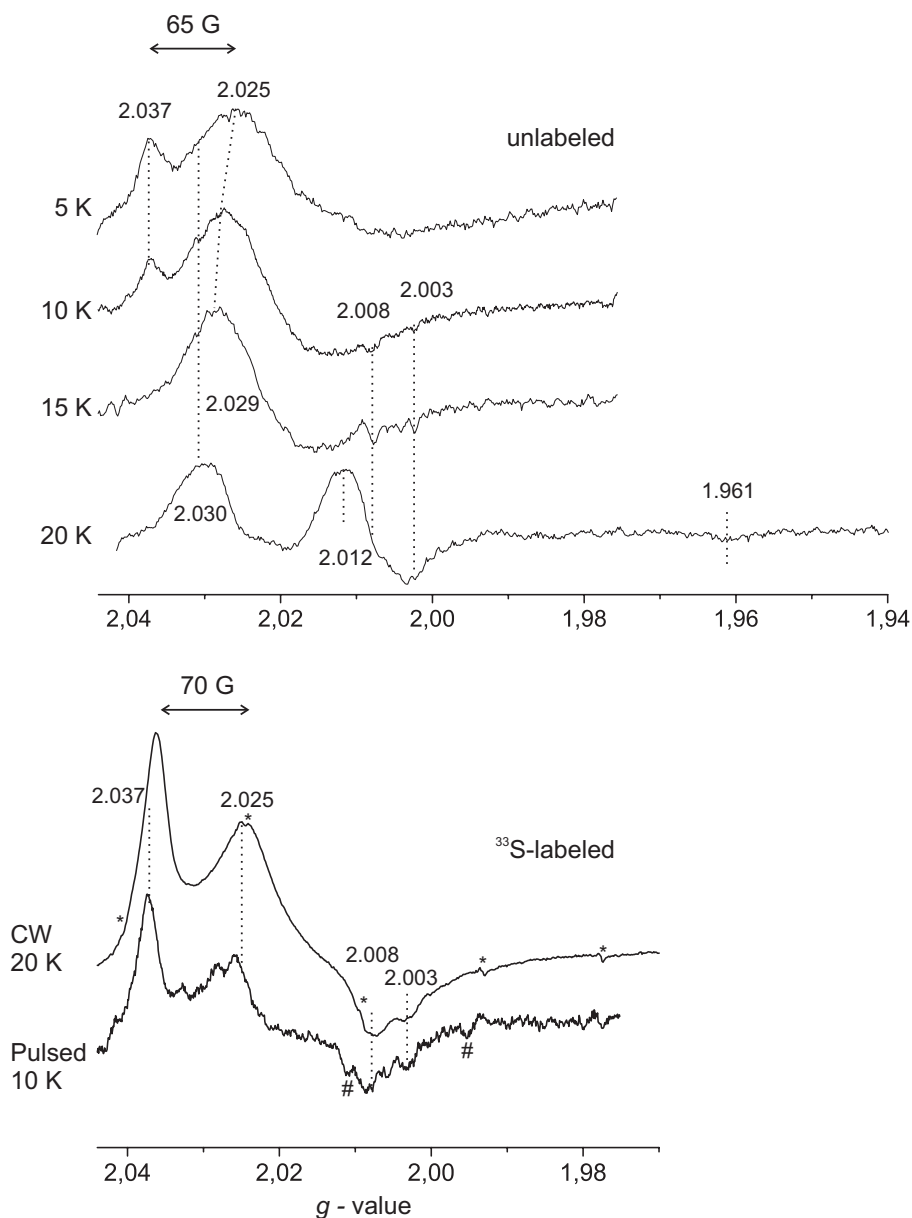


**Figure 3.5** Temperature-dependent Q-band EPR spectra from unlabeled (top) and  $^{33}\text{S}$ -labeled (bottom) 4-F-CoA-inhibited BCR reduced with 0.5 equivalents of dithionite. The former were acquired in pulsed mode whereas the spectra from the labeled enzyme were obtained in the pulsed and CW mode as indicated. The \* indicate a  $\text{Mn}^{2+}$  signal from the cavity background and the # marks the high temperature signals (see text). Experimental parameters: CW Q-band spectra: 71 scans with experimental parameters described in Section 3.2. Pulsed Q-band: unlabeled BCR: SRT = 1 ms (5 and 10 K) and 0.5 ms (15 and 20 K), 4, 1, 8 and 1 scans with 200, 400, 200 and 400 shots per point at 5, 10, 15 and 20 K, respectively;  $^{33}\text{S}$ -labeled BCR: 1 ms at 10 K, 1 scan with 400 shots per point. For further experimental details see Section 3.2.



observed at X-band at  $g = 2.035$  shows an effective  $g$ -value of  $g = 2.037$  in the Q-band spectra.

In contrast, the pulsed Q-band spectra from the labeled enzyme showed an overall signal intensity which was much weaker than for the unlabeled samples such that already at 15 K, hardly any spectral features could be resolved. The CW Q-band measurements at 20 K yielded a good signal-to-noise ratio for the labeled samples, whereas attempts to obtain a CW EPR spectrum for the unlabeled samples failed due to power saturation. Because of the very poor signal-to-noise ratio and the low information content, only the spectrum with the best signal-to-noise ratio acquired at 10 K is shown in Figure 3.5 along with the CW Q-band spectrum of the same sample measured at 20 K. In the CW Q-band spectrum measured at 20 K, signal I has an effective  $g$ -value of  $g = 2.036$  and signal II has a broad maximum at  $g = 2.025$ , showing up along with two singularities at  $g = 2.008$  and  $g = 2.003$ . Although these features are also found in the pulsed spectrum (however with  $g = 2.037$  in contrast to  $g = 2.036$ ), they are much weaker.

It is difficult to judge which temperature range in the pulsed mode corresponds to 20 K when measuring in CW mode with respect to the spectral contributions from different radical species. Therefore, the spectral features observed in the 20 K CW Q-band spectrum from the labeled enzyme are compared with the pulsed spectra of the unlabeled enzyme acquired at two different temperatures (at 10 and 5 K), as shown in Figure 3.6. Overall, the spectra from the labeled and the unlabeled enzyme display very similar features and no clear broadening is observed in the spectra from the labeled enzyme. As main difference, the broad maximum of signal I observed at  $g = 2.025$  in the labeled spectra is observed at  $g = 2.027$  in the spectra of the unlabeled sample recorded at 10 K. Furthermore, in the spectra from the labeled enzyme, the signal I species ( $g = 2.036/2.037$ ) appears to be more pronounced in comparison to the signal II species as was already found at X-band.

### 3.3.3 Do the observations indicate the presence of a disulfide radical anion?

Regarding the question whether the signal with maximum signal intensity at 20 K is due to a disulfide radical anion, the differences observed in the X- and Q-band EPR spectra of the labeled and the unlabeled enzyme raise the ques-

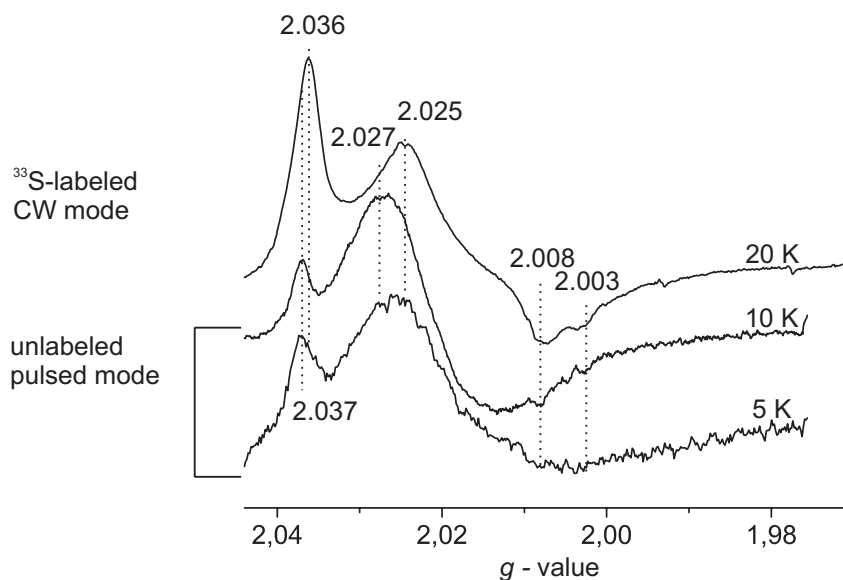


**Figure 3.6** Comparison of CW Q-band EPR spectrum of  $^{33}\text{S}$ -labeled BCR with pulsed Q-band spectrum of unlabeled BCR reduced with 0.5 equivalents of dithionite, measured at 20 K, 10 K and 5 K, respectively. Experimental parameters: see Figure 3.5.

tion whether the broadening in the 20 K X-band spectrum from labeled enzyme originates from two sulfur hyperfine couplings of the disulfide group or from different contributions of trapped radicals in the labeled sample in comparison to the unlabeled samples. From the above described observed signals in the X- and Q-band spectra it appears possible that the unlabeled X- and Q-band samples contain an increased contribution from the signal II species ( $g = 2.024$ ) but less from the signal I and signal IV species ( $g = 2.035$  and  $g = 2.030$ , respectively) and no contributions from the signal SV species ( $g = 2.043$ ) in comparison to the labeled samples. Therefore, possible signals which could cause the broadening observed in the labeled spectra are the signals I, IV and SV found in the spectra of the labeled enzyme as will be discussed in this section. Simulations of the labeled and unlabeled spectra using  $g$ -values and hyperfine couplings for a disulfide radical anion reported in the literature help to shed some light on this question as described in the following.

## Simulations

In order to answer the question whether the observed broadening in the deconvoluted X-band 20 K spectrum could be due to two sulfur hyperfine couplings and whether this is in line with the spectral features observed at Q-band, the spectra at X- and Q-band (the deconvoluted spectrum at 20 K and the spectrum at 10 K, respectively) were simulated following  $g$ -values and hyperfine couplings for a disulfide radical anion reported in the literature. First, the  $g$ -values were obtained from the simulation of the spectra from the unlabeled enzyme at both frequencies, and afterwards the effect of two sulfur nuclei on the line shape was estimated including two  $I = \frac{3}{2}$  hyperfine coupling tensors in the simulation.

The simulation of the X- and Q-band spectra of the unlabeled sample was obtained including hyperfine tensor components from two protons in the range of the ones reported in the literature for disulfide radical anions (see Table 3.1). Two simulations with slightly different  $g$ - and HFC tensor components are shown in Figure 3.7. For the simulation, the  $g$ - and HFC tensors were assumed to be collinear (see Section 3.2). Simulation *A* was obtained with  $g_x = 2.026$ ,  $g_y = 2.017$  and  $g_z = 2.002$  along with two proton hyperfine couplings of  $A_x = 8$  G,  $A_y = 9$  G,  $A_z = 13$  G while for simulation *B*  $g$ -tensor components  $g_x = 2.0245$ ,  $g_y = 2.0190$  and  $g_z = 2.0020$  were used along with two hyperfine couplings of  $A_x = 8$  G,  $A_y = 10$  G,  $A_z = 12$  G. Both simulations using  $g$ -values and two proton hyperfine couplings in the range of the literature values match the experimental X-band EPR spectrum at the low-field side, however not at the high-field side. This mismatch at the  $g = 2.002$  position is even more pronounced in the simulations of the Q-band experimental spectrum. The additional discrepancy of the  $g_y$ -component in simulation *B* with the Q-band experimental spectrum excludes the  $g$ -values used therein. In contrast, simulation *A* is considered as solution since it can not be excluded taking into account the presence of more than species in the samples whose signals overlap in the observed X- and Q-band EPR spectra.

In the following, the  $g$ -values and proton hyperfine couplings obtained from simulation *A* were used for simulating the effect of two nuclear spins  $I = \frac{3}{2}$  on the EPR line shape. The simulations were performed by including two  $I = \frac{3}{2}$  hyperfine couplings following quantum chemical calculations for disulfide radical anions [33]. These predict a strongly anisotropic hyperfine tensor with  $A_{\parallel} \approx 50$  G

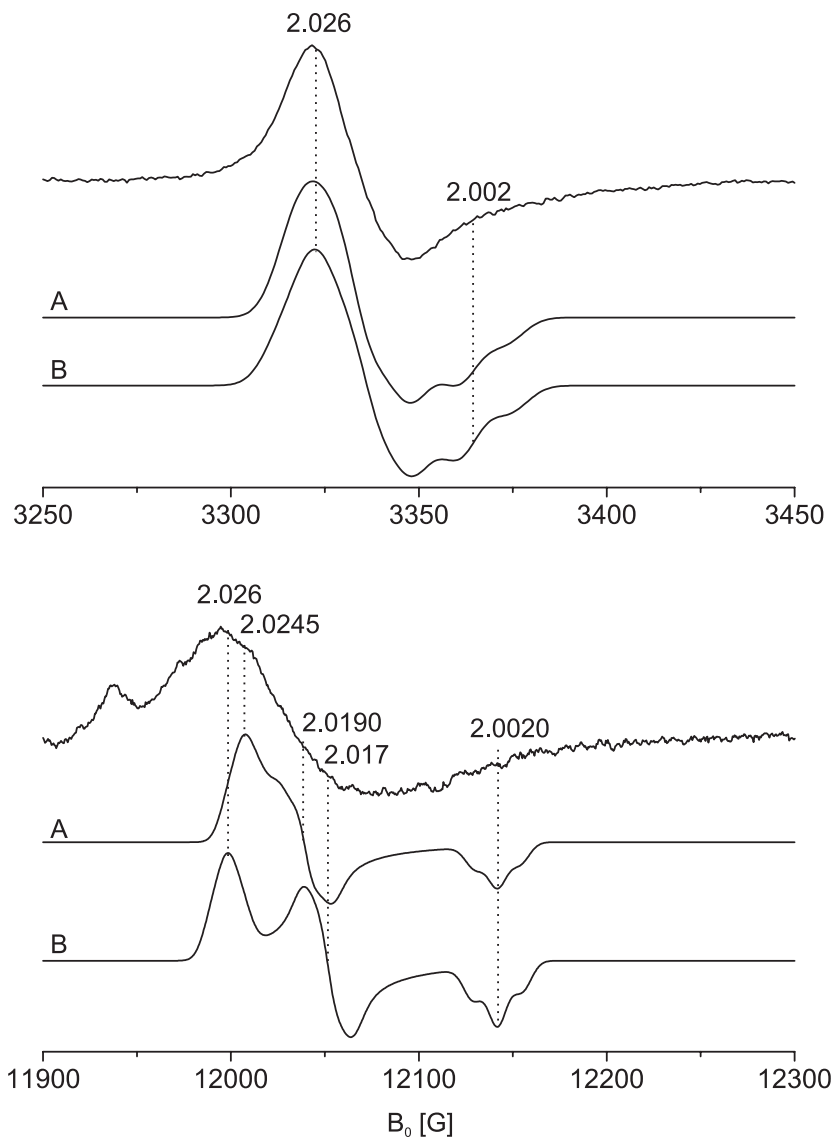


**Figure 3.7** Simulation of the deconvoluted 20 K CW X-band EPR spectrum (top) and the pulsed Q-band EPR spectrum at 10 K (bottom) of unlabeled BCR at 20 K (X-band) and 10 K (Q-band) with slightly different  $g$ - and HFC-tensor components: (A)  $g_x = 2.026$ ,  $g_y = 2.017$  and  $g_z = 2.002$  along with two  $I = \frac{1}{2}$  hyperfine couplings of  $A_x = 8$  G,  $A_y = 9$  G,  $A_z = 13$  G; (B)  $g_x = 2.0245$ ,  $g_y = 2.0190$  and  $g_z = 2.0020$  along with two  $I = \frac{1}{2}$  hyperfine couplings of  $A_x = 8$  G,  $A_y = 10$  G,  $A_z = 12$  G.

**Table 3.1** Principal  $g$ -values and proton as well as  $^{33}\text{S}$  hyperfine couplings (in G) for disulfide radical anions reported in the literature.

$g_x$	$g_y$	$g_z$	nucleus	$a_{\text{iso}}$	$A_x$	$A_y$	$A_z$	Ref.
2.017	2.014	2.002	H <sub>1</sub> , H <sub>2</sub>	8–11	–	–	–	[31]
–2.024	–2.020							
2.018	2.018	2.002	H <sub>1</sub> , H <sub>2</sub>	8–10/6–8	–	–	–	[32]
			$^{33}\text{S}$	–	5.8	5.8	22.7	[32]
2.023	2.015	2.002	H <sub>1</sub> , H <sub>2</sub>	10	–	–	–	[22]
2.028	2.009	2.002	H <sub>1</sub> , H <sub>2</sub>	2/2/8	1/1/7	2/2/8	3/2/10	[33]
			$^{33}\text{S}$	0	0	52		[33]
2.023	2.021	2.002	H <sub>1</sub> , H <sub>2</sub>	2/3/11	1/2/10	2/2/10	3/4/12	[33]
			$^{33}\text{S}$		3	3	55	[33]

and  $A_{\perp} \approx 0$  G, which we used for simulation  $D$  depicted in Figure 3.8. Whereas at X-band this coupling clearly exceeds the observed broadening, at Q-band, a hyperfine splitting of this size could be hidden by the overlapping broad spectral features.

At this point, it should be noted that the calculations were performed for a isolated radical. However, in a protein environment the size of the hydrogen and sulfur HFCs were found to depend on the dihedral angle of the hyperconjugated hydrogens [33, 34]. Therefore, the spectra were simulated using slightly smaller hyperfine couplings in order to find a parameter set which better fits the X-band experimental spectrum. Simulation  $C$  in Figure 3.8 depicts the simulated spectrum using two  $I = \frac{3}{2}$  hyperfine tensors with slightly differing and smaller  $A_z$  components than predicted from the DFT calculations, close to the ones reported by Hadley et al. [32] observed in irradiated single crystals of cystine dihydrochloride. The two  $I = \frac{3}{2}$  tensors have the main components  $A_{x1} = A_{y1} = 0$  G,  $A_{z1} = 24$  G and  $A_{x2} = A_{y2} = 0$  G,  $A_{z2} = 27$  G. Although this simulation fits the X-band experimental spectrum better than simulation  $D$ , a (small) shift of the maximum at  $g = 2.027$  caused by the HFC couplings from two  $I = \frac{3}{2}$  nuclei to lower fields is observed. In the Q-band spectra, the most remarkable effect of two  $I = \frac{3}{2}$  hyperfine couplings of this size is a broadening of the  $g_z$  component.

The simulation which best fits the experimental data is therefore simulation  $C$  with  $g_x = 2.0245$ ,  $g_y = 2.0190$  and  $g_z = 2.0020$ , including two  $I = \frac{1}{2}$  HFCs with  $A_x = 8$  G,  $A_y = 10$  G,  $A_z = 12$  G and two additional  $I = \frac{3}{2}$  HFCs with  $A_{x1} = A_{y1} = 0$  G,  $A_{z1} = 24$  G and  $A_{x2} = A_{y2} = 0$  G,  $A_{z2} = 27$  G. In comparison to the experimental  $g$ -values found for the disulfide radical anion in

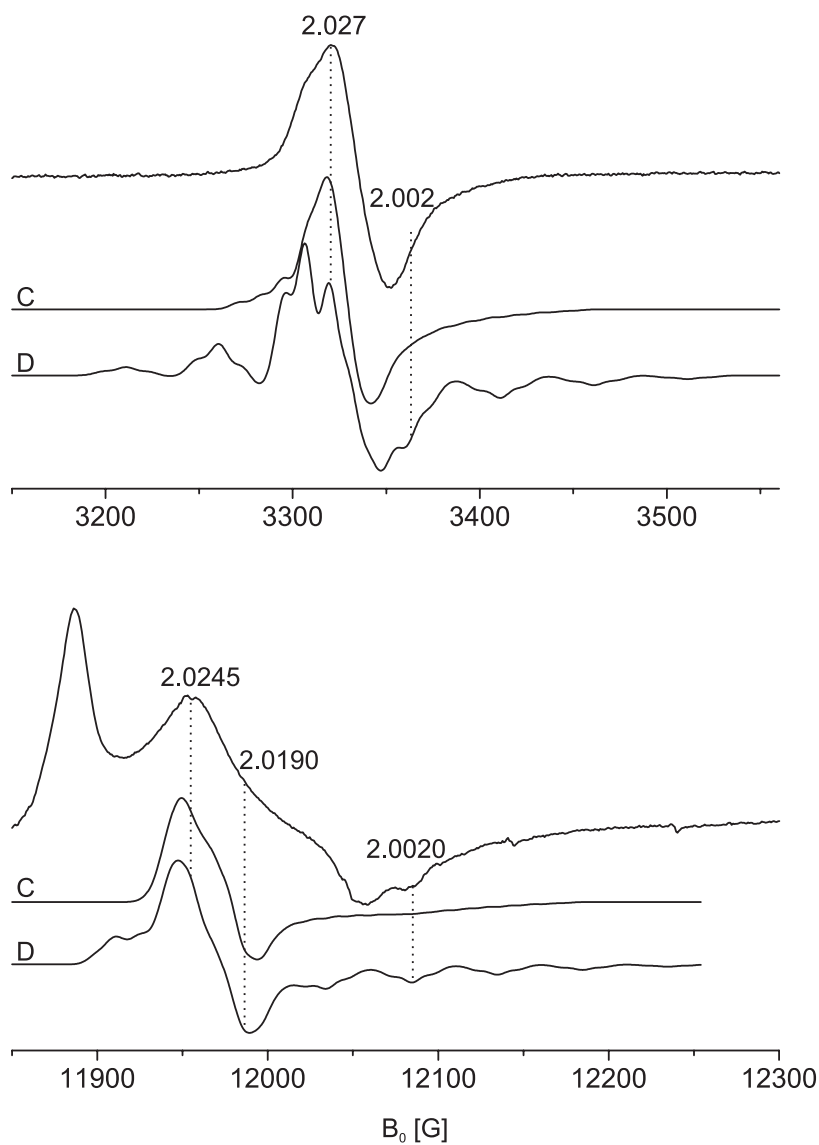


**Figure 3.8** Simulation of deconvoluted 20 K CW X-band EPR spectrum (top) and pulsed 10 K Q-band EPR spectrum (bottom) of  $^{33}\text{S}$ -labeled BCR with the  $g$ - and hyperfine tensor components obtained from unlabeled BCR at X- and Q-band (see Figure 3.7) with  $g_x = 2.0245$ ,  $g_y = 2.0190$  and  $g_z = 2.0020$  including two proton HFC tensors with  $A_x = 8$  G,  $A_y = 10$  G,  $A_z = 12$  G and two additional  $I = \frac{3}{2}$  HFC tensors: (C)  $A_{x1} = A_{y1} = 0$  G,  $A_{z1} = 24$  G and  $A_{x2} = A_{y2} = 0$  G,  $A_{z2} = 27$  G; (D)  $A_x = A_y = 0$  G,  $A_z = 50$  G following DFT calculations [33].

RNR [22], the simulated  $g_x$ - and  $g_y$ -values are slightly larger. In comparison to the calculated values, the simulated  $g$ -tensor  $x$ - and  $y$ -components lie in between the two calculated tensor sets with slightly varied geometry [33]. Although the size of the HFCs used for simulation  $C$  simulate the broadening observed in the X-band spectrum reasonably well and are close to the  $^{33}\text{S}$  couplings reported by Hadley et al. [32], the simulations show that the hyperfine interaction of two  $I = \frac{3}{2}$  spins with the radical should shift the maximum of the 20 K signal to lower fields, an effect which was not observed when comparing the X-band 20 K spectra from the labeled and the unlabeled enzyme. Overall, the simulation studies do neither strongly support nor exclude the existence of a disulfide radical anion.

### Different radical contributions in the labeled and unlabeled samples

An alternative reason for the observed broadening in the X-band 20 K spectrum of the labeled enzyme may be the presence of an additional broad signal due to contributions of different species in the  $^{33}\text{S}$ -labeled samples. As found by the temperature-dependent X-band spectra, the X-band samples of the labeled enzyme contained more intensity from signal I ( $g = 2.035$ ) with respect to signal II ( $g = 2.024$ ), as well as more intensity of signal IV ( $g = 2.030$ ) with respect to signal III ( $g_{\text{av}} = 2.006$ ), similar as found for measurements of the unlabeled enzyme reduced with one equivalent of dithionite (see Figure C.2 in Appendix C). Furthermore, at 45 K, signal SV ( $g = 2.043$ ) observed in the labeled spectra was not observed at all in the spectra from the unlabeled enzyme. Therefore, in principle these three signals could cause the additional broadening in the 20 K spectrum of the labeled enzyme. In order to get an idea if the additional signal SV could in principal be responsible for such a broadening, we added the  $g = 2.043$  contribution of the 45 K spectrum from the labeled enzyme to the unlabeled spectrum at 20 K as depicted in Figure 3.9. From the comparison with the 20 K spectrum of the labeled enzyme it appears possible that such an additional signal could indeed cause the observed broadening.

The observation that the  $g = 2.043$  singularity was not found in the Q-band spectra raises the question about the reproducibility of the sample preparation with respect to the reduction and the freeze-quench preparation, as well as differences between the X- and Q-band samples. In order to find out whether the X-band samples contain the same (contributions of) species as the Q-band samples, and therefore to estimate up to which extent the observations at X- and at

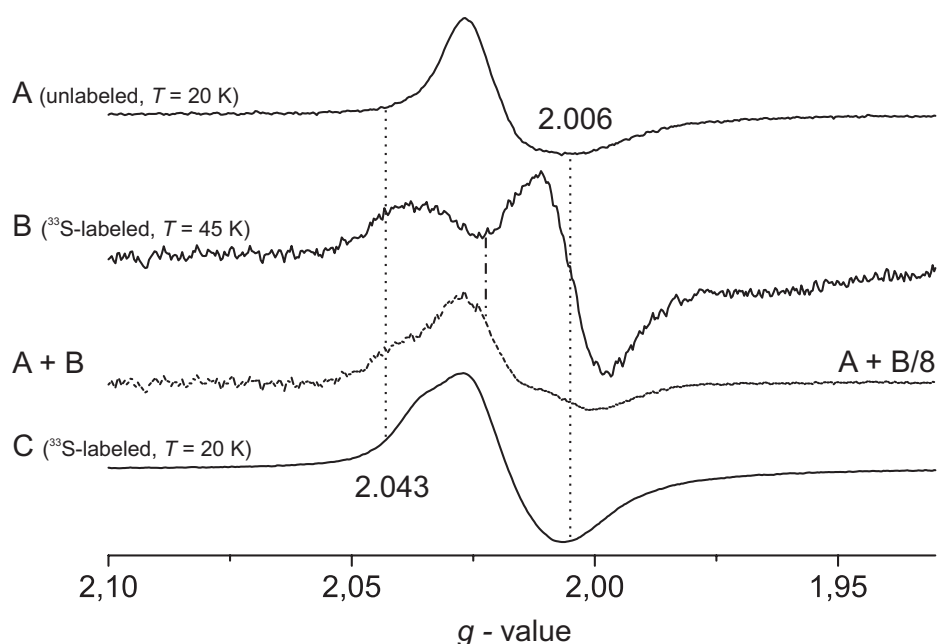


**Figure 3.9** Sum of the 20 K CW X-band EPR spectrum of the unlabeled enzyme (A) and the 45 K CW X-band EPR spectrum from <sup>33</sup>S-labeled BCR (B) and comparison with the 20 K spectrum from <sup>33</sup>S-labeled BCR (C). In order to make up for the large contribution of the signal at  $g_{av} = 2.006$  at 45 K, the spectrum was split into two halves, dividing the intensity of the latter by a factor of eight in comparison to the  $g = 2.043$  signal starting from the position on the  $g$ -axis indicated by the dotted line. For experimental parameters see Section 3.2.

Q-band can be compared with each other, the Q-band samples were measured at X-band at 20 K as shown in Figure C.1. These spectra reveal that both Q-band samples contain more contribution of the high-field signal in comparison to the X-band samples. This comparison shows that although the samples were quenched in liquid nitrogen at the same time, differences in samples may arise either from the reduction procedure or the time of freeze-quenching. This may be explained by the smaller capillary diameter of the Q-band samples which allows for faster freezing of the enzyme solution. Similarly, we found that the contributions of the different spectral features slightly varied when measuring samples from different enzyme preparations as well as when repeating the measurements of the same samples at different dates. Hence, although the samples were prepared with an inhibitor, the observed spectral components (and therefore the trapped radical intermediates) appear to differ slightly from sample to sample.



### Other signals broadened in sulfur-labeled spectra?

According to the single turnover studies performed by Boll et al. [14], at least three [4Fe-4S] clusters should be present in the sample. Although Mössbauer studies had shown that all [4Fe-4S] clusters are diamagnetic (although not specifically for the EPR samples), the relaxation behaviour and the  $g$ -value of the high temperature signal would be in line with an [4Fe-4S] cluster, such that the presence of paramagnetic [4Fe-4S] clusters in the samples can not be excluded. Furthermore, although the inhibition with 4-F-CoA is expected to efficiently prevent the electron transfer to the aromatic ring of benzoyl-CoA, one could imagine that in a small proportion of enzymes the electron is transferred to the benzene ring yielding an inhibitor signal. Therefore, in order gain more information about the nature of the trapped intermediates, we searched for broadenings on the overall observed spectral features. The superpositions of spectra from  $^{33}\text{S}$ - and unlabeled 4-F-BCoA-inhibited BCR at 10, 30 and 45 K are depicted in Figure 3.10.

As discussed above, at 20 K, no shift on the maximum is observed in the spectra from the labeled enzyme in comparison to the unlabeled enzyme which in contrast would be expected if two sulfur atoms were present in the samples. At 10 K, the increased contribution of the  $g = 2.035$  signal is not visibly broadened in the spectra from the labeled enzyme, in line with observations at Q-band. Although the  $g = 2.030$  signal observed at 30 K appears broadened, it is not clear if this is due to an additional contribution of a broad species (such as the  $g = 2.029$  signal) or due to an  $^{33}\text{S}$  coupling. In contrast, a broadening is observed on the high temperature  $g = 1.96$  singularity, although no clear splitting can be observed.

## 3.4 Summary and Discussion

Using RFQ techniques in combination with multifrequency EPR spectroscopy, the present study aimed at identifying a putative radical intermediate in benzoyl-CoA reductase which catalyzes the reduction of benzoyl-CoA. Since catalysis occurs on the sub millisecond time scale, the detection of such short-lived radical intermediates is very demanding. With the use of an inhibitor some of the mechanistic steps can be chemically or kinetically hindered, such that protein- or substrate-based radicals are accumulated on a longer (usually second) time scale and with freeze-quench techniques trapped for investigation by EPR spectroscopy [21]. On

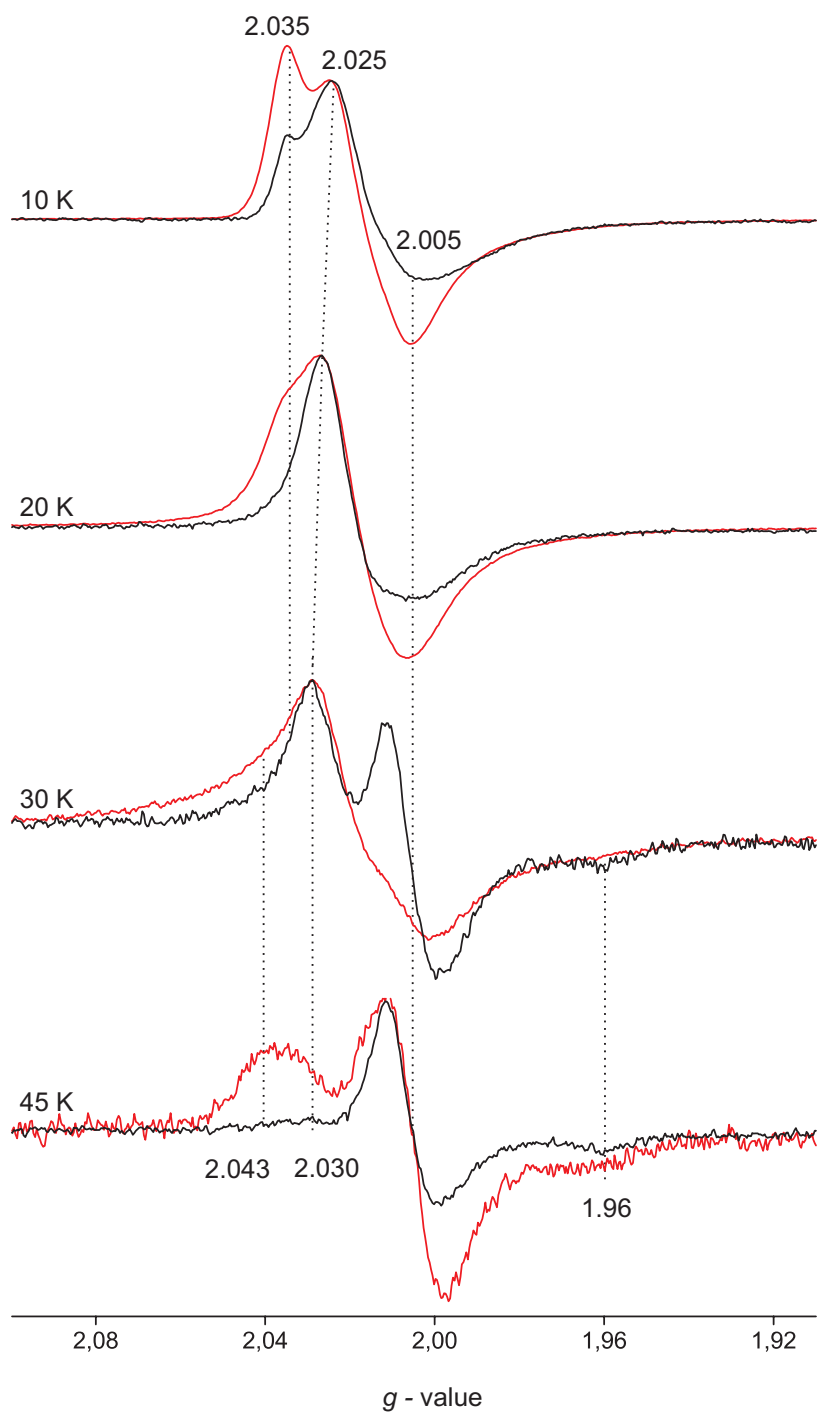


**Figure 3.10** Comparison of temperature-dependent CW EPR X-band spectra of unlabeled Benzoyl-CoA reductase (black) with spectra from the  $^{33}\text{S}$ -labeled enzyme (red) reduced with 0.5 equivalents of dithionite. For experimental parameters see Section 3.2.

the basis of this technique, Boll and coworkers studied the stopped-flow UV-Vis and EPR signals obtained from 4-F-BCoA-inhibited BCR [6]. The authors proposed a mechanistic model in which a fast relaxing  $g = 2.015$  signal from a radical intermediate observed at 20 K was suggested to be due to a disulfide radical anion, whose fast relaxation behaviour was attributed to its interaction with an iron-sulfur cluster near by [6]. In the present study, the use of pulsed high-field and pulsed Q-band EPR spectroscopy aimed at resolving the  $g$ -values of the trapped paramagnetic species. Furthermore, the effect of  $^{33}\text{S}$ -labeling on the line shape of the inhibited signals was studied using CW X- and Q-band in order to find more evidence for the presence of a sulfur-centered radical species.

One difficulty in identifying radical intermediates in enzymatic reactions originates from the fact that the samples often consist of mixtures of two or more radicals and separation via time-domain methods is only possible if the involved radicals differ sufficiently in their relaxation behaviour. In such a manner, temperature-dependent time-domain EPR measurements could help to separate the signal of a disulfide radical anion in the R1 subunit of RNR [22] from the overlapping signal of a  $\text{Y}^\bullet$ , which was near by a metallo-cofactor and therefore exhibited a much faster relaxation time. However,  $g$ -strain at high fields may prevent the detection of hyperfine structure such that for the analysis of the EPR spectra and the verification of a postulated molecular structure it is often helpful to acquire spectral data at different microwave frequencies as performed in the present study.

In the studies reported within this work, the spectral components observed in the field-swept echo-detected spectra at 180 GHz could not be separated via their relaxation behaviour using time-domain methods. Unfortunately, the small spin concentration rendered the detection of signals above 10 K impossible. In order to separate the spectral components temperature-dependent CW X-band and pulsed Q-band EPR measurements were performed. These temperature-dependent X- and Q-band spectra revealed the presence of at least three species in 4-F-BCoA-inhibited BCR. From the pulsed Q-band spectra of unlabeled enzyme, a slowly relaxing signal observed at high temperatures with  $g_{\text{av}}=2.008$  (signal III) and a very fast relaxing signal with a singularity at  $g = 2.030$  (signal IV) could be extracted. A weak contribution at  $g = 1.96$  was attributed to the former based on the observation that at X-band only these two singularities were present at 45 K.

The overall spectral features for the unlabeled enzyme at the three different frequency bands are very similar as depicted in Figure 3.11, showing the pulsed G-

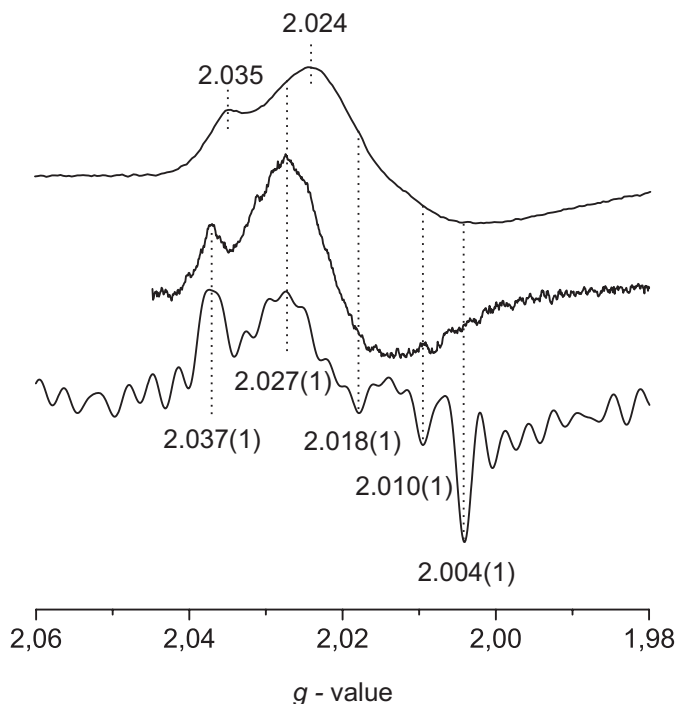


**Figure 3.11** CW X-band (top), pulsed Q-band (middle) and G-band (bottom) spectra of 4-F-BCoA-inhibited BCR reduced with 0.5 equivalents of dithionite at  $T = 10, 10$  and  $5$  K, respectively. Experimental parameters: Q-band: pseudo modulated field-swept echo detected spectrum using a shot repetition time of  $1$  ms; G-band: band-pass filtered derivative spectrum of the band-pass filtered field-swept-echo detected spectrum obtained with  $\text{SRT} = 10$  ms,  $1$  scan with  $25$  shots per point. For further experimental details see Section 3.2.

band spectrum measured at  $5$  K, the pulsed Q-band spectrum measured at  $10$  K as well as the CW X-band spectrum measured at  $10$  K. In the low temperature regime, two signals are observed, signal II ( $g = 2.024$ ) and signal I ( $g = 2.035$ ). Three further singularities at  $g = 2.018$ ,  $g = 2.010$  and  $g = 2.004$  resolved in the G-band spectra detectable at temperatures above  $5$  K are likely to be due to the high temperature signal as found at X- and Q-band ( $g_{\text{av}} = 2.006$ , signal III).

Furthermore, the effect of  $^{33}\text{S}$ -labeling on the observed spectral features in the CW X-band EPR spectra as well as in the CW and pulsed Q-band spectra was investigated at different temperatures. The CW Q-band spectrum obtained at  $20$  K was consistent with the X-band spectrum measured at  $10$  K. In comparison to the spectra from the unlabeled samples, the overall observed signals were very similar, however with different contributions. In the spectra from the

labeled enzyme, signals I and IV were more pronounced in comparison to signal II, whereas signal IV was more pronounced in comparison to signal III and an additional signal around  $g = 2.043$  (signal SV) appeared at high temperatures.

The signal proposed to be due to a disulfide radical anion had maximum intensity at 20 K [14]. Therefore, the focus was put on the simulation and interpretation of the broadening observed at this temperature. Although a broadening in the 20 K spectrum from the  $^{33}\text{S}$ -labeled enzyme could be observed, the origin of this effect needed a closer look. Since more pronounced and additional signals were observed in the spectra of the labeled enzyme, it needed to be clarified whether the observed broadening was due to two sulfur hyperfine couplings or due to overlapping spectral components. Before simulating the spectra including two  $I = \frac{3}{2}$  nuclei, the 20 K spectrum of the unlabeled enzyme was simulated following  $g$ -values of disulfide radical anions reported in the literature. A simulation with a parameter set with  $g$ -values and proton hyperfine couplings in the range of the ones reported in the literature did fit the experimental X- and Q-band spectra reasonably well on the  $g_x$  and  $g_y$  component, however less on the  $g_z$  position.

For the simulation of the  $^{33}\text{S}$ -labeled spectra, calculated HFCs obtained with DFT methods of disulfide radical anions [33] were included in the simulation, which predict a strongly anisotropic hyperfine coupling with  $A_{\perp} \approx 0$  G and  $A_{\parallel} \approx 50$  G. Such a large broadening was not observed in the X-band spectrum and therefore, the effect of a smaller  $^{33}\text{S}$ -HFC was tested. However, as a fingerprint, the effect of two  $I = \frac{3}{2}$  spins was a shift of the maximum of the EPR signal. This was not observed when comparing the 20 K X-band spectra of the unlabeled and the labeled enzyme. Alternatively, it was found that the broadening could originate from the additional species with a singularity at  $g = 2.043$  (signal SV) observed in the labeled spectra or from the other low-field signals IV or signal I found for the labeled enzyme.

Furthermore, the effect of the  $^{33}\text{S}$ -labeling on the X-band signals was investigated in the spectra acquired at 10, 30 and 45 K. No broadening could be found for signal I. Although the signal IV observed at 30 K appeared to be broadened, the origin of this broadening can not unambiguously be assigned to a sulfur HFC since the contribution of the high temperature signal III rendered the normalization of the spectra difficult. In contrast, the observed broadening of the  $g = 1.96$  singularity at high temperatures may be due to a sulfur coupling. This broadening along with the low  $g$ -value and the relatively slow relaxation of this signal could be indicative of a  $[\text{4Fe-4S}]^{+1/+2}$  cluster.

The lack of resolution of the  $g$ -values and the similar relaxation behaviour of all other spectral components, including the 20 K signal, render their interpretation difficult. One can speculate that signal I could originate from a [4Fe-4S] cluster as found by previous EPR studies [14], where a signal measured at 40 K with  $g$ -values of 2.037, 1.995 and 1.965 was assigned to an [4Fe-4S] cluster. The observation that signal II, which was postulated to be due to a disulfide radical anion, does not show three resolved  $g$ -values and relaxes very fast (the disulfide radical anion from RNR was detected at 60 K at 140 GHz [22]), as well as the lack of a simulation parameter set consistent with the proposed model, render the presence of an uncoupled disulfide radical anion in the samples unlikely. The very similar and fast relaxation behaviour of signal I and II as well as the temperature-dependent maximum of signal II could be indicative for an exchange coupling between the two radical species (see Chapter 3.5).

Still, since it can not be excluded that the  $^{33}\text{S}$  HFC might be hidden under the broad lines and/or overlapping signals in the X- and Q-band EPR spectra, one might speculate that the lack of EPR spectroscopical evidence found by the present multifrequency EPR studies does not disprove the mechanistic model proposed by Boll et al. [6] and the hypothesis of a disulfide radical anion being involved in the ring reduction of BCoA. Preliminary measurements and comparison of spectra from different enzyme preparations showed that the samples did not always contain the same contribution of species, and therefore the time window in which the samples were prepared might simply not include the proposed radical, since the hyperfine broadening might be obscured by the broad line widths or overlapping signals.

## 3.5 Outlook

In the following, additional ways to further identify the nature of the transient radical intermediates in the reduction of benzoyl-CoA via benzoyl-CoA reductase are proposed.

First of all, X-band  $^{57}\text{Fe}$ -ENDOR on the  $^{57}\text{Fe}$ -labeled enzyme could provide valuable information about hyperfine interactions of paramagnetic species with paramagnetic clusters present in the sample and help to verify whether the high temperature signal (signal IV) is indeed due to a [4Fe-4S] cluster. Furthermore, measuring the hyperfine interactions at different field positions could help to

disentangle the different spectral components with respect to their  $^{57}\text{Fe}$  hyperfine coupling. Thereafter, simulations including an exchange coupling parameter could help to test whether the radical species yielding signals I and II might be indeed exchange coupled.

From the biochemical part, selective site-directed mutation of cysteine residues would be helpful to verify the presence of a disulfide radical anion. In combination with EPR studies on the mutated enzymes, this could help to shed some more light on the mechanism of aromatic ring reduction in benzoyl-CoA reductase.

Since hyperfine spectroscopy such as ENDOR, HYSCORE (hyperfine sub-level correlation) or ESEEM (electron spin echo envelope modulation) provides a "fingerprint" whether  $^{33}\text{S}$  HFC exist at all, these techniques performed at X- and Q-band could be used for studying possible sulfur hyperfine couplings in the trapped radical intermediates and therefore gain more information about their nature. However, the detection of sulfur hyperfine couplings of sulfur centered radicals has proved to be rather demanding and only very limited number publications exists which report the detection of such sulfur hyperfine couplings. This might be ascribed to difficulties in labeling and/or the reactive nature of these radicals. The increased nuclear Zeeman resolution at high fields might help to detect the hyperfine couplings of such species with ENDOR.

## References

- [1] Heider, J.; Fuchs, G. *Eur. J. Biochem.* **1997**, *243*, 577–596.
- [2] Harwood, C. S.; Burchardt, G.; Herrmann, H.; Fuchs, G. *FEMS Microbiol. Rev.* **1999**, *22*, 439–458.
- [3] Koch, J.; Eisenreich, W.; Bacher, A.; Fuchs, G. *Eur. J. Biochem.* **1993**, *211*, 649–661.
- [4] Boll, M.; Fuchs, G. *Eur. J. Biochem.* **1995**, *234*, 921–933.
- [5] Boll, M.; Laempe, D.; Eisenreich, W.; Bacher, A.; Mittelberger, T.; Heinze, J.; Fuchs, G. *J. Biol. Chem.* **2000**, *275*, 21889–21895.
- [6] Boll, M.; Fuchs, G. *Biol. Chem.* **2005**, *386*, 989–997.
- [7] Boll, M.; Fuchs, G. *Eur. J. Biochem.* **1998**, *251*, 946–954.

- [8] Birch, A. J.; Hinde, A. L.; Radom, L. *J. Am. Chem. Soc.* **1980**, *102*, 3370–3376.
- [9] Buckel, W.; Keese, R. *Angew. Chem. Int. Ed.* **1995**, *34*, 1502–1506.
- [10] Boll, M.; Albracht, S. J. P.; Fuchs, G. *Eur. J. Biochem.* **1997**, *244*, 840–851.
- [11] Boll, M.; Schink, B.; Messerschmidt, A.; Kroneck, P. M. H. *Biol. Chem.* **2005**, *386*, 999–1006.
- [12] Boll, M.; Fuchs, G.; Meier, C.; Trautwein, A. X.; Lowe, D. J. *J. Biol. Chem.* **2000**, *275*, 31857–31868.
- [13] Locher, K. P.; Hans, M.; Yeh, A. P.; Schmid, B.; Buckel, W.; Rees, D. C. *J. Mol. Biol.* **2001**, *307*, 297–308.
- [14] Boll, M.; Fuchs, G.; Lowe, D. J. *Biochemistry* **2001**, *40*, 7612–7620.
- [15] Meier, C. *Mössbauerspektroskopie an biomimetischen Modellkomplexen und nicht-Häm-Eisenproteinen*, Thesis, Universität Lübeck, Germany, 2000.
- [16] Messerschmidt, A.; Huber, R.; Poulos, T.; Wieghardt, K., Eds.; *Handbook of Metalloproteins*; Wiley & Sons, LTD: 2001.
- [17] Kozbial, P. Z.; Mushegian, A. R. *BMC Struct. Biol.* **2005**, *5*, 1–16.
- [18] Frey, P. A. In *Comprehensive Natural Products Chemistry*, Vol. 5; Poulter, C. D., Ed.; Oxford: Elsevier Science: 1999.
- [19] Frey, P. A. In *Advances in Free Radical Chemistry*, Vol. 2; Zard, S. Z., Ed.; Stamford, CT: JAI Press: 1999.
- [20] Frey, P. A. *Annu. Rev. Biochem.* **2001**, *70*, 121–148.
- [21] Bennati, M.; Stubbe, J.; Griffin, R. G. *Appl. Magn. Reson.* **2001**, *21*, 389–410.
- [22] Lawrence, C. C.; Bennati, M.; Obias, H. V.; Bar, G.; Griffin, R. G.; Stubbe, J. *Proc. Natl. Acad. Sci. USA* **1999**, *96*, 8979–8984.
- [23] Johnson, K. A. In *The Enzymes*, Vol. 20; Sigman, D. S., Ed.; Academic Press, San Diego: 1992.



- [24] Bollinger, J. M. J.; Tong, W. H.; Ravi, N.; Huynh, B. H.; Edmondson, D. E.; Stubbe, J. *Methods Enzymol.* **1995**, *258*, 278–303.
- [25] Stubbe, J.; van der Donk, A. *Chem. Rev.* **1998**, *98*, 705–762.
- [26] Möbitz, H.; Boll, M. *Biochemistry* **2002**, *41*, 1752–1758.
- [27] Nelson, D. J.; Peterson, R. L.; Symons, M. C. R. *J. Chem. Soc. Perkin Trans.* **1977**, *2*, 2005–2015.
- [28] Rohrer, M.; Brüggmann, O.; Kinzer, B.; Prisner, T. F. *Appl. Magn. Res.* **2001**, *21*, 257–274.
- [29] Hertel, M. M.; Bennati, M.; Denysenkov, V.; Prisner, T. *Magn. Res. Chem.* **2005**, *43*, 248–255.
- [30] Schweiger, A.; Jeschke, G. *Principles of pulse electron paramagnetic resonance*; Oxford, University Press: 2001.
- [31] Rao, D. N. R.; Symons, M. C. R.; Stephenson, J. M. *J. Chem. Soc. Perkin Trans.* **1983**, *2*, 727–730.
- [32] Hadley, J. H.; Gordy, W. *Proc. Nat. Acad. Sci.* **1974**, *71*, 4409–4413.
- [33] Engström, M.; Vahtras, O.; Agren, H. *Chem. Phys. Lett.* **2000**, *328*, 483–491.
- [34] van Gastel, M.; Lubitz, W.; Lassmann, G.; Neese, F. *J. Am. Chem. Soc.* **2004**, *126*, 2237–2246.



## Chapter 4

# High-Field ENDOR Studies of the Catalytic Site in Ras

As a guanine nucleotide binding protein Ras plays a central role as molecular switch in cellular signal transduction, cycling between a GDP-bound "off" state and a GTP-bound "on" state. Specific oncogenic mutations in the Ras protein are found in up to 30% of all human tumors. Previous  $^{31}\text{P}$ -NMR studies had demonstrated that in liquid solution different conformational states in the GDP- as well as in the GTP-bound form coexist [1–3]. High-field EPR spectroscopy of the GDP complexes in solution revealed differences in the ligand sphere of the wild-type GDP-bound protein as compared to its oncogenic mutant Ras(G12V), i.e. only three water ligands were found in the former with respect to four in the G12V mutant [1]. In contrast, these differences were not detected in previous X-ray structures in the crystalline state [4–6]. The present study addressed the question about the nature of a phosphate ion or amino acid ligand that could replace a water molecule in the GDP-bound state of the wild-type protein by performing high-field ENDOR at 94 GHz in combination with selective  $^{31}\text{P}$ - and  $^{13}\text{C}$ - isotope labeling.

### 4.1 In Search of a Metal Ion Ligand at the Catalytic Site in Ras

Ras (rat sarcoma) is a prototypical member of the family of small G proteins (guanine nucleotide-binding proteins or GNBPs) with molecular weights of 20 to

25 kDa which provide the catalytic machinery for orchestrating diverse cellular signal transduction pathways in eucaryotes (for recent reviews see [7–18]). Signal flow is controlled by the function of Ras as a molecular switch cycling between a guanosine 5'-diphosphate (GDP)-bound inactive and a guanosine 5'-triphosphate (GTP)-bound active state (see Figure 4.1) regulating cell proliferation, differentiation and apoptosis [19]. The GTP-bound form is the functionally active form, in which the protein interacts with and activates downstream targets, so-called "effector" molecules, which in turn regulate their activities within the cell. For the inactive protein to become activated, GDP has to be exchanged for GTP. This reaction requires guanine nucleotide exchange factors (GEFs) [20] to catalyze the release of usually tightly bound GDP, which is subsequently replaced by abundant cellular GTP. The protein is "switched off" again via hydrolysis of GTP which returns Ras•GTP to its inactive GDP-bound form and results in effector release, thereby terminating downstream signaling [13]. In the absence of other factors, the duration of the active signaling state depends on the intrinsic hydrolytic rate of the G protein. The intrinsic GTPase reaction is rather slow but is accelerated on interaction with Ras-specific GTPase activating proteins (GAPs) by factors ranging from 10 to  $10^5$  [21–23], e.g. RasGAP increases the GTPase rate of Ras from  $10^{-4} \text{ s}^{-1}$  to  $10 \text{ s}^{-1}$  [10].

The longer a G protein remains in its active GTP-bound state, the longer its particular signal is transmitted and amplified. Hence, the rate of hydrolysis is of great importance for the right timing of many processes in a cell. Mutation of critical residues at the active site can slow down the GTPase reaction such that the signal transduction pathway becomes permanently activated. Biochemical analysis have shown that single point mutations at positions 12, 13 and 61 prevent GTP hydrolysis such that the protein can no longer be switched off by GAPs [26]. The mutated Ras protein which constantly remains in its active state consequently contributes to sustained cell proliferation and tumor formation. In such a manner, mutations at the codons 12 and 61, and more rarely at 13 are found in 30% of all human tumors [27–30]. According to numerous X-ray studies of the active and the inactive Ras protein [4–6, 24, 31–37], the aforementioned residues make up part of the guanine nucleotide binding pocket, located at the active site of the protein where GTP hydrolysis takes place. At the active site, Ras binds  $\text{Mg}^{2+} \cdot \text{GDP}$  and  $\text{Mg}^{2+} \cdot \text{GTP}$  with high specificity and high affinity if an excess of  $\text{Mg}^{2+}$  is present.

For the understanding of tumor formation the knowledge of differences in

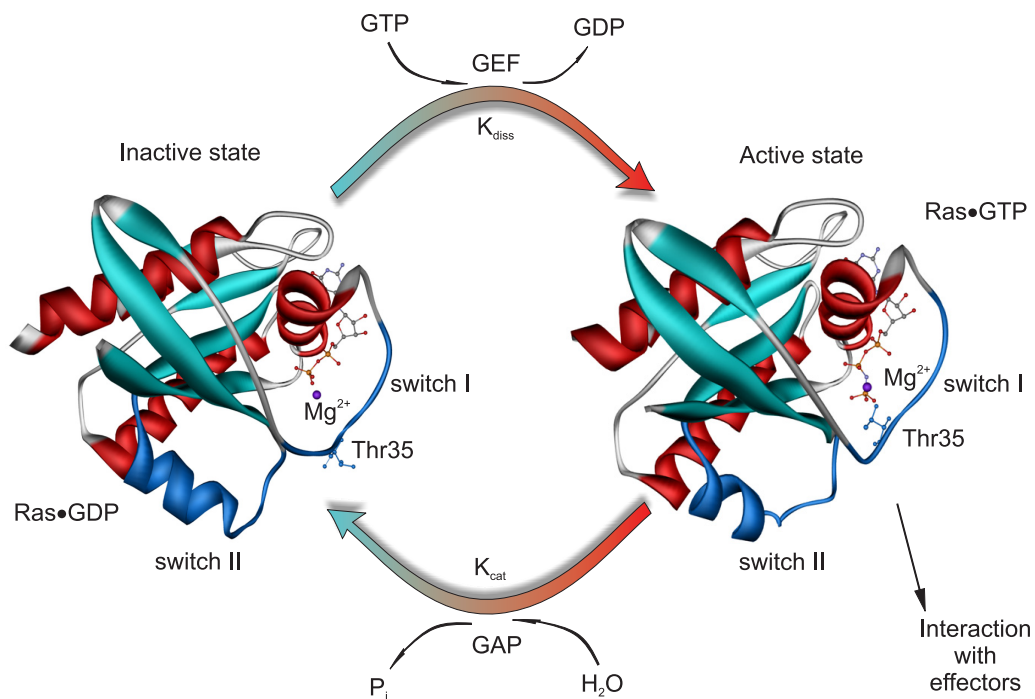


**Figure 4.1** Activation and deactivation cycle of Ras. Ras is activated via exchange of bound GDP to GTP, which is achieved via guanine nucleotide exchange factors (GEFs). Hydrolysis of GTP brings the protein back into its inactive GDP bound state, which is accelerated by orders of magnitudes via binding of GTPase activating proteins (GAPs). The blue regions indicate switch I (residues 30–38) and switch II (residues 60–76) where the major differences between the two conformational states were observed in X-ray structures [24, 25].

the structure and conformation at the active site in the GTP- and GDP-bound states in Ras as well as in the oncogenic mutants is of great importance. The structure of Ras was solved for the wild-type protein [5, 24, 31, 32] as well as for oncogenic mutants at position 12 [4–6, 24, 32–36] and 61 [32, 33] in the diphosphate [5, 24, 31–33] or triphosphate form, by using slowly hydrolysing GTP analogues such as GppNHp or GppCH<sub>2</sub>p [4, 6, 24, 25, 32–37]. These studies showed that the main structural differences between the GTP-bound and GDP-bound state in Ras are found primarily in the switch I (residues 30–38) and switch II (residues 60–76) regions [24, 25]. Furthermore, the crystal structures in complex with effectors Raf [38], RalGDS [39, 40] and PI(3)-kinase [41, 42] revealed that the interactions with Raf and RalGDS mainly take place in switch I and additionally in switch II in complex with PI(3)-kinase. The main differences

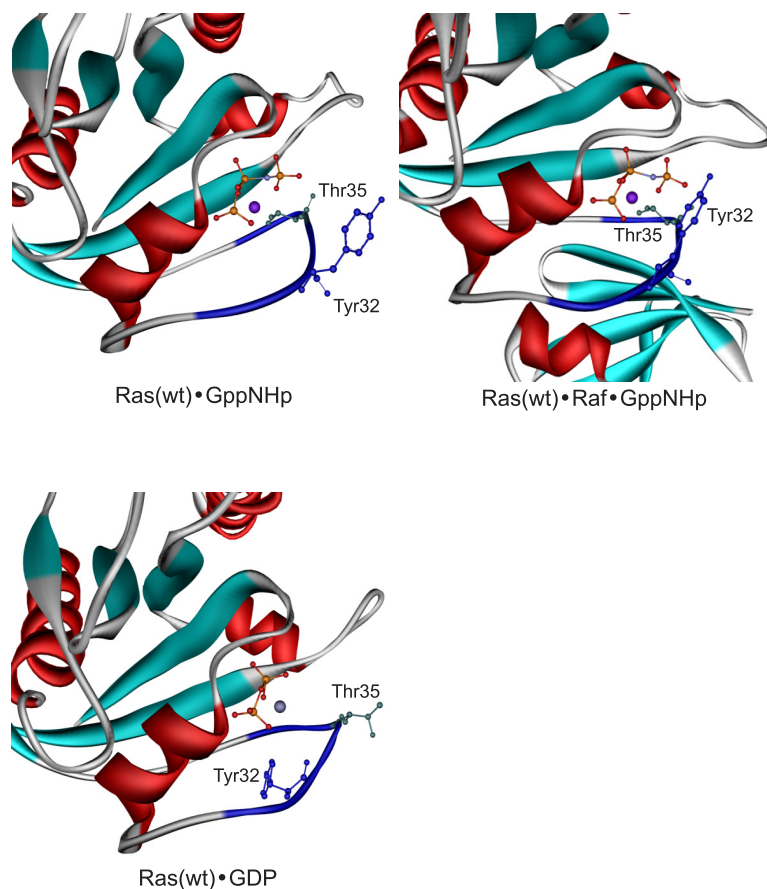


**Figure 4.2** Differences in the switch I region (in blue) observed in the crystal structures of Ras(wt)•GppNHp and in complex with the effector Raf as well as in Ras(wt)•GDP (PDB files 5P21 [4], 1GUA [38] and 4P21 [5], respectively). The main differences between the three states are the positioning of Tyr32 and the binding of Thr35 to the metal ion as discussed in the text.

observed in the switch regions of the different Ras complexes according to the crystal structures comprise the positioning of Tyr32 and the binding of Thr35 to the metal ion as illustrated in Figure 4.2 and will be discussed in more detail in the following.

#### 4.1.1 Structure of the active site in Ras according to X-ray

According to the X-ray crystallographic studies, the  $Mg^{2+}$  ion is coordinated by six oxygen atoms in an octahedral arrangement as depicted in Figure 4.3. In the crystal structure of the GTP-bound protein [4, 24, 43], the metal ion is complexed

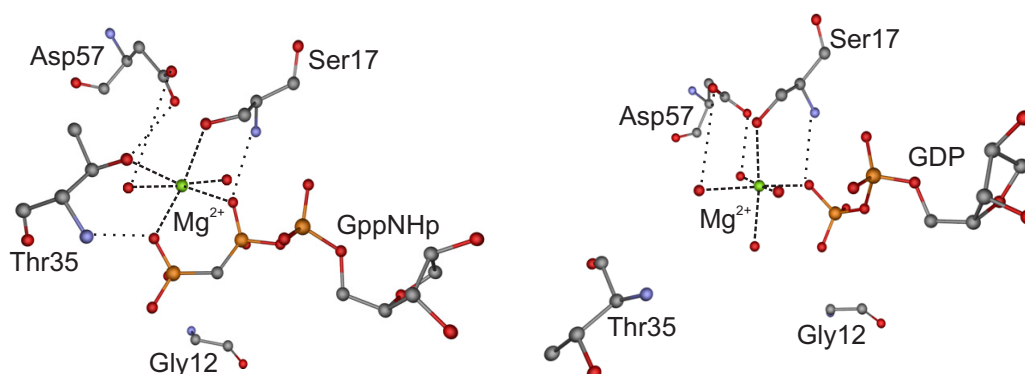


**Figure 4.3** Nucleotide binding site of Ras•GppNHp (left) and Ras•GDP (right) according to crystal structures (PDB files 5P21 [4] and 4Q21 [24]), where the dotted lines indicate hydrogen bonding.

to two phosphate oxygens of GppNHp and forms two additional bonds to the side chain oxygens of Ser17 and Thr35, both of which are highly conserved in all guanine nucleotide-binding proteins. Serine is part of the P-loop (residues 10–17) and coordinates through a hydroxyl group to the metal ion as well as through its amide group to the oxygen of the  $\beta$ -phosphate of GppNHp. Threonine as part of the switch I and the effector region (residues 32–40) binds through its hydroxyl group to the metal ion and through its amide group to an oxygen of the  $\gamma$ -phosphate (see Figure 4.3, left hand side). The two apical positions of the octahedron are occupied by oxygens from water molecules. One of these water molecules is coordinated to the  $\alpha$ -phosphate oxygen and the other to Asp57, another highly conserved residue of GNB proteins. In the GDP-bound state, the switch II region is far removed from the active site with Thr35 being no longer a direct ligand of the metal ion [5, 24]. According to the crystal structures of Ras•GDP [5, 24],  $Mg^{2+}$  is coordinated to an oxygen of the  $\beta$ -phosphate group of GDP, to the oxygen of the hydroxyl group of Ser17, and to four water molecules (see Figure 4.3, right hand side).

In one of the crystal structures of Ras•GDP, which was solved using caged GTP allowing Ras•GTP to hydrolyze to Ras•GDP in the crystal, Asp57 is directly coordinated to the metal ion in the GDP-bound form but via an intervening water molecule in the GTP-bound form [31]. Also in the small human GTPase protein RhoA in the  $Mg^{2+}$ •GDP complex, for which Thr35 was shown to directly coordinate to the metal ion via its main chain carbonyl, only three water mole-

cules were found to bind to the metal ion [44]. Surprisingly, the crystallographic studies of the oncogenic protein with mutations at positions 12 [4–6, 24, 32–36] as well as at position 61 [32, 33] did not reveal any significant structural differences between the wild-type protein and the oncogenic mutants.

### 4.1.2 Protein dynamics

When investigating the structure of a protein one has to bear in mind that most of the proteins are not rigid but rather "breathing" molecules, since they often bind specifically and interact with several different proteins. This is especially important for proteins like Ras which switches between different, energetically finely balanced conformational states, and needs to interact with several diverse effectors as well as bind to GAPs or GEFs.

With X-ray crystallography, the resolution of the protein structure is limited to rigid conformations and only R-factors provide some information about areas of flexibility within the amino acid sequence. Furthermore, crystal packing forces are likely to influence the structure detected with X-ray. In such a manner, intermolecular contacts between the effector region and the neighbouring Ras molecules were found for Ras•GppNHp and Ras•GppCH<sub>2</sub>p in crystals, and four independent conformations were found for the latter [24, 25].

Therefore, several methods are advantageous over X-ray crystallography for observing dynamical processes in proteins. Among the most suited methods for studying protein dynamics are NMR (Nuclear Magnetic Resonance) and EPR (Electron Paramagnetic Resonance) spectroscopy as well as Fourier Transform Infrared (FTIR) or Raman spectroscopy. Also molecular dynamics (MD) simulations can yield valuable information about the dynamical processes in proteins. These methods have been used in the past for studying dynamics and gave evidence for the important role of structural dynamics in Ras [2, 3, 45–63]. In particular, MD calculations showed that mutations at position 12 are connected with an increase of protein flexibility in comparison to the wild-type protein [51, 53, 56].

The structure at the active site has been studied by several groups with EPR spectroscopical methods [1, 46–48, 64–69], for which the diamagnetic magnesium ion needs to be substituted with a paramagnetic manganese ion. A crystal structure of a Ras(G12P)•GppCH<sub>2</sub>p complex containing a manganese ion showed a very similar ligand sphere as the same complex containing a magnesium ion [70].



Performing high-field CW EPR spectroscopy, Rohrer et al. [1] showed for the first time a difference in the structure at the catalytic center between the wild-type and the oncogenic mutant of the protein-nucleotide complex in its inactive GDP-bound state. Specifically, one can extract the number of water molecules bound to the manganese ion by analysing the  $^{17}\text{O}$ -induced inhomogeneous broadening on the ( $m_S = +\frac{1}{2} \leftrightarrow -\frac{1}{2}$ ) EPR transitions, a method pioneered by Reed et al. [71] and applied later on for the studies of Ras at Q-band by Smithers et al. [65] and Latwesen et al. [66] as well as at high fields by Bellew et al. [69] and Rohrer et al. [1]. Using this approach, four bound water ligands were found for the mutated Ras(G12V,A59T)•GDP [65, 66] and Ras(G12V)•GDP [1] complexes in agreement with crystal structures [5, 24, 32]. However, for the wild-type GDP-bound protein, Rohrer et al. [45] found only three bound water ligands.

Furthermore,  $^{31}\text{P}$ -NMR spectroscopy in liquid solution [1–3, 49, 72–76] as well as in the crystalline state [50, 77] along with EPR in liquid solution [1, 47] revealed the existence of more than one conformational state in the active and inactive GDP-bound protein. Two interconverting conformations, called state 1 and state 2, are characterised by different chemical shift values for the resonances of the  $\beta$ -phosphate group of GDP. These dynamical equilibria were found to be perturbed by minor changes in the amino acid sequence or the type of nucleotide analogue bound to Ras [1, 3, 75]. While the oncogenic mutant Ras(G12V)•GDP was observed in a single conformational state, the wild-type protein was found in two different conformational states [1] with an equilibrium constant  $K_{12} = 0.3^1$ . Two conformational states around the  $\gamma$ -phosphate group of the Ras(wt)•GDP complex were also postulated from the FTIR spectra of the phosphate vibrations [63]. Similarly, two equally populated states were found in Ras(wt)•GppNHp, for which the equilibrium is entirely shifted to a single state on association with the effector Raf [2]. Here, the two states are characterized by different chemical shift values for the resonances of the  $\gamma$ - and  $\alpha$ -phosphate groups of GppNHp.

Since association of Raf induced a transition of state 1 to state 2, it was suggested that state 1 and 2 correspond to the "off" and "on" conformations of Ras•GTP, respectively. Geyer et al. [2] proposed that the two states observed in Ras(wt)•GppNHp are connected with different conformations of loop L2 with Tyr32 being hydrogen-bonded via an oxygen atom to  $\text{P}_\gamma$  in state 2, while it is removed in state 1. While state 2 corresponds to the structure found in crystals

---

<sup>1</sup>Defined by the ratio [2]:[1] between the two states.

as well as in complex with effectors [2, 3], the state 1 conformation was predicted to be characterized by the loss of the interaction between Thr35 and the  $\gamma$ -phosphorus of GTP [3]. This suggestion was supported by the solution of the structure of M-Ras•GppNHp which was predominantly found in state 1 in solution [78]. In this structure, Thr45 (corresponding to Thr35 in H-Ras) is no longer a direct ligand of the metal ion but instead a third water ligand binds to the metal center. Similarly, a recent crystal structure of the mutant Ras(G60A)•GppNHp showed that Thr35 is no longer a ligand of  $Mg^{2+}$  [79].

For the GDP-bound state, Rohrer et al. [1] proposed that the two states found for the wild-type protein are connected with a different ligation sphere of the metal ion, assigning a fourfold water coordination to state 1 and a threefold coordination to state 2. In such manner it was proposed that in the wild-type protein which predominantly exists in state 2, an additional non-water ligand has to exist.

### 4.1.3 Aim of the present study

The question about the nature of a ligand which would replace a water in the Ras(wt)•GDP complex is the starting point for the present work aiming at the investigation of the structure at the active site. We addressed this question using high-frequency ENDOR spectroscopy in combination with selective isotope labeling in order to detect the resonances of nuclei in the first ligand sphere of the ion with high spectral resolution. As additional binding partner replacing a water molecule we consider a free phosphate ion or an amino acid. For testing the former hypothesis, we compared  $^{31}P$ -ENDOR spectra from the wild-type Ras•GppNHp and Ras•GDP complex. Furthermore, in order to find the additional amino acid ligand that could replace a water ligand, we performed  $^{13}C$ -ENDOR (Section 4.3.2). In particular, we tested whether Asp57 is directly coordinated to the metal center by comparing spectra of uniformly  $^{13}C$ -labeled Ras(wt)•GDP with spectra from selectively 1,4- $^{13}C$ - aspartate labeled Ras(wt)•GDP. In order to find out whether any other amino acid ligand than Asp57 is a binding partner of the metal ion, spectra from uniformly  $^{13}C$ -labeled Ras(wt)•GDP and Ras(G12V)•GDP complexes were compared with spectra of uniformly  $^{13}C$ -labeled Ras(wt)•GppNHp.

## 4.2 Pulsed ENDOR at 94 GHz

All experiments were performed in collaboration with Dr. Norbert Weiden using the W-band (94 GHz) spectrometer situated in the group of Prof. Klaus Peter Dinse. The samples were prepared in the group of Prof. Hans-Robert Kalbitzer by Dr. Michael Spörner and Roland Hofweber as described in Ref. 80. The Bruker E680 spectrometer was equipped with a 94 GHz microwave amplifier (about 20 dBm output power) from Donetsk Physico Technical Institute. The  $^{31}\text{P}$ -ENDOR spectra as well as the  $^{13}\text{C}$ -ENDOR spectra of 1,4- $^{13}\text{C}$ - aspartate labeled Ras(wt)•GDP were obtained using a home-built ENDOR probe equipped with a four-turn radio frequency (RF) coil, whereas the  $^{13}\text{C}$ -ENDOR spectra of Ras(wt/G12V)•GDP and Ras(wt)•GppNHp were acquired with a probehead from Bruker Biospin GmbH, in which the resonator functioned as RF coil. The RF amplifier was an ENI-LPI-10 providing an output power of 1 kW which was attenuated by 7 to 10 dB. Davies ENDOR spectra were typically acquired with a pulse sequence ( $\pi_{\text{MW}} - \pi_{\text{RF}} - \pi/2_{\text{MW}} - \pi_{\text{MW}}$ ) consisting of selective pulses, with typical  $\pi/2$  pulse lengths of 50–100 ns for  $90^\circ$  excitation of the electron spin  $S = 5/2$  of  $\text{Mn}^{2+}$ . The pulse sequence was employed to detect hyperfine couplings larger than 4–5 MHz as to be expected in the  $^{31}\text{P}$ -ENDOR spectra. Mims ENDOR ( $\pi/2_{\text{MW}} - \pi/2_{\text{MW}} - \pi_{\text{RF}} - \pi/2_{\text{MW}}$ ) was used to detect weak hyperfine couplings as encountered in the  $^{13}\text{C}$ -ENDOR spectra. The length of the RF pulse varied for the different nuclei and was optimised for a maximum ENDOR effect. All experiments were performed at temperatures between 3–4.5 K with a shot repetition time between 5–25 ms. More detailed parameters are given for each experiment in the figure captions.

### Simulation of ENDOR spectra

Simulations were performed using home-written MATLAB routines described previously [81]. For simplicity, the simulations were performed only for the ENDOR lines arising from the EPR  $m_S = +\frac{1}{2}$  to  $-\frac{1}{2}$  transition of the  $S = \frac{5}{2}$   $\text{Mn}^{2+}$  spin, where  $m_S$  is the electron spin quantum number. At high fields, these ENDOR lines are well resolved and expected at the first order frequencies as given by Equation 2.14, in which the nuclear Zeeman frequency  $\nu_I$  of nucleus  $I$ , the nuclear spin quantum number  $m_I$ , the orientation-dependent hyperfine and quadrupole tensor components  $A_{zz}$  and  $Q_{zz}$  go in. As described in Chapter 2,

the high-field approximation is generally valid when the nuclear Zeeman frequencies are substantially larger than the observed hyperfine couplings, which is the case here for  $^{31}\text{P}$  ( $\nu_I = 57.4$  MHz) and  $^{13}\text{C}$  ( $\nu_I = 36.2$  MHz). The zero-field splitting (ZFS) term of the electron spin Hamiltonian for the Ras•Mn<sup>2+</sup>•GDP complex is small ( $D = 11$  mT,  $E = 0$ ) and contributes to the  $m_S = +\frac{1}{2}$  to  $-\frac{1}{2}$  transition only as second order perturbation [1]. Further,  $g$ -anisotropy and the anisotropy of the  $^{55}\text{Mn}$  hyperfine coupling can be neglected [1]. Thus, orientational selectivity has not to be taken into account to compute the ENDOR transitions associated with the electron  $m_S = \pm\frac{1}{2}$  manifolds. The validity of this assumption is demonstrated by the satisfactory agreement between the computed and the experimental ENDOR line shapes.

### Validity of point-dipole-model

As discussed in Chapter 2, the traceless dipolar part of the HFC-tensors can be used to estimate the distance between the Mn<sup>2+</sup> ion and the  $^{31}\text{P}$  nuclei in a simple point-dipole model via Equation 2.14. The validity of this model for atoms that are at least two bond lengths removed from the Mn<sup>2+</sup> ion has been established in previous works of Singel and coworkers [46, 67] and Goldfarb and coworkers [82].

## 4.3 In Search of an Additional Ligand

### 4.3.1 In search of a phosphate ligand using $^{31}\text{P}$ -ENDOR

In principle, after GTP hydrolysis of Ras a transient GDP•P<sub>*i*</sub> complex is formed where the inorganic phosphate P<sub>*i*</sub> is non-covalently bound to the nucleotide. Under equilibrium conditions such a complex is always formed when P<sub>*i*</sub> is present in solution and its population is defined by the concentration of free P<sub>*i*</sub> as well as by the corresponding association constant. Although the preparation of Ras was performed with phosphate-free buffers and no free or bound P<sub>*i*</sub> can be detected by  $^{31}\text{P}$ -NMR spectroscopy of Ras•GDP in solution, it cannot be excluded that in GDP-bound form a further non-covalently bound phosphate exists as contamination from the cell-lysate in the active site of Ras. It could replace a water molecule and an additional  $^{31}\text{P}$  resonance should be observed in the ENDOR spectra.

Mims and Davies ENDOR were used by coworkers to detect the  $\alpha$ - and  $\beta$ -

phosphorus resonances in the Ras(wt)•GDP and Ras(G12V)•GDP complex and additionally the resonance of the  $\gamma$ -phosphorus in the Ras(wt)•GppNHp complex [80]. These ENDOR spectra did not reveal any difference between the oncogenic mutant and the wild-type GDP-bound protein and the obtained distances via the point-dipole model were in agreement with the distances extracted from the crystal structures. Within the present work we focus on the comparison of the ENDOR spectra from the wild-type protein in its active and its inactive state as reported in the following.

According to X-ray crystallographic as well as NMR spectroscopical studies (see Section 4.1), the metal ion binds to the  $\beta$ -phosphorus of GDP via one oxygen and to GppNHp via two oxygens (to the  $\beta$ - and  $\gamma$ -phosphorus, respectively). An additional phosphate ion ligand in Ras(wt)•GDP should show up as additional resonance in the  $^{31}\text{P}$ -ENDOR spectrum similar as observed for the GppNHp complex. Therefore, the  $^{31}\text{P}$ -Davies ENDOR spectrum of Ras(wt)•GDP was compared with the spectrum of Ras(wt)•GppNHp which are depicted in Figure 4.4.

The  $^{31}\text{P}$ -Davies ENDOR spectrum of the GppNHp complex (Figure 4.4, top) shows small but significant differences to the spectrum of the GDP complex (Figure 4.4, middle), i.e. the maximum of the powder pattern is shifted and the peak pattern is broadened. Since this spectrum consists of the resonances from the  $\beta$ - and  $\gamma$ -phosphorus, it was assumed that the former has similar hyperfine coupling constants as in the GDP-bound complex, and the contribution of the  $\beta$ -phosphorus (middle spectrum) normalized to 50% of the area of the top spectrum was subtracted from the GppNHp spectrum, yielding the bottom spectrum. The resulting powder pattern was simulated with one  $^{31}\text{P}$  nucleus with tensor components  $A_{\perp} = 3.3(1)$  MHz and  $A_{\parallel} = 5.8(1)$  MHz. The anisotropic part of the hyperfine tensor,  $T_{\perp} = -0.8(1)$  MHz, translates via the point-dipole model into a distance of  $3.4(1)$  Å which is in close agreement with the distances from the  $\gamma$ -phosphorus to the metal ion extracted from the crystal structures ( $3.3$  Å [4],  $3.2$  Å [34]). The hyperfine coupling tensor components for all  $^{31}\text{P}$  nuclei are listed in Table 4.1.

Assuming that the  $\beta$ -phosphorus possesses the same hyperfine couplings as in the GDP-bound state, the coupling in the bottom spectrum is assigned to

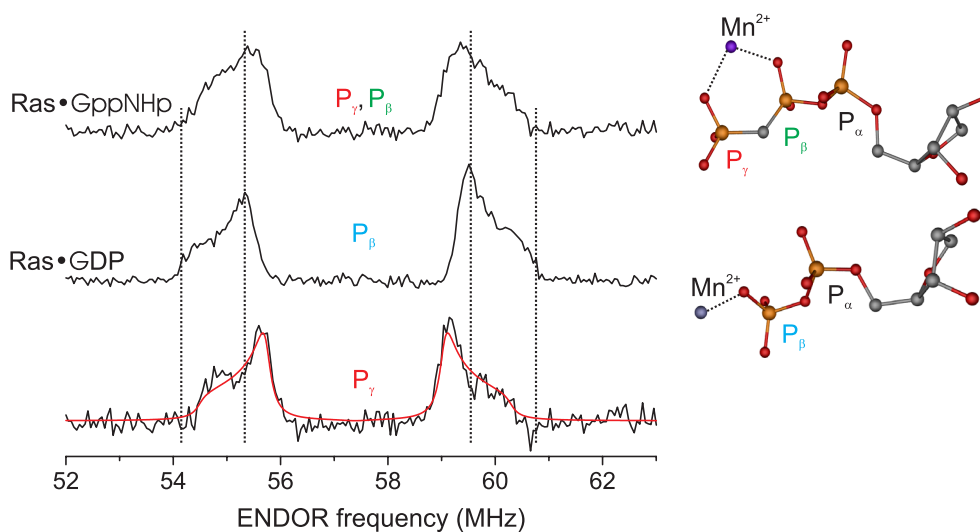


**Figure 4.4** Comparison of  $^{31}\text{P}$ -Davies ENDOR spectra of Ras(wt) •  $\text{Mn}^{2+}$  • GppNHp (top) and Ras(wt) •  $\text{Mn}^{2+}$  • GDP (middle) at 4.0 K. Subtraction of the middle spectrum, normalized to 50% of the area of the top spectrum, yields the difference spectrum shown at the bottom. Superimposed is the simulation with the hyperfine tensor components  $A_{\perp} = +3.9$  MHz and  $A_{\parallel} = +6.4$  MHz as described in the text and listed in Table 4.1. Right: schematic pictures of the metal ion coordination to GppNHp and GDP according to the X-ray structures [5, 83]. Experimental parameters: Ras • GppNHp:  $t_{\pi} = 160$  ns,  $t_{\pi/2} = 90$  ns,  $t_{\text{RF}} = 16$   $\mu\text{s}$ ,  $\tau = 400$  ns, shot repetition time = 15 ms, 50 scans with 20 shots per point. Ras • GDP:  $t_{\pi} = 200$  ns,  $t_{\pi/2} = 110$  ns,  $t_{\text{RF}} = 15$   $\mu\text{s}$ ,  $\tau = 400$  ns, shot repetition time = 16 ms, 25 scans with 20 shots per point.

**Table 4.1** Hyperfine tensor components (in MHz) obtained from  $^{31}\text{P}$ -ENDOR studies of Ras(wt) • nucleotide. The calculated distances were obtained via the point-dipole model and compared with the distances  $R_{\text{lit}}$  reported in the literature.

nucleus	nucleotide	$A_1$	$A_2$	$A_3$	$a_{\text{iso}}$	$T_{\perp}$	$R_{\text{exp}}$ [ $\text{\AA}$ ]	$R_{\text{lit}}$ [ $\text{\AA}$ ]
$^{31}\text{P}_{\beta}$ (this work)	GppNHp	+3.9	+3.9	+6.4	+4.7	−0.8	3.4(1)	3.3 [4]
								3.3 [34]
$^{31}\text{P}_{\gamma}$ (this work)	GppNHp	+3.3	+3.3	+5.8	+4.1	−0.8	3.4(1)	3.3 [4]
								3.3 [34]
$^{31}\text{P}_{\beta}$ [80]	GDP	+3.9	+3.9	+6.4	+4.7	−0.8	3.4(1)	3.5 [5]
								3.2 [24]
								3.5 [37]
								3.3 [67]

the  $\gamma$ -phosphorus of GppNHp. The simulation of the  $\beta$ -phosphorus resonance observed in the spectrum from the GDP-bound protein was obtained by Dr. M. Bennati [80], yielding the hyperfine tensor components  $A_{\perp} = 3.9(1)$  MHz and  $A_{\parallel} = 6.4(1)$  MHz, which gives the same point-dipole distance of  $3.4(1)$  Å as found for the  $\gamma$ -phosphorus of GppNHp. This distance is in agreement with ESEEM data from Larsen et al. ( $3.3$  Å) [67] and partially with crystal structures ( $3.5$  Å [5],  $3.2$  Å [24] and  $3.6$  Å [37]). Within the experimental error and assuming that the point-dipole model holds, our ENDOR spectra reveal the same distance between the metal ion and the  $\gamma$ - and  $\beta$ -phosphorus.

### 4.3.2 In search of an amino acid ligand using $^{13}\text{C}$ -ENDOR

In all crystal structures of the GDP-bound complex, Ser17 is directly ligated to the  $\text{Mg}^{2+}$  ion via its side chain hydroxyl group. In the structure of Schlichting et al. [31] Asp57 seemed additionally coordinated to the metal ion via the side chain carboxyl group, and it was proposed [1] that such a coordination pattern may be preserved for the wild-type protein complex in solution. To test this hypothesis, the resonances of strongly coupled  $^{13}\text{C}$  nuclei observed in the  $^{13}\text{C}$ -ENDOR spectra of the uniformly  $^{13}\text{C}$ -labeled Ras(wt)•GDP complex were compared with the ones observed in the spectra of the same complex containing selectively labeled 1,4- $^{13}\text{C}$  aspartates. Furthermore, in order to test whether an additional amino acid ligand is bound to the metal ion in the wild-type protein in comparison to the oncogenic mutant G12V, the ENDOR spectra of Ras(wt)•GDP were compared with spectra from Ras(G12V)•GDP and Ras(wt)•GppNHp.

#### Is Asp57 a ligand of the metal ion?

The  $^{13}\text{C}$ -ENDOR spectra of the uniformly  $^{13}\text{C}$ -labeled Ras(wt)•GDP complex are displayed in Figure 4.5 along with spectra of the same complex containing selectively labeled 1,4- $^{13}\text{C}$  aspartates. The Mims ENDOR spectrum of uniformly  $^{13}\text{C}$ -labeled Ras(wt)•GDP shows a 2 MHz broad powder pattern centered around the free Larmor frequency of  $^{13}\text{C}$ . As starting point for the simulation the calculated DFT hyperfine coupling tensor values from Ser17 were used (see Table 4.2). The simulation depicted in Figure 4.5 contains a single  $^{13}\text{C}$  tensor with  $|A_{\perp}| = 0.19$  MHz,  $|A_{\parallel}| = 1.76$  MHz and a matrix peak about 0.6 MHz wide which results from further distant nuclei ( $r \geq 0.4$  nm). Assuming that hyperfine tensor components have a positive sign, the  $|T_{\perp}|$  component (0.65 MHz) of

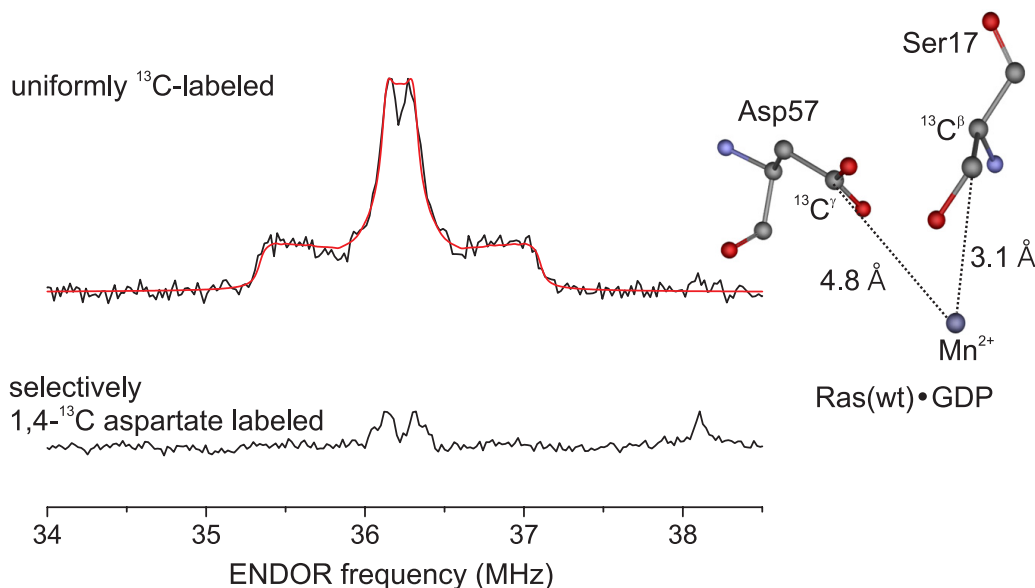


**Figure 4.5** Comparison of  $^{13}\text{C}$ -Mims ENDOR spectra of uniformly  $^{13}\text{C}$ -labeled Ras(wt)•Mn $^{2+}$ •GDP with spectra from the selectively 1,4- $^{13}\text{C}$  aspartate labeled complex at 4.5 K and 3.0 K, respectively. Superimposed on the uniformly labeled spectrum is the simulation with the hyperfine tensor components  $A_{\perp} = -0.19$  and  $A_{\parallel} = +1.76$  MHz as described in the text and listed in Table 4.2. Right: Schematic representation of the direct and indirect binding of the metal ion to Ser17 and Asp57, respectively, according to the X-ray structure [5]. Experimental parameters: Top:  $t_{\pi/2} = 96$  ns,  $\tau = 250$  ns,  $t_{\text{RF}} = 18$   $\mu\text{s}$ , shot repetition time = 5 ms, 240 scans with 50 shots per point. Bottom:  $t_{\pi/2} = 32$  ns,  $\tau = 500$  ns,  $t_{\text{RF}} = 46$   $\mu\text{s}$ , shot repetition time = 15 ms, 102 scans with 25 shots per point.

the extracted  $^{13}\text{C}$  dipolar tensor gives a point-dipole distance of 3.1 Å, which is close to the distances of 3.5, 3.5 and 3.3 Å between the metal ion and the  $^{13}\text{C}^{\beta}$  of Ser17 from X-ray data of Tong et al. [5], Milburn et al. [24] and Hall et al. [37], respectively. Considering the DFT calculations as well as the comparison with the distances from the X-ray structures the observed coupling is assigned to the  $^{13}\text{C}^{\beta}$  of Ser17.

In contrast to the uniformly  $^{13}\text{C}$ -labeled sample, the Mims ENDOR spectrum of the specifically 1,4- $^{13}\text{C}$ - aspartate labeled Ras(wt)•GDP complex displays only a weak peak at the free  $^{13}\text{C}$  Larmor frequency from further distant  $^{13}\text{C}$  nuclei. If Asp57 were coordinated to the Mn $^{2+}$  ion via an oxygen of its carboxyl group, the  $^{13}\text{C}^{\gamma}$  of the carboxyl group should contribute to the ENDOR spectrum with a similar hyperfine coupling as the  $^{13}\text{C}^{\beta}$  of Ser17. The absence of such a coupling in the spectrum indicates that Asp57 is not a direct ligand of the metal ion in



**Table 4.2** Hyperfine tensor components (in MHz) obtained from  $^{13}\text{C}$ -ENDOR studies of Ras•GDP and Ras•Raf•GppNHp complexes. The signs of the simulated components were derived from the calculated components obtained from DFT calculation given in parentheses (see Appendix A). The calculated distances (in Å) were obtained via the point-dipole model and compared with the distances reported in the literature.

nucleus	nucleotide	$A_1$	$A_2$	$A_3$	$a_{\text{iso}}$	$T_{\perp}$	$R_{\text{exp}}$	$R_{\text{lit}}$
$^{13}\text{C}$ Ser17	GDP	-0.19	-0.19	+1.76	+0.46	-0.65	3.1(1)	3.5 [5]
		(+0.07)	(+0.19)	(+1.63)	(+0.62)	(-0.49)		3.5 [24]
								3.3 [37]
$^{13}\text{C}$ Ser17	GppNHp	+0.52	+0.52	+2.02	+1.02	-0.50	3.4(1)	3.3 [4]
		(+0.27)	(+0.42)	(+2.10)	(+0.93)	(-0.59)		3.3 [34]
								3.3 [38]
$^{13}\text{C}$ Thr35	GppNHp	-0.07	+0.52	+1.72	+0.62	-0.55	3.3(1)	3.2 [4]
		(+0.03)	(+0.13)	(+1.91)	(+0.67)	(-0.63)		3.2 [34]
								3.2 [38]

the frozen protein solution. The visible splitting of 0.21 MHz in the spectrum from selectively labeled Ras corresponds to a point-dipole distance of 4.8(1) Å which agrees with the distances of 4.9, 4.8 and 4.7 Å to the  $4\text{-}^{13}\text{C}$  of Asp57 from the X-ray structures of Tong et al. [5], Milburn et al. [24] and Hall et al. [37], respectively.

#### Any amino acid binding partner other than Ser17?

To test whether an amino acid other than Asp57 coordinates to the ion in the wild-type Ras•GDP complex and not in its G12V mutant,  $^{13}\text{C}$ -Mims ENDOR spectra were recorded for the uniformly  $^{13}\text{C}$ -labeled Ras(G12V)•GDP and Ras(wt)•GppNHp complexes, the latter in complex with the Ras binding domain (RBD) of the effector Raf-kinase, and compared with the one from the uniformly  $^{13}\text{C}$ -labeled Ras(wt)•GDP (see Figure 4.6). According to NMR data, Ras(wt)•GppNHp in complex with Raf-RBD occurs in liquid solution only in one conformational state [3] (see Section 4.1) and was therefore used as a reference for the contribution of two directly ligated amino acids, i.e. Ser17 and Thr35. While the ENDOR spectrum of the G12V mutant is undistinguishable from the one of the wild-type protein, the spectrum from the Ras(wt)•GppNHp•Raf-RBD

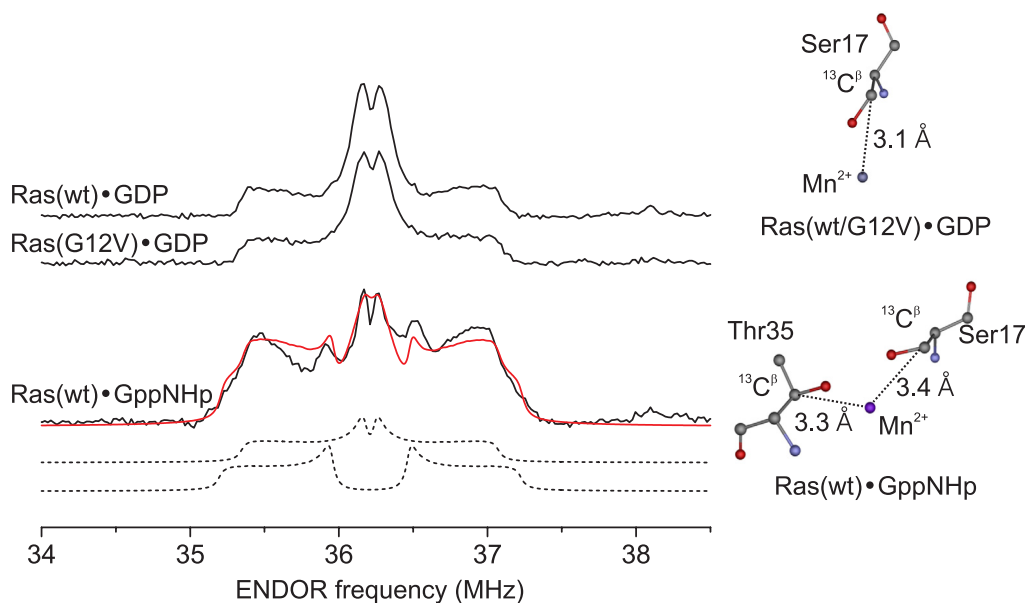


**Figure 4.6** Comparison of  $^{13}\text{C}$ -Mims ENDOR spectra of uniformly  $^{13}\text{C}$ -labeled wild-type Ras•Mn<sup>2+</sup>•GDP and its oncogenic mutant G12V as well as of Ras(wt)•Raf•GppNHp at 4.5 K. Superimposed on the latter is the simulation with the hyperfine tensor components  $|A_{\perp 1}| = 0.07$  MHz,  $|A_{\parallel 1}| = 1.72$  MHz and  $|A_{\perp 2}| = 0.52$  MHz,  $|A_{\parallel 2}| = 2.02$  MHz as described in the text and listed in Table 4.2. Right: Schematic representation of the binding of the metal ion according to the X-ray structures [5, 83]. Experimental parameters: Ras(wt)•GDP:  $t_{\pi/2} = 96$  ns,  $\tau = 250$  ns,  $t_{\text{RF}} = 18$   $\mu\text{s}$ , shot repetition time = 5 ms, 240 scans with 50 shots per point; Ras(G12V)•GDP: as Ras(wt)•GDP but with  $t_{\pi/2} = 42$  ns. Ras•Mn<sup>2+</sup>•Raf•GppNHp: as Ras(wt)•GDP but with  $t_{\pi/2} = 104$  ns,  $t_{\text{RF}} = 35$   $\mu\text{s}$ .

complex displays significant differences. Specifically, the latter contains features similar to the spectra from the GDP-bound complexes plus some additional contribution. Based on all known X-ray structures this contribution is expected to arise from Thr35 which is directly coordinated to the metal ion.

As a starting point for the spectral simulation procedure we used the hyperfine tensor components obtained from DFT calculations (see Appendix A) as listed in Table 4.2. As a result, the spectrum of the GppNHp complex was simulated with a superposition of two hyperfine coupling tensors with  $|A_{\perp 1}| = 0.07$  MHz,  $|A_{\parallel 1}| = 1.72$  MHz and  $|A_{\perp 2}| = 0.52$  MHz,  $|A_{\parallel 2}| = 2.02$  MHz and a matrix peak about 0.6 MHz wide, as displayed in Figure 4.3.2. The calculated point-dipole distances from the  $T_{\perp}$  components of the extracted  $^{13}\text{C}$  dipolar tensors are 3.4 Å and 3.3 Å. The smaller tensor is tentatively assigned to Thr35 and the slightly larger one to Ser17 based on the X-ray structure of GppNHp and the calculated

hyperfine tensor components (see Table 4.2), being aware that the very small differences between the  $\text{Mn}^{2+}$ -Thr35 and  $\text{Mn}^{2+}$ -Ser17 distances observed in the X-ray structures might not be conserved in the frozen solution state. The comparison between the spectra of GppNHp and the GDP complexes strongly suggests that the spectra of the wild-type and oncogenic GDP-bound protein are both constituted by only one amino acid ligand, i.e. Ser17.

To confirm this result, the relative  $^{13}\text{C}$ -ENDOR intensities of the spectra from the three complexes acquired under the same experimental conditions were compared by normalizing them to the respective echo intensity. Since the ENDOR effect for small hyperfine couplings is directly proportional to the number of contributing nuclei, the ENDOR effect measured at the same spectral position, on the edge of the powder pattern in Figure 4.6, should differ by about a factor of two between the GDP and the GppNHp complexes. For three different loadings of the sample a reproducible ENDOR effect of 0.28(3) was measured for both Ras•GDP complexes and of 0.5(1) for the Ras(wt)•GppNHp•Raf complex. The observation strongly supports the above mentioned result that in the GDP complexes only one amino acid, namely Ser17, is directly coordinated to the metal ion.

## 4.4 Summary and Discussion

In the present study, high-frequency 94 GHz ENDOR spectroscopy combined with selective isotope labeling was employed for studying the ligation sphere of the metal ion in wild-type Ras•GDP and the oncogenic GDP-bound mutant G12V as well as in the Ras(wt)•GppNHp complex. While the structure at the active site has been studied by several groups using EPR spectroscopy [1, 46, 66–69], the present work aimed at searching for the ligand that would replace a water ligand in the wild-type GDP-bound protein compared to the oncogenic mutant G12V as proposed by Rohrer et al. [1]. In particular,  $^{13}\text{C}$ - and  $^{31}\text{P}$ -ENDOR was used to test whether an amino acid from the protein environment or a non-covalently bound phosphate ion would be the substituting candidate. The measurements were carried out in the frozen solution state at very low temperatures (3–4.5 K). From the anisotropic part of the simulated hyperfine coupling tensors, the point-dipole distances between the metal ion and the surrounding  $^{13}\text{C}$  and  $^{31}\text{P}$  nuclei were extracted and compared with the distances reported in the literature. In the

following, the main results will be summarized and discussed with special focus on differences between the liquid and the frozen solution state.

From the difference  $^{31}\text{P}$ -ENDOR spectra of the Ras(wt)•GppNHp and Ras(wt)-GDP complex recorded by Bennati et al. [80] a distance of 3.4(1) Å between the metal ion and the  $\beta$ - as well as the  $\gamma$ -phosphorus was extracted. The isotropic part of the hyperfine coupling tensor is slightly different for both phosphorus nuclei, indicating different electronic environments around these nuclei. Furthermore, according to our data, the  $\beta$ -phosphorus is equally far from the metal ion in the GDP- and in the GppNHp-bound state. For both states, the point-dipole distances are in agreement with the distances observed in crystal structures [4, 34] as well as in ESEEM studies [67]. Analysis of the  $^{31}\text{P}$ -ENDOR spectra from Ras(G12V)•GDP as well as from Ras(wt)•GDP showed no difference between the resonances observed for the wild-type protein and the oncogenic mutant [80]. Since the Ras(wt)•GPD and Ras(wt)•GppNHp spectra are clearly different, the presence of an additional, bound phosphate ion in the Ras(wt)•GDP and not in the G12V complex can be ruled out.

In order to test whether Asp57 is a direct ligand of the metal center in Ras(wt)•GDP as was proposed by Schlichting et al. [31], we compared the resonances observed in the  $^{13}\text{C}$ -ENDOR spectra of uniformly  $^{13}\text{C}$ -labeled Ras(wt)-GDP with the ones observed in the spectra of the same complex containing selectively labeled 1,4- $^{13}\text{C}$  aspartates. The spectra from the uniformly labeled protein were simulated with one hyperfine coupling tensor whose anisotropic part yields a point-dipole distance to the metal ion of 3.1 Å in close agreement to the  $\text{Mg}^{2+}$ - $^{13}\text{C}^{\beta}$ -Ser17 distances observed in crystal structures [5, 24, 37]. It should be mentioned that hyperfine coupling values of Ser17 had not been reported in any of the previous ESEEM studies, although an interaction had been detected [68]. In the  $^{13}\text{C}$ -ENDOR spectra of the selectively labeled samples only a small splitting showed up which translates into a point-dipole distance of 4.8(1) Å. The observed distance rules out direct coordination to the metal ion and is in agreement with the  $\text{Mg}^{2+}$ - $^{13}\text{C}^{\gamma}$ -Asp57 distance observed in the crystal structures [5, 24, 37] as well as with previous ESEEM studies of the mutant Ras(G12V,A59T)•GDP complex [46, 69].

Furthermore, the question of an additional amino acid ligand bound to the metal ion in the wild-type protein with respect to the oncogenic mutant G12V was addressed by comparing the ENDOR spectra of uniformly  $^{13}\text{C}$ -labeled Ras(wt)-GDP with spectra from Ras(G12V)•GDP as well as from Ras(wt)•Raf•GppNHp.

As was observed in previous  $^{31}\text{P}$ - and  $^{17}\text{O}$ -ENDOR studies [80], no difference between the spectra from the wild-type protein and the oncogenic mutant could be detected. In contrast, the spectra from the Ras(wt)•GppNHp showed significant differences. The simulation of the latter yielded two  $^{13}\text{C}$  nuclei of two directly bound amino acid ligands with distances of 3.4(1) and 3.3(1) Å which were assigned to the  $^{13}\text{C}^\beta$  of Ser17 and Thr35, based on the knowledge of the crystal structure as well as on DFT calculations. Previous ESEEM data had reported a much weaker coupling to Thr35 yielding a distance of 4.3(2) Å without complexation with the effector Raf-kinase [68]. The authors discuss possible reasons for the discrepancy between the crystal and the frozen solution structure, concluding that either Thr35 is in a more remote, well defined conformation, or the effector region exhibits conformational heterogeneity as suggested by  $^{31}\text{P}$ -NMR [2, 50] and MD simulations [51, 52]. This question could be answered performing  $^{13}\text{C}$ -ENDOR on the mutant Ras(T35S)•GppNHp (see Section 4.5). The observations from the  $^{13}\text{C}$ -ENDOR data described here exclude the presence of an additional amino acid ligand other than Ser17 in the wild-type GDP-bound protein with respect to its oncogenic mutant in frozen solution.

Overall, the observed structural data are in agreement with the published crystal structures [4, 5, 24, 34, 37, 38] and imply equal coordination spheres in the GDP-bound wild-type protein and G12V mutant, such that the ligation of an additional amino acid ligand or phosphate ion to the metal ion in Ras(wt)•GDP can be ruled out.

Furthermore, the reported ENDOR data provide an answer to the question whether the two conformational states observed by NMR for the wild-type protein in liquid solution are connected with a different ligation sphere of the metal ion as suggested by Rohrer et al. [1]. Since more than one conformational state was also found by NMR in crystals of the GppNHp-bound wild-type Ras protein [50, 77], it appears likely that two conformational states also exist in the GDP-bound wild-type protein in frozen solution. In order to estimate whether a second conformational state connected with a different ligation sphere of the metal ion could be observed in the ENDOR spectra, the ENDOR data were correlated with the  $^{31}\text{P}$ -NMR data using fractional states to account for different populations of conformers. Although these numbers likely vary with the temperature and also with the different metal ion, it was estimated that one should be able to observe a second conformer with a population as low as 1/3 (corresponding to the equilibrium constant  $K_{12} = 0.3$  reported for the wild-type GDP-bound protein [1])

if the hyperfine coupling values between the two conformers would differ at least by 15–20%. This estimate was based on the spectral resolution demonstrated by the comparison with the GppNHp spectra and given the signal-to-noise ratio of the spectra in the GDP-complexes. This estimation yields that a second conformation if connected with a different ligation sphere at the active site should be observable in the ENDOR spectra. Therefore, in conclusion our data indicate that the two conformational states observed in the wild-type GDP-bound protein in solution are not connected with a different ligation sphere of the metal ion.

## 4.5 Outlook

Still, the question about the nature of the ligand replacing a water molecule in the solution state of Ras(wt)•GDP remains open. A chloride ion from the buffer could bind to the metal center in the wild-type GDP-bound protein. This question might be answered performing chlorine ENDOR. Beforehand one could test whether the same coordination sphere of the metal ion observed in liquid solution is preserved in the frozen state, which could be clarified by simulating the CW EPR spectra obtained at low temperatures [1], including the  $^{17}\text{O}$  hyperfine couplings obtained from previous ENDOR studies [80].

Although two states were observed in the crystals of Ras(wt)•GppNHp, it cannot be excluded that in frozen solution, the equilibrium of the two conformational states is shifted towards a single conformation. This question could be addressed with ENDOR studies of the GppNHp-bound protein, by comparing the frozen solution  $^{13}\text{C}$ -ENDOR spectra of Ras(wt)•GppNHp with the spectra from Ras(wt)•GppNHp•Raf. As described in Section 4.1, the former exhibits two states with equal populations in solution which is shifted entirely towards state 2 upon complexation with Raf.

Furthermore, ENDOR spectroscopy could be used to test whether state 1 observed in the GppNHp complex is indeed connected with a loss of binding of Thr35 to the metal center as well as to the  $\gamma$ -phosphate group as suggested by Spörner et al. [3] and confirmed by Ye et al. with  $^{31}\text{P}$ -NMR and crystallographic studies of M-Ras [78]. The mutant Ras(T35S)•GppNHp was found by  $^{31}\text{P}$ -NMR only in state 1 and in the Ras•Raf complex only in state 2. Therefore, the comparison of  $^{13}\text{C}$ -ENDOR spectra of Ras(T35S)•GppNHp with spectra from the same complex bound to the effector should answer whether Thr35 is no

longer bound to the metal center in state 1.

## References

- [1] Rohrer, M.; Prisner, T.; Brüggmann, O.; Käss, H.; Spörner, M.; Wittinghofer, A.; Kalbitzer, H. R. *Biochemistry* **2001**, *40*, 1884–1889.
- [2] Geyer, M.; Schweins, T.; Herrmann, C.; Prisner, T. F.; Wittinghofer, A.; Kalbitzer, H. R. *Biochemistry* **1996**, *35*, 10308–10320.
- [3] Spoerner, M.; Herrmann, C.; Vetter, I. R.; Kalbitzer, H.-R.; Wittinghofer, A. *Proc. Natl. Acad. Sci. USA* **2001**, *98*, 4944–4949.
- [4] Pai, E. F.; Krenzel, U.; Goody, R. S.; Kabsch, W.; Wittinghofer, A. *EMBO J.* **1990**, *9*, 2351–2359.
- [5] Tong, L.; deVos, A. M.; Milburn, M. V.; Brunger, A.; Kim, S.-H. *J. Mol. Biol.* **1991**, *217*, 503–516.
- [6] Krenzel, U.; Schlichting, I.; Scherer, A.; Schumann, R.; Frech, M.; John, J.; Kabsch, W.; Pai, E. F.; Wittinghofer, A. *Cell* **1990**, *62*, 539–548.
- [7] Wittinghofer, A.; Herrmann, C. *FEBS Lett.* **1995**, *369*, 52–56.
- [8] Maegley, K. A.; Admiraal, S. J.; Herschlag, D. *Proc. Natl. Acad. Sci. USA* **1996**, *93*, 8160–8166.
- [9] Wittinghofer, A.; Nassar, N. *TIBS* **1996**, *21*, 488–491.
- [10] Wittinghofer, A.; Scheffzek, K.; Ahmadian, M. R. *FEBS Lett.* **1997**, *410*, 63–67.
- [11] Wittinghofer, A. *Nature* **1998**, *394*, 317–320.
- [12] Sprang, S. *Curr. Opin. in Struct. Biol.* **1997**, *7*, 849–856.
- [13] Sprang, S. R. *Annu. Rev. Biochem.* **1997**, *66*, 639–678.
- [14] Geyer, M.; Wittinghofer, A. *Curr. Opin. Struct. Biol.* **1997**, *7*, 786–792.
- [15] Vetter, I. R.; Wittinghofer, A. *Science* **2001**, *294*, 1299–1304.

- [16] Takai, Y.; Sasaki, T.; Matozaki, T. *Physiol. Rev.* **2001**, *81*, 153–208.
- [17] Ehrhardt, A.; Ehrhardt, G. R. A.; Guo, X.; Schrader, J. W. *Experimental Hematology* **2002**, *30*, 1089–1106.
- [18] Scheffzek, K.; Ahmadian, M. R. *Cell. Mol. Life Sci.* **2005**, *62*, 3014–3038.
- [19] Bourne, H. R.; Sanders, D. A.; McCormick, F. *Nature* **1990**, *348*, 125–132.
- [20] Cherfils, J.; Chardin, P. *Trends. Biochem. Sci.* **1999**, *24*, 306–311.
- [21] Boguski, M. S.; McCormick, F. *Nature* **1993**, *366*, 643–654.
- [22] Scheffzek, K.; Ahmadian, M. R.; Wittinghofer, A. *Trends Biochem. Sci.* **1998**, *23*, 257–262.
- [23] Bernardis, A. *Biochim. Biophys. Acta* **2003**, *1603*, 47–82.
- [24] Milburn, M. V.; Tong, L.; de Vos, A. M.; Brünger, A.; Yamaizumi, Z.; Nishimura, S.; Kim, S.-H. *Science* **1990**, *247*, 939–945.
- [25] Brünger, A. T.; Milburn, M. V.; Tong, L.; de Vos, A. M.; Jancarik, J.; Yamaizumi, Z.; Nishimura, S.; Ohtsuka, E.; Kim, S. H. *Proc. Natl. Acad. Sci. USA* **1990**, *87*, 4849–4853.
- [26] Bos, J. L. *Cancer Res.* **1989**, *49*, 4682–4689.
- [27] Barbacid, M. *Annu. Rev. Biochem.* **1987**, *56*, 779–827.
- [28] Der, D.; Finkel, T.; Cooper, G. M. *Cell* **1986**, *44*, 167–176.
- [29] Neri, A.; Knowles, D. M.; Greco, A.; McCormick, F.; Dalla-Favera, R. *Proc. Natl. Acad. Sci. USA* **1988**, *85*, 9268–9272.
- [30] Seeburg, P. H.; Colby, W. W.; Capon, D. J.; Goeddel, D. V.; Levinson, A. D. *Nature* **1984**, *312*, 71–75.
- [31] Schlichting, I.; Almo, S. C.; Rapp, G.; Wilson, K.; Petratos, K.; Lentfer, A.; Wittinghofer, A.; Kabsch, W.; Pai, E. F.; Petsko, G.; Goody, R. S. *Nature* **1990**, *345*, 309–315.
- [32] Prive, G. G.; Milburn, M. V.; Tong, L.; de Vos, A. M.; Yamaizumi, Z.; Nishimura, S.; Kim, S.-H. *Proc. Natl. Acad. Sci. USA* **1992**, *89*, 3649–3653.



- [33] De Vos, A. M.; Tong, L.; Milburn, M.; Matias, P. M.; Jancarik, J.; Noguchi, S.; Nishimura, K.; Miura, K.; Ohtsuka, E.; Kim, S. J. *Science* **1988**, *239*, 888–893.
- [34] Wittinghofer, F.; Kregel, U.; John, J.; Kabsch, W.; Pai, E. F. *Environ. Health Perspect.* **1991**, *93*, 11–15.
- [35] Franken, S. M.; Scheidig, A. J.; Kregel, U.; Rensland, H.; Lautwein, A.; Geyer, M.; Scheffzek, K.; Goody, R. S.; Kalbitzer, H.; Pai, E.; Wittinghofer, A. *Biochemistry* **1993**, *32*, 8411–8420.
- [36] Scheidig, A. J.; Sanchez-Lorente, A.; Lautwein, A.; Pai, E. F.; Corrie, J. E. T.; Reid, G. P.; Wittinghofer, A.; Goody, R. S. *Acta. Cryst.* **1994**, *D50*, 512–520.
- [37] Hall, B. E.; Bar-Sagi, D.; Nassar, N. *Proc. Natl. Acad. Sci. USA* **2002**, *99*, 12138–12142.
- [38] Nassar, N.; Horn, G.; Herrmann, C.; Block, C.; Janknecht, R.; Wittinghofer, A. *Nat. Struct. Biol.* **1996**, *3*, 723–729.
- [39] Huang, L.; Hofer, F.; Martin, G. S.; Kim, S. H. *Nat. Struct. Biol.* **1998**, *5*, 422–426.
- [40] Vetter, I. R.; Linnemann, T.; Wohlgemuth, S.; Geyer, M.; Kalbitzer, H.-R.; Herrmann, C.; Wittinghofer, A. *FEBS Lett.* **1999**, *451*, 175–180.
- [41] Pacold, M. E.; Suire, S.; Perisic, O.; Lara-Gonzalez, S.; Davis, C. T.; Walker, E. H.; Hawkins, P. T.; Stephens, L.; Eccleston, J. F.; Williams, R. L. *Cell* **2000**, *103*, 931–943.
- [42] Scheffzek, K.; Grünewald, P.; Wohlgemuth, S.; Kabsch, W.; Tu, H.; Wigler, M.; Wittinghofer, A. *Structure* **2001**, *9*, 1043–1050.
- [43] Pai, E. F.; Kabsch, W.; Kregel, U.; Holmes, K.; John, J.; Wittinghofer, A. *Nature* **1989**, *341*, 209–214.
- [44] Wei, Y.; Zhang, Y.; Derewenda, U.; Liu, X.; Minor, W.; Nakamoto, R. K.; Somlyo, A. *Nat. Struct. Biol.* **1997**, *4*, 699–703.

- [45] Rohrer, M.; Brüggmann, O.; Kinzer, B.; Prisner, T. F. *Appl. Magn. Res.* **2001**, *21*, 257–274.
- [46] Halkides, C.; Farrar, C. T.; Larsen, R. G.; Redfield, A. G.; Singel, D. J. *Biochemistry* **1994**, *33*, 4019–4035.
- [47] Haller, M.; Hoffmann, U.; Schanding, T.; Goody, R. S.; Vogel, P. D. *J. Biol. Chem.* **1997**, *48*, 30103–30107.
- [48] Farrar, C. T.; Halkides, C. J.; Singel, D. J. *Structure* **1997**, *5*, 1055–1066.
- [49] Ito, Y.; Yamasaki, K.; Iwahara, J.; Tereda, T.; Kamiya, A.; Shirouzu, M.; Muto, Y.; Kawai, G.; Yokoyama, S.; Laue, E. D.; Wälchi, M.; Shibata, T.; Nishimura, S.; Miyazawa, T. *Biochemistry* **1997**, *36*, 9109–9119.
- [50] Iuga, A.; Spoerner, M.; Kalbitzer, H. R. *J. Mol. Biol.* **2004**, *342*, 1033–1040.
- [51] Foley, C. K.; Pederson, L. G.; Charifson, P. S.; Darden, T. A.; Wittinghofer, A.; Pai, E. F.; Anderson, M. W. *Biochem.* **1992**, *31*, 4951–4959.
- [52] Díaz, J. F.; Wroblowski, B.; Engelborghs, Y. *Biochemistry* **1995**, *34*, 12038–12047.
- [53] Ma, J.; Karplus, M. *Proc. Natl. Acad. Sci. USA* **1997**, *94*, 11905–11910.
- [54] Mello, L. V.; van Aalten, D. M. F.; Findlay, J. B. C. *Prot. Engen.* **1997**, *10* (4), 381–387.
- [55] Glennon, T. M.; Villa, J.; Warshel, A. *Biochemistry* **2000**, *39*, 9641–9651.
- [56] Futatsugi, N.; Tsuda, M. *Biophys. J.* **2001**, *81*, 3483.
- [57] Shurki, A.; Warshel, A. *Proteins* **2004**, *55*, 1–10.
- [58] Gohlke, J.; Kuhn, L. A.; Case, D. A. *Proteins* **2004**, *56*, 322–337.
- [59] Cepus, V.; Scheidig, A. J.; Goody, R. S.; Gerwert, K. *Biochemistry* **1998**, *37*, 10236–10271.
- [60] Wang, J. H.; Xiao, D. G.; Deng, H.; Webb, M. R.; Callender, R. *Biochemistry* **1998**, *37*, 11106–11116.
- [61] Du, X.; Frei, H.; Kim, S.-H. *J. Biol. Chem.* **2000**, *275*, 8492–8500.

- [62] Cheng, H.; Sukal, S.; Deng, H.; Leyh, T. S.; Callender, R. *Biochemistry* **2001**, *40*, 4035–4043.
- [63] Allin, C.; Ahmadian, M. R.; Wittinghofer, A.; Gerwert, K. *Proc. Natl. Acad. Sci. USA* **2001**, *98*, 7754–7759.
- [64] Feuerstein, J.; Kalbitzer, H. R.; John, J.; Goody, R. S.; Wittinghofer, A. *Eur. J. Biochem.* **1987**, *162*, 49–55.
- [65] Smithers, G. W.; Poe, M.; Latwesen, D. G.; Reed, G. H. *Arch. Biochem. Biophys.* **1990**, *280*, 416–420.
- [66] Latwesen, D. G.; Poe, M.; Leigh, J. S.; Reed, G. H. *Biochemistry* **1992**, *31*, 4946–4950.
- [67] Larsen, R. G.; Halkides, C. J.; Redfield, A. G.; Singel, D. J. *J. Am. Chem. Soc.* **1992**, *114*, 9608–9611.
- [68] Halkides, C. J.; Farrar, C. T.; Redfield, A. G.; Singel, D. J. In *Biological Structure and Dynamics*, Vol. 1; Sarma, R. H.; Sarma, M. H., Eds.; Adenine Press: 1995.
- [69] Bellew, B.; Halkides, C. J.; Gerfen, G. J.; Griffin, R. G.; Singel, D. J. *Biochemistry* **1996**, *35*, 12186–12193.
- [70] Schweins, T.; Scheffzek, K.; Afshauer, R.; Wittinghofer, A. *J. Mol. Biol.* **1997**, *266*, 847–856.
- [71] Reed, G. H.; Markham, G. D. *Biol. Magn. Res.* **1984**, *6*, 73–142.
- [72] Muto, Y.; Yamasaki, K.; Ito, Y.; Yajima, S.; Masaki, H.; Uozumi, T.; Wälchli, M.; Nishimura, S.; Miyazawa, T.; Yokoyama, S. *J. Biol. NMR* **1993**, *3*, 165–184.
- [73] Kraulis, P. J.; Domaille, P. J.; Campbell-Burk, S. L.; Van Aken, T.; Laue, E. D. *Biochemistry* **1994**, *33*, 3515–3531.
- [74] Hu, J. S.; Redfield, A. G. *Biochemistry* **1997**, *36*, 5045–5052.
- [75] Spoerner, M.; Wittinghofer, A.; Kalbitzer, H.-R. *FEBS Lett.* **2004**, *578*, 305–310.

- [76] Spoerner, M.; Nuehs, A.; Ganser, P.; Herrmann, C.; Wittinghofer, A.; Kalbitzer, H.-R. *Biochemistry* **2005**, *44*, 2225–2236.
- [77] Stumber, M.; Geyer, M.; Kalbitzer, H. R.; Scheffzek, K.; Haeblerlen, U. *J. Mol. Biol.* **2002**, *323*, 899–907.
- [78] Ye, M.; Shima, F.; Muraoka, S.; Liao, J.; Okamoto, H.; Yamamoto, M.; Tamura, A.; Yagi, N.; Ueki, T.; Kataoka, T. *J. Biol. Chem.* **2005**, *280*, 31267–31275.
- [79] Ford, B.; Skowronek, K.; Boykevisch, S.; Bar-Sagi, D.; Nassar, N. *J. Biol. Chem.* **2005**, *280*, 25697–25705.
- [80] Bennati, M.; Hertel, M. M.; Fritscher, J.; Prisner, T. P.; Weiden, N.; Dinse, K. P.; Spörner, M.; Hofweber, R.; Horn, G.; Kalbitzer, H.-R. *Biochemistry* **2005**, *45*, 42–50.
- [81] Bennati, M.; Farrar, C. T.; Bryant, J. A.; Inati, S. J.; Weis, V.; Gerfen, G. J.; Riggs-Gelasco, P.; Stubbe, J.; Griffin, R. G. *J. Magn. Res.* **1999**, *138*, 232–243.
- [82] Carmieli, R.; Manikandan, P.; Kalb, A. J.; Goldfarb, D. *J. Am. Chem. Soc.* **2001**, *123*, 8378–8386.
- [83] Wittinghofer, A.; Kabsch, W.; Pai, E. F.; Petsko, G.; Goody, R. S. *Nature* **1990**, *345*, 309–315.

# Chapter 5

## Implementing ENDOR at 180 GHz

### 5.1 Introduction

It is well established that electron nuclear double resonance (ENDOR) spectroscopy shows considerable advantages when performed at high fields and frequencies [1–5]. One of the numerous advantages is the increased nuclear Zeeman resolution, which leads to the separation of ENDOR signals from different nuclei as well as significant simplification of the ENDOR spectra due to the reduction of second-order effects (see Chapter 2). Another advantage is the possibility to determine the absolute signs of hyperfine coupling constants (HFCs) by exploiting the large thermal electron spin polarization at high fields and low temperatures [6, 7]. Furthermore, the increased resolution of  $g$ -anisotropy at high fields allows the selective excitation of specific molecular orientations. For high-spin systems such as  $\text{Mn}^{2+}$  [8], high-field EPR offers the crucial advantage to reduce the forbidden transitions and narrow the central transitions ( $m_S = -\frac{1}{2} \leftrightarrow +\frac{1}{2}$ ). In particular the latter advantage renders high-field ENDOR a powerful technique for studying the ligation sphere of  $\text{Mn}^{2+}$  in general and in  $\text{Ras}\cdot\text{Mn}^{2+}\cdot\text{GXP}$  and provided one motivation for implementing an ENDOR setup into a home-built pulsed EPR spectrometer operating at 180 GHz [9, 10].

Despite the above mentioned advantages, so far only few home-built pulsed high-field ENDOR spectrometers have been built, of which the first operating at 95 GHz (W-band) were built in 1995 simultaneously in Berlin [1, 11] and in Leiden [2]. In 1999, another pulsed W-band ENDOR spectrometer was implemented in Rehovot [3] and at the same time at a frequency of 140 GHz in Cambridge [5]. Very recently, pulsed ENDOR has been demonstrated at a frequency as

high as 275 GHz in Leiden [12]. Furthermore, a W-band ENDOR probe can be purchased commercially via Bruker Analytik [13] as well as from Donetsk Physico Technical Institute [3]. The reason for so little home-built ENDOR spectrometers might be found in the challenge of building a reliable high-sensitivity ENDOR setup due to the additional requirements that have to be met in comparison to high-field EPR and NMR (Nuclear Magnetic Resonance) spectrometers. The additional requisites originate from the requirement of a high microwave as well as a high radio frequency (RF) field strength ( $\mathbf{B}_1$  and  $\mathbf{B}_2$ , respectively) at the sample position necessary for observing the change of the electron spin echo intensity while applying the RF field. Furthermore, in the ENDOR experiment, the bandwidths which need to be covered with the resonant circuit are often much broader than the chemical shifts detected with NMR (several MHz versus several hundred kHz). These demands make the NMR probe a very critical part in successful ENDOR instrumentation. Additionally, the small sample and resonator dimensions at high frequencies render the sample handling demanding and require external mounting of the coil.

Most efficient power transfer from the high-power, pulsed radio frequency amplifier to the probe is obtained when the NMR probes are "tuned" and "matched" [14]. An efficient power transfer will minimize the RF pulse length, which is especially important for ENDOR, where an intense electron spin echo is crucial for optimum ENDOR performance. In the past, impedance-matching networks for ENDOR experiments have been realised using  $RL$  [2, 12, 13, 15–19] or  $RLC$  circuits with fixed [3, 16, 18, 20] or variable [17, 21, 22] capacitors. In a series  $RLC$  circuit no reflections arise at the resonant frequency, provided that  $R$  is equal to the impedance of the transmission line. However, at frequencies different from the resonant frequency, the impedance is no longer  $50 \Omega$  such that reflections arise. A solution to the problem is a frequency-independent impedance matching achieved via variable and fixed capacitors yielding a tuned circuit with high current over a broad frequency range [16, 23–26]. However, appropriate adjustment of the series capacitance is difficult to achieve even for a limited frequency range and becomes more demanding at high frequencies. Therefore, less complicated RF schemes have been designed at high frequencies. For their ENDOR setup operating at 95 GHz, Rohrer et al. designed an RF scheme where tuning and matching was achieved via a series  $RLC$  circuit, in which a second resonance frequency was obtained via a second fixed capacitor, acting as  $\pi$ -filter [1]. At 140 GHz, a parallel  $RLC$  circuit with variable tuning and matching capacitors

was designed by Bennati and coworkers in particular for the high frequency range [5]. A broadband  $RLC$  circuit with characteristics of low-pass filters proved also to permit highly efficient RF irradiation [2, 3, 27] in particular for nuclei with small gyromagnetic ratio [2, 27].

However, the construction of a tuning system becomes more demanding at even higher frequencies since the reduced resonator and sample dimensions ask for a coil geometry which implies a limited range of inductivities. Furthermore, a tuned circuit conflicts with the necessity of sweeping the RF frequency while recording the ENDOR spectra such that one often prefers to use a broadband probe circuit to meet the frequency sweep requirements [2, 12, 13, 16–19].

In the most simple broadband circuit, the ENDOR RF amplifier is connected directly to the coil. Because of its simplicity and since it provides a large bandwidth, this arrangement was chosen in the present work for designing an  $RL$  circuit for performing  $^1\text{H}$ -ENDOR experiments at 180 GHz, which was incorporated into a home-built 180 GHz pulsed EPR spectrometer [9, 10]. The performance for  $^1\text{H}$ -ENDOR is illustrated on the model system bisdiphenylene-phenyl-allyl (BDPA) using the Mims as well as the Davies pulse sequences. Furthermore, Mims and Davies ENDOR spectra of  $\text{Ras}\cdot\text{Mn}^{2+}\cdot\text{GDP}$  are described and the observed  $^1\text{H}$  HFCs compared with the ones reported in the literature for biological systems containing  $\text{Mn}^{2+}$ .

## 5.2 ENDOR Probe and Radio Frequency Circuit

In order to achieve an optimum ENDOR performance, an effective power transmission to the RF coil as well as a stable and intense EPR signal are of crucial importance. Therefore, the goal in designing the broadbanded RF circuit used in the present ENDOR setup was to maximize the current in the coil while minimizing the voltage standing wave ratio (VSWR) in the lines by finding the optimum coil dimensions. Furthermore, the  $\text{TE}_{011}$  resonator designed by Rohrer et al. [10] needed to be modified for performing ENDOR experiments, such that a compromise between RF penetration and the quality factor ( $Q$ ) of cavity had to be made. Amongst other factors, the echo intensity strongly depends on  $Q$ .

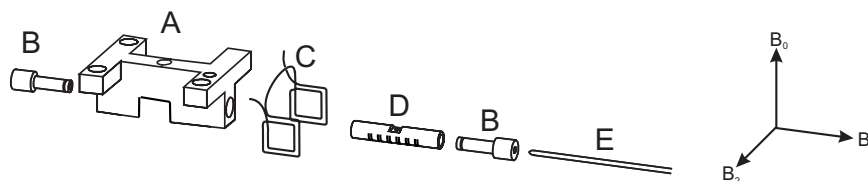


**Figure 5.1** Schematic drawing of the 180 GHz ENDOR cavity holder (A) with plungers (B), four-turn flat RF coil made out of copper wire (C), silver-plated, cylindrical TE<sub>011</sub> cavity (D) and sample tube (E).

### 5.2.1 Design of the Resonator

For externally produced RF fields, the main problem in modifying the TE<sub>011</sub> cavity for ENDOR experiments is the shielding of the metal which prevents penetration of the used NMR frequencies into the originally closed cavity. This shielding is due to the *skin effect* which is observed when an alternating voltage passes through a leading metal surface, yielding a current density at the center of the metal which is smaller than at the surface. The *skin depth*  $\delta = 1/\sqrt{\mu_0\sigma\pi\nu}$  gives the depth at which the current density has dropped to  $1/e$ , depending on the frequency  $\nu$  of the alternating voltage and the conductivity of the metal surface  $\sigma$  ( $\mu_0$  is the permeability of vacuum). Since the *skin depth* is inversely proportional to the frequency, the applied radio frequencies (e.g. 275 MHz for <sup>1</sup>H) will penetrate more easily through the resonator surface than the applied microwaves (180 GHz).

In order to reduce ring current effects (*Eddy currents*) which prevent RF penetration, the resonator wall was divided in segments of well chosen size and distance as depicted in Figure 5.2 such that *Eddy currents* and losses of microwave power through the slotted cavity were minimized. To estimate the size of the loss of microwave power, we performed preliminary measurements of the quality factor  $Q$  of resonators with different slot dimensions (see Figure 5.2).  $Q$  was determined experimentally by sweeping the MW frequency with a varactor and observing the frequency response of the reflected power on the oscilloscope. The quality factor of the cavity was then calculated via  $Q = \frac{\Delta\nu}{\nu_0}$ , where  $\Delta\nu$  is the width of the resonant dip at half height and  $\nu_0$  the resonance frequency. For the tested resonators with  $d = 0.10$  mm and  $a = 0.70$  mm (cavity A),  $d = 0.22$  mm and  $a = 0.70$  mm (cavity B),  $d = 0.30$  mm and  $a = 0.75$  mm (cavity C) as well as  $d = 0.45$  mm and  $a = 0.38$  mm (cavity D), cavity A and B both yielded quality



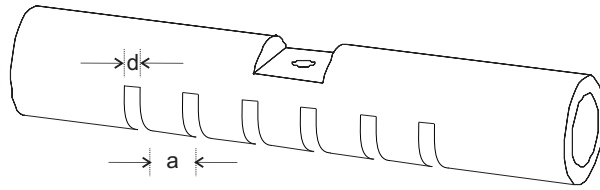


**Figure 5.2** Schematic drawing of the modified  $TE_{011}$  EPR cavity with six introduced slots with width  $d$  and distance  $a$  as described in the text.

factors of  $Q_{\text{empty}} = 2500 \pm 300$  while cavity  $C$  yielded  $Q_{\text{empty}} = 2000 \pm 300$  and the quality factor of cavity  $D$  was impossible to determine because the resonator dip was no longer visible within the mode picture. Although the quality factor for cavity  $C$  was lower than for cavity  $A$  and  $B$ , the largest ENDOR effect was observed when performing ENDOR experiments using cavity  $C$ .

Furthermore, in order to minimize or ideally prevent shielding it is common to cover the metal surface with a thin layer of material with very high electric conductivity. Therefore, in the present work, the cavity made from brass was covered with a thin silver layer of  $10 \mu\text{m}$ .

### 5.2.2 The Radio Frequency Field

In order to design an ENDOR system with maximum current in the coil and minimum reflections in the transmission line, one has to consider that both, the current and the reflections, strongly depend on the frequency-dependent inductance of the coil. In an unmatched circuit as used in the present work, reflections occur over the entire frequency range - apart from a single frequency where the coil impedance is equal to  $50 \Omega$ . Therefore, the coil dimensions had to be chosen such that the current in the coil is maximised (and hence  $\mathbf{B}_2$ ) while the VSWR in the lines is minimized (and therefore maximum power is reaching the coil), as described in the following.

The current at the coil is given by [28]:

$$I = \sqrt{\frac{2 \cdot P}{Z_L}} \approx \sqrt{\frac{2 \cdot P}{\omega L}}, \quad (5.1)$$

where  $P$  is the power fed into the RF circuit and  $Z_L$  is the coil impedance with  $Z_L = R + i(\omega L - \omega C)$  and  $|Z_L| = Z$ ,  $R$  being the real resistance,  $(\omega L - \omega C)$

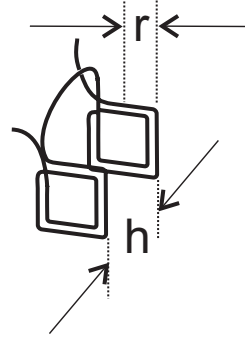


**Figure 5.3** Schematic drawing of the flat saddle coil with radius  $r = 3$  mm and height  $h = 5.8$  mm as used in the present ENDOR setup.

the reactance,  $L$  the inductance,  $C$  the capacity, and  $\omega$  the RF frequency. The approximation in Equation 5.1 holds when the real and capacitive parts of the coil reactance are negligible. The reflections in the transmission line system are given by the *reflection coefficient* [28]

$$r = \frac{Z - Z_T}{Z + Z_T}, \quad (5.2)$$

where  $Z$  denotes the total impedance of the RF circuit and  $Z_T$  is the impedance of the transmission line.

The coil needs to be designed such that a high and homogeneous  $\mathbf{B}_2$ -field is provided at the sample position. In the rotating frame,  $\mathbf{B}_2$  at the center of a solenoid is given by [28]:

$$B_2 = \frac{\mu_0 \cdot N \cdot I}{2 \cdot h \cdot \sqrt{1 + 4\left(\frac{r}{h}\right)^2}}, \quad (5.3)$$

where  $\mu_0$  is the permeability of vacuum,  $N$  is the number of turns,  $r$  and  $h$  are the radius and height of the coil, and  $I$  is the current leading through the coil as given by Equation 5.1. In order to obtain a maximum  $\mathbf{B}_2$ -field, the coil needed to be mounted as close as possible to the resonator, and was therefore designed in a flat geometry as depicted in Figure 5.3. Furthermore, for achieving maximum homogeneity in  $\mathbf{B}_2$ , a rectangular geometry was chosen. The minimum distance between the two pairs of turns is restricted to  $h = 5.8$  mm by the width of the cavity holder at the sample position as depicted in Figure 5.1.

The power  $P$  reaching the coil is given by  $P/P_0 = 1 - |r|$ , with  $r$  being the reflection coefficient given by Equation 5.2. Therefore, for an optimum ENDOR performance not only a strong  $\mathbf{B}_2$ -field at the sample position but also matching is crucial, both of which strongly depend on the inductance of the coil. The inductance  $L$  of a finite, multiturn, single layer RF solenoid can e.g. be calculated

via [28]:

$$L = \frac{4 \cdot N^2 \cdot r^2 \cdot (1 - 0.2/N)}{h + 1.2 \cdot r^{0.9}}, \quad (5.4)$$

given in nH, where  $N$  is the number of turns,  $h$  is the overall axial length, and  $r$  is the effective inside radius (for  $h/r > 0.2$  and dimensions in mm). Although the ENDOR coil used in the present setup is not a solenoid but a saddle coil and the condition  $h/r > 0.2$  does not hold, Equation 5.4 was used to determine the influence of the coil geometry on the frequency dependence of  $\mathbf{B}_2$  as well as the reflections on a qualitative level, using Equations 5.3 and 5.2. The calculated frequency dependence showed that a maximum  $\mathbf{B}_2$  and minimized reflections can be obtained when choosing  $r$  as small as possible. However, a small radius conflicts with a homogeneous RF field. Furthermore, although only critical at low frequencies, a maximum  $\mathbf{B}_2$  demands for a large height, which in turn conflicts with increased reflections. As expected, an increased number of turns is beneficial for the RF field but will cause increased reflections. The calculated reflection coefficients are in line with the frequency dependence of the VSWR<sup>1</sup> measured for coils with 2.5, 4.5 and 7 turns (see Appendix B). An increase of the VSWR is observed at increasing frequencies as well as when using more turns. Overall, the observed VSWR frequency dependence as well as the calculated reflection coefficients and  $\mathbf{B}_2$ -field strengths demonstrate how difficult it is to predict the coil dimensions from these values for achieving an optimum ENDOR performance. Therefore, the approach for finding the coil dimensions for yielding an optimum  $^1\text{H}$ -ENDOR effect with the present setup was via measuring the ENDOR effect using different coil geometries.

### 5.3 Characterization of the Setup and Performance for $^1\text{H}$ -ENDOR

Before describing the performance of the ENDOR setup for  $^1\text{H}$ -ENDOR on the model system BDPA as well as on the biological sample Ras • Mn<sup>2+</sup> • GDP in the following two subsections, the main characteristics of the RF transmission system are described.

---

<sup>1</sup>The VSWR is given by  $\frac{1+\gamma}{1-\gamma}$ , where  $\gamma$  is the ratio between the reflected power and the incoming power.

### 5.3.1 The ENDOR setup at 180 GHz

The RF transmitter unit as depicted in Figure 5.4 was implemented into the pulsed 180 GHz EPR spectrometer described earlier on in Refs. 10 and 9. It consists of an RF synthesizer (Rohde und Schwartz, SMY 01, 9 kHz–1.040 GHz), a high-speed PIN switch with 5 ns rise/fall time (Synergy Microwave Corporation, model AK-711S, 5–400 MHz) and an RF amplifier with 400 W pulsed power (Dressler, LPPA 3004, 30–320 MHz). For the extension of the setup to low- $\gamma$  nuclei, an RF amplifier with 2000 W peak-to-peak power operating from 1–100 MHz (Dressler, LPPA 10020) can replace the former. The probehead for ENDOR experiments was equipped with a broadband RF circuit, in which the RF pulses are guided to one side of the coil via a low-loss shielded microflex cable (Telemeter Electronic, Micropore 190) and inside the cryostat via a semirigid stainless steel cable (purchased from Bruker Biospin GmbH). The other side of the RF coil is connected to a 30 dB high power attenuator (Weinschol Associates, WA 53-30-43, DC–2 GHz) acting as a 50  $\Omega$  load via a semirigid cable inside the cryostat and via a microflex cable outside the cryostat. In order to regulate the incoming RF power, an RF attenuator with variable attenuation from 0 to 50 dB in 1 dB steps (Tactron, model 50DR-003, DC–1000 MHz) was purchased. For measuring the reflected and incoming power of the RF circuit, a bidirectional coupler (Telemeter Electronic, RFC 10300-2000P) can be introduced into the circuit.

The performance of the setup for  $^1\text{H}$ -ENDOR (see next subsection) was tested using the model system BDPA for different coils with 2.5, 4.5 and 7 turns, in flat and solenoid shape, as well as using different wire widths, investigating the  $^1\text{H}$ -ENDOR effect as well as the VSWR (see previous section). An optimum ENDOR effect was observed using a 4.5-turn flat coil with an inner diameter of approximately 3 mm, made out of insulated 0.5 mm copper wire which was attached as close as possible to the cavity holder (see Figure 5.1). The cylindrical  $\text{TE}_{011}$  cavity was modified for ENDOR experiments to allow RF penetration by introducing six slots of 0.3 mm width, 0.75 mm apart, for which the quality factor was measured to be  $Q_{\text{loaded}} \approx 900 \pm 300$ . In order to reduce Eddy currents and heating effects, the cavity holder as well as the two plungers were made out of *G10* (purchased from Altec Plastics) with copper caps at the ends facing the cavity. This setup allows for typical RF  $\pi$ -pulses for  $^1\text{H}$  excitation of  $30 \pm 5 \mu\text{s}$  and MW  $\pi/2$ -pulse lengths of 70–90 ns, corresponding to a  $B_1$  of 0.10–0.12 mT at the

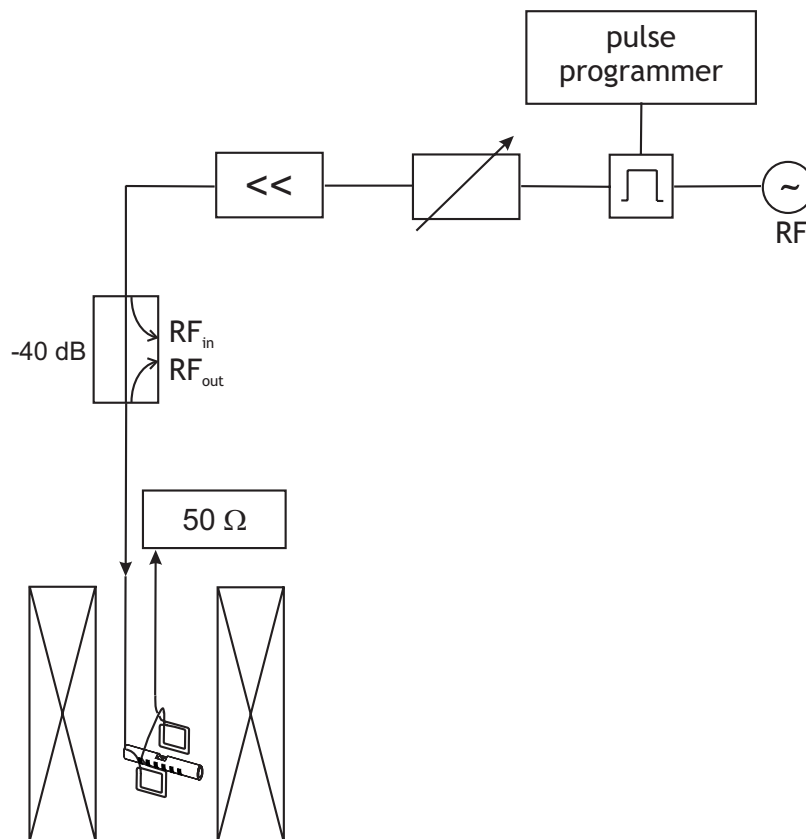


**Figure 5.4** Schematic drawing of the broadband radio frequency transmitter unit with RF synthesizer, high-speed PIN switch, attenuator, amplifier and coupler terminated by a  $50\ \Omega$  load as described in the text.

sample position. Rabi oscillations could not be observed on the test sample BDPA either because the sample was not evacuated, leading to a small  $T_2$  preventing the detection of Rabi oscillations, or because of an inhomogeneous  $\mathbf{B}_2$ -field. Still, the  $\mathbf{B}_2$ -field strength at the sample position was estimated to be at most  $0.8 \pm 0.1$  mT, by measuring the ENDOR effect as a function of the duration of the RF pulse via  $\mathbf{B}_2 = \pi/(\gamma t_{RF})$ .

### 5.3.2 Performance for $S = 1/2$ Systems: BDPA

Mims and Davies ENDOR on BDPA in polystyrene (with approximately  $4 \cdot 10^{16}$  spins in the active sample volume) were used to test the performance of our setup for  $^1\text{H}$ -ENDOR. As described in Chapter 2, the Davies sequence is sensitive to couplings larger than about 5 MHz, and the maximum ENDOR effect is obtained

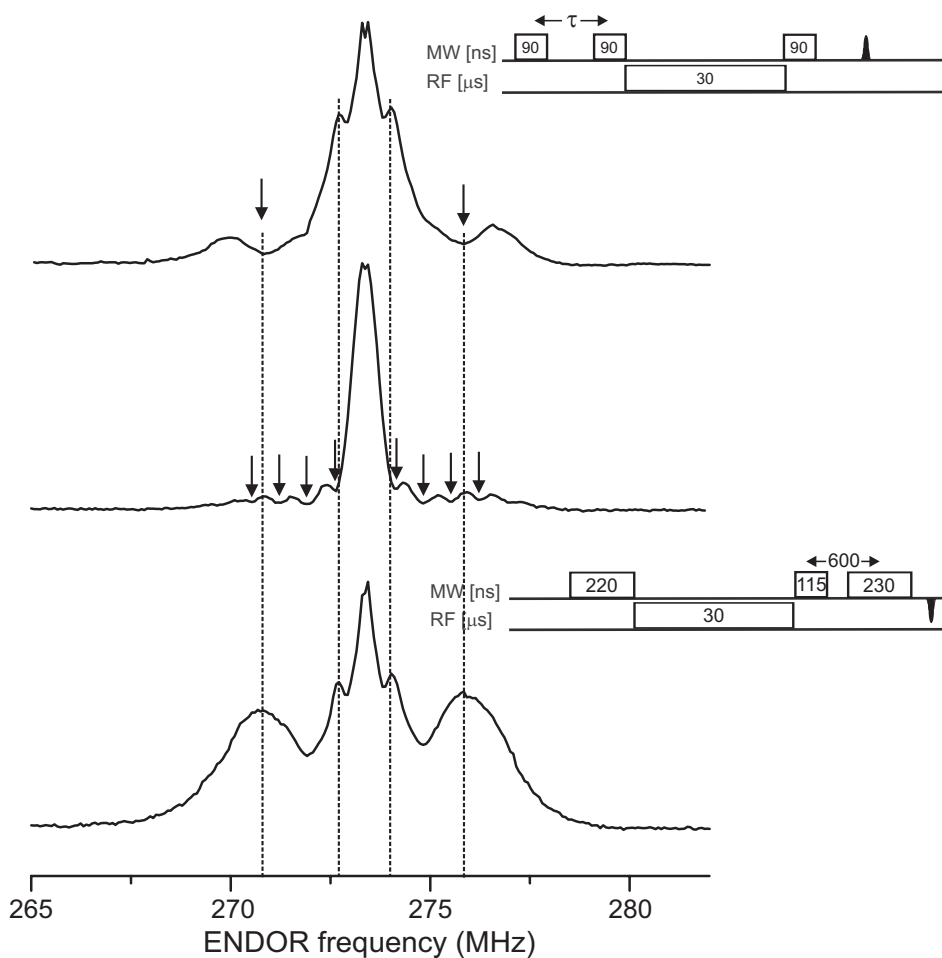


**Figure 5.5**  $^1\text{H}$ -Mims (top and middle) and Davies (bottom) ENDOR spectra of BDPA in polystyrene ( $\approx 4 \cdot 10^{16}$  spins in the active sample volume) measured at 180 K, with 128 shots per point using the pulse sequence shown in the insets and a SRT of 10 ms. The holes in the ENDOR spectrum due by the polarization pattern created by the Mims preparation sequence are observed using two different  $\tau$ -values, 200 and 700 ns (top and middle spectrum, respectively), as indicated by the arrows.

using selective, long preparation pulses [29]. In contrast, Mims ENDOR [30] is used for couplings smaller than  $\sim 5$  MHz. Figure 5.5 shows the single-scan  $^1\text{H}$ -ENDOR spectra acquired at 180 K using the pulse sequences shown in the inset. The observed features as well as the sensitivity of the setup for detecting proton resonances using the Mims and Davies ENDOR sequences are discussed in the following.

In order to demonstrate the effect of the preparation pulses on the polarization pattern for the Mims ENDOR sequence, spectra were recorded for two different

$\tau$ -values. Blind spots are observed at 2.5 MHz and 0.7 MHz for  $\tau = 200$  ns and  $\tau = n \cdot 700$  ns, respectively, according to  $\nu = 2n\pi/\tau$ . In BDPA, two sets of magnetically equivalent protons lead to one small and one large hyperfine splitting ( $A_1 = 1.4$  MHz and  $A_2 = 5.0$  MHz) [5], indicated by the dotted lines in Figure 5.5. It is known that the Mims ENDOR effect on the matrix line is very sensitive to the  $\tau$ -value [31, 32]. We find an ENDOR effect of  $25 \pm 5$  versus  $75 \pm 5\%$  of the echo amplitude when going from  $\tau = 200$  to 700 ns. In comparison, an ENDOR effect of  $25 \pm 5\%$  is observed on the maximum when using the Davies pulse sequence with MW pulse lengths of 200–220 ns (achieved by attenuation of the MW power by 1.5–2 dB).

### 5.3.3 Performance for $S = 5/2$ Systems: Ras•Mn $^{2+}$ •GDP

One of the motivations for building the present ENDOR setup was to measure the ligation sphere in Ras (see Chapter 4). The ENDOR studies reported in Chapter 4 were performed at 94 GHz for studying the  $^{31}\text{P}$  and  $^{13}\text{C}$  resonances of the metal ion and yielded information about differences between the wild-type protein and the G12V oncogenic mutant of the protein in both switch states [33, 34]. In the following, the first representative application of 180 GHz pulsed  $^1\text{H}$ -ENDOR for studying the active site in Ras•Mn $^{2+}$ •GDP is reported.

$^1\text{H}$ -Mims and Davies ENDOR spectra of 1 mM Ras(wt)•Mn $^{2+}$ •GDP solved in H $_2$ O acquired at 4 K are shown in Figure 5.6, using the experimental parameters listed in the figure caption. In order to inhibit damage from freezing, sugar was added to the sample solution as cryoprotectant [35]. For this system,  $^1\text{H}$  couplings are expected from the bound water molecules as well as from the protons of the surrounding amino acids and from the second solvation shell. In the Davies ENDOR spectrum, at least two splittings of  $\sim 2.5$  and  $\sim 7.5$  MHz are observed. Mims ENDOR was used to better resolve the hyperfine coupling constants in the range of  $\sim 3$  MHz, and the resulting ENDOR spectrum shows at least three splittings of 2.6, 2.1 and 1.4 MHz. In the following, the observed patterns are compared with experimental hyperfine couplings of protons located in the surroundings of Mn $^{2+}$  in biological and model systems reported in the literature.

The splittings observed in the Davies spectrum lie in the range of HFCs reported in the literature for directly bound water in the  $[\text{Mn}(\text{H}_2\text{O})_6]^{2+}$  complex, for which the reported values vary within the range of  $2.0 \leq A_{\perp} \leq 2.5$  MHz and  $7.3 \leq A_{\parallel} \leq 8.21$  MHz [6, 36]. The observed coupling of  $\approx 7.5$  MHz is also in the

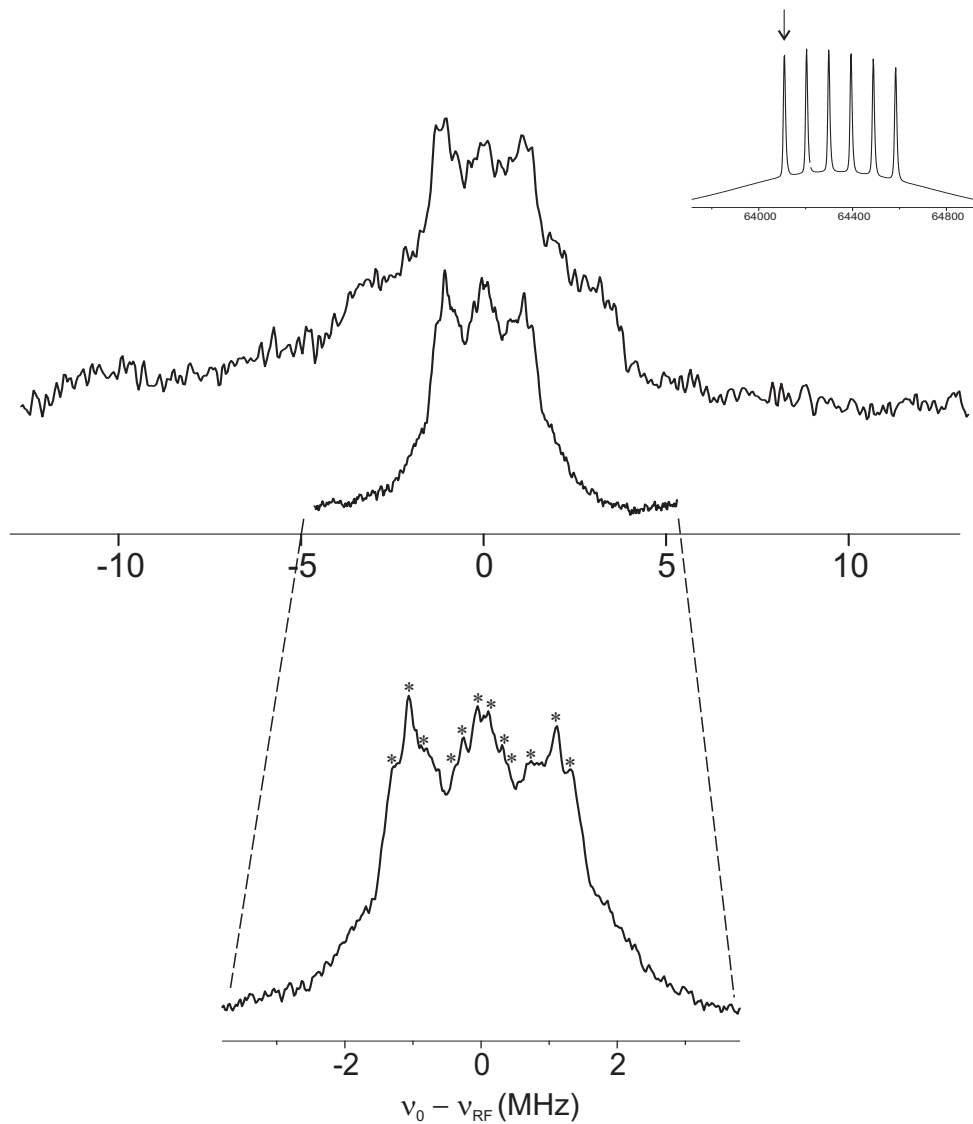


**Figure 5.6**  $^1\text{H}$ -Mims (bottom) and Davies (top) ENDOR spectra of Ras•Mn $^{2+}$ •GDP solved in H $_2$ O ( $\sim 1$  mM) with sugar added to the sample solution. The spectra were measured at the field position indicated by the arrow in the inset showing the field-swept, echo-detected EPR spectrum. Experimental parameters:  $T = 4$  K,  $t_{\text{RF}} = 20$   $\mu\text{s}$ , SRT = 10 ms; Mims:  $t_{\pi/2} = 40$  ns,  $\tau = 125$  ns, 9 scans with 128 shots per point; Davies:  $t_{1\pi} = 150$  ns,  $t_{1\pi} = 140$  ns,  $\tau = 500$  ns, 4 scans with 32 shots per point.



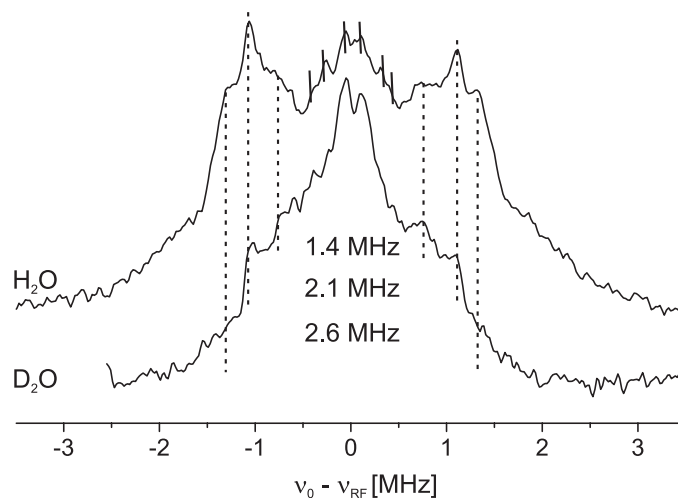


**Figure 5.7** Comparison of  $^1\text{H}$ -Mims ENDOR spectra of  $\text{Ras} \cdot \text{Mn}^{2+} \cdot \text{GDP}$  (1 mM) measured in  $\text{H}_2\text{O}$  (top) and  $\text{D}_2\text{O}$  (bottom) at  $T = 4$  K. Experimental parameters:  $\text{H}_2\text{O}$ : see Figure 5.6;  $\text{D}_2\text{O}$ :  $t_{\text{RF}} = 20 \mu\text{s}$ ,  $\text{SRT} = 10$  ms,  $t_{\pi/2} = 40$  ns,  $\tau = 125$  ns, 11 scans with 128 shots per point. The dashed lines mark the observed splittings of 1.4, 2.1 and 2.6 MHz as discussed in the text.

range of reported HFCs for directly bound water in Concanavalin (5.4 to 8.2 MHz [37]). Couplings  $2.9 \leq A_{\perp} \leq 4.3$  MHz observed in Concanavalin A for bound water [37] could not be found in the present spectra. On the basis of this comparison, the observed couplings in the Davies ENDOR spectra can be tentatively assigned to directly bound water, with  $A_{\perp} \approx 2.5$  MHz and  $A_{\parallel} \approx 7.5$  MHz.

The interpretation of the peaks observed in the Mims ENDOR spectrum (2.6, 2.1 and 1.4 MHz) is less evident. Assuming a purely dipolar coupling mechanism, one can estimate the point-dipole distances of these protons. The calculated distances of 3.1 to 3.8 Å lie in the range of protons from surrounding amino acids as was found in Concanavalin A ( $A_{\perp} \approx 2.0$  MHz) [37] as well as of hyperfine couplings reported in the literature for directly bound water ( $A_{\perp} = -2.5$  MHz [6],  $-2.4$  MHz [36] and  $|A_{\perp}| = 2.0$  MHz [38]). Smaller peaks observed on the central peak could arise either from further distant amino acids or from water protons in the second solvation shell as found by studies of the  $[\text{Mn}(\text{H}_2\text{O})_6]^{2+}$  complex (0.5 and 1.0 MHz) by Morrissey et al. [38].

To distinguish between protons from directly bound water and from surrounding amino acids is to compare the  $^1\text{H}$ -ENDOR spectra of the protein solved in  $\text{D}_2\text{O}$  with the spectra of the protein solved in  $\text{H}_2\text{O}$  as depicted in Figure 5.7. The

HFCs of exchangeable protons should no longer be visible in the spectra of the protein solved in D<sub>2</sub>O. It appears plausible that at least the coupling of 2.6 MHz originates from exchangeable protons. Along with the information of the Davies ENDOR spectra, it is likely that these belong to directly bound water, however this is still rather speculative. In order to find more evidence for this assumption, it would be helpful to perform <sup>2</sup>H-ENDOR on the same system (see the following section).

## 5.4 Summary and Outlook

In the following, the performance of the broadband RF circuit designed for the use of <sup>1</sup>H-ENDOR implemented into the pulsed EPR spectrometer operating at 180 GHz [9, 10] is summarized. The performance of the setup will be discussed in comparison to high-field pulsed ENDOR spectrometers reported in the literature along with possible future changes of the setup for improving its performance.

Because of its simplicity and broadband characteristics, an *RL* circuit terminated with a 50 Ω load was chosen for <sup>1</sup>H-ENDOR experiments. This RF circuit allows to sweep the frequency over a broad frequency range and therefore to detect also larger proton HFCs from 10–20 MHz e.g. typical for protons in biological systems containing Mn<sup>2+</sup>. The Mims and Davies ENDOR spectra of BDPA, which was used as a model system to test the performance of the setup for <sup>1</sup>H-ENDOR, acquired at 180 K with an RF output power of ≈ 400 W, showed an ENDOR effect of 25–75% (depending on the  $\tau$ -value) and 25%, respectively. Furthermore, <sup>1</sup>H-Mims and Davies ENDOR spectra at 4 K were obtained for a solution containing 1 mM Ras • Mn<sup>2+</sup> • GDP.

From the dependence of the ENDOR effect on the RF pulse length and RF-pulse of  $30 \pm 5 \mu\text{s}$  yielded an optimum ENDOR effect for <sup>1</sup>H-excitation, from which the **B**<sub>2</sub>-field strength was estimated to be at most  $0.8 \pm 0.1 \text{ mT}$ . ENDOR setups operating at W-band frequencies described in the literature using tuned RF circuits with RF amplifiers delivering output powers of 3 kW [3] and 2.5 kW [1] report RF pulse lengths of  $35 \mu\text{s}$  and  $6 \pm 2 \mu\text{s}$ , yielding **B**<sub>2</sub>-field strengths of 2.1 and 2.5 mT, respectively. Considering that the RF amplifier used in the ENDOR setup reported here delivers less output power (400 W), the performance of the 180 GHz ENDOR setup lies well in the range of the ENDOR setups operating at 95 GHz. It is also comparable to the performance of the ENDOR setup reported

at 275 GHz [12], which equally uses a broadband RF circuit terminated with a  $50\ \Omega$  load for  $^1\text{H}$ -excitation and yields a  $\mathbf{B}_2$  of 1.0 mT, with 100 W pulsed power. The performance of the ENDOR setup may be further improved for measurements at low temperatures, where fluctuations of the electron spin echo intensity were observed with the present setup, decreasing the ENDOR efficiency. One reason for the echo instability may be mechanical instability of the tuning system caused by the helium flow and might be overcome with a more stable tuning system. Furthermore, a fixed teflon holder housing the RF coil as designed for other ENDOR probes [2, 3, 17] could be implemented into the setup to stabilise the RF coil and avoid problems with soldering in particular at low temperatures. Finally, the performance of the broadband circuit for nuclei with small gyromagnetic ratios should be tested and eventually, a tuned RF circuit with variable capacitors may yield an improved ENDOR efficiency for low and nuclei with high gyromagnetic ratio.

## References

- [1] Rohrer, M.; Plato, M.; MacMillan, F.; Grishin, Y.; Lubitz, W.; Möbius, K. *J. Magn. Res.* **1995**, *116*, 59–66.
- [2] Disselhorst, J. A. J. M.; van der Meer, H.; Poluektov, O. G.; Schmidt, J. *J. Magn. Res.* **1995**, *116*, 183–188.
- [3] Gromov, I.; Krymov, V.; Manikandan, P.; Arieli, D.; Goldfarb, D. *J. Magn. Res.* **1999**, *139*, 8–17.
- [4] Goldfarb, D.; Krymov, V. In *Very High Frequency ESR/EPR*, Vol. 22; Grinberg, O.; Berliner, L., Eds.; Plenum: New York, 2005.
- [5] Bennati, M.; Farrar, C. T.; Bryant, J. A.; Inati, S. J.; Weis, V.; Gerten, G. J.; Riggs-Gelasco, P.; Stubbe, J.; Griffin, R. G. *J. Magn. Res.* **1999**, *138*, 232–243.
- [6] Epel, B.; Manikandan, P.; Kroneck, H.; Goldfarb, D. *Appl. Magn. Res.* **2001**, *21*, 287–297.
- [7] Bennebroek, M.-T.; Schmidt, J. *J. Magn. Res.* **1997**, *128*, 199–206.
- [8] Reed, G. H.; Markham, G. D. *Biol. Magn. Res.* **1984**, *6*, 73–142.

- [9] Hertel, M. M.; Bennati, M.; Denysenkov, V.; Prisner, T. *Magn. Res. Chem.* **2005**, *43*, 248-255.
- [10] Rohrer, M.; Brüggmann, O.; Kinzer, B.; Prisner, T. F. *Appl. Magn. Res.* **2001**, *21*, 257-274.
- [11] Prisner, T.; Rohrer, M.; Möbius, K. *Appl. Magn. Res.* **1994**, *7*, 167-183.
- [12] Blok, H.; Disselhorst, J. A. J. M.; van der Meer, H.; Orlinskii, S. B.; Schmidt, J. *J. Magn. Res.* **2005**, *173*, 49-53.
- [13] Poluektov, O. G.; Schmidt, J. *Bruker Rep.* **1996**, *143*, 34-37.
- [14] Traficante, D. D. *Concepts in Magn. Res.* **1989**, *1*, 73-92.
- [15] Cook, R. J. *J. Sci. Instrum.* **1966**, *43*, 548-553.
- [16] Forrer, J.; Pfenninger, S.; Eisenegger, J.; Schweiger, A. *Rev. Sci. Instrum.* **1990**, *61*, 3360-3367.
- [17] Burghaus, O.; Rohrer, M.; Götzinger, T.; Plato, M.; Möbius, K. *Meas. Sci. Technol.* **1992**, *3*, 765-774.
- [18] Seck, M.; Wyder, P. *Rev. Sci. Instrum.* **1998**, *69*, 1817-1822.
- [19] Gromov, I.; Shane, J.; Forrer, J.; Rakhmatoullin, R.; Rozentzwaig, Y.; Schweiger, A. *J. Magn. Res.* **2001**, *149*, 196-203.
- [20] Avdievich, N. I.; Gerfen, G. J. *J. Magn. Res.* **2001**, *153*, 178-185.
- [21] Burghaus, O.; Toth-Kischkat, A.; Klette, R.; Möbius, K. *J. Magn. Res.* **1988**, *80*, 383-388.
- [22] Bender, C. J.; Babcock, G. T. *Rev. Sci. Instrum.* **1992**, *63*, 3523-3524.
- [23] Schmalbein, D.; Witte, A.; Röder, R.; Laukien, G. *Rev. Sci. Instrum.* **1972**, *43*, 1664-1665.
- [24] Peric, M.; Dulcic, A. *J. Phys. E: Sci. Instrum.* **1981**, *14*, 700-701.
- [25] Pfenninger, S. Thesis, ETH Zürich, 1991.
- [26] Forrer, J.; Pfenninger, S.; Wagner, B.; Weiland, T. *Pure and Appl. Chem.* **1992**, *64*, 865-872.

- [27] Höfer, P. Thesis, Institut für Physik, Universität Stuttgart, 1988.
- [28] Doty, D. D. In *Encyclopedia of NMR*; Grant, D. M.; Harris, R. K., Eds.; Wiley Press: 1996.
- [29] Davies, E. *Phys. Lett.* **1974**, *47A*, 1–2.
- [30] Mims, W. B. *Proc. R. Soc. London* **1965**, *283*, 452–457.
- [31] Grupp, A.; Mehring, M. In *Modern Pulsed and CW Electron Spin Resonance*; Kevan, L.; Bowman, M., Eds.; Wiley: New York, 1990.
- [32] Astashkin, A.; Kawamori, A. *J. Magn. Res.* **1998**, *135*, 406–417.
- [33] Bennati, M.; Hertel, M.; Fritscher, J.; Prisner, T. F.; Weiden, N.; Dinse, K. P.; Hofweber, R.; Spoerner, M.; Horn, G.; Kalbitzer, H. R. *Biochemistry* **2006**, *45*, 42–50.
- [34] Spoerner, M.; Nuehs, A.; Ganser, P.; Herrmann, C.; Wittinghofer, A.; Kalbitzer, H.-R. *Biochemistry* **2005**, *44*, 2225–2236.
- [35] Sutton, R. L. *J. Chem. Soc. Farad. Trans.* **1991**, *87*, 3747–3751.
- [36] Tan, X.; Bernando, M.; Thomann, H.; Scholes, C. P. *J. Chem. Phys.* **1992**, *98*, 5147–5157.
- [37] Carmieli, R.; Manikandan, P.; Kalb, A. J.; Goldfarb, D. *J. Am. Chem. Soc.* **2001**, *123*, 8378–8386.
- [38] Morrissey, S. R.; Horton, T. E.; DeRose, V. J. *J. Am. Chem. Soc.* **2000**, *122*, 3473–3481.



# Chapter 6

## Summary

In the first part of the present work (Chapter 3), EPR spectroscopy at different microwave frequencies, namely at 9 GHz (X-band), 34 GHz (Q-band) and 180 GHz (G-band), was employed to resolve the  $g$ -values and the HFCs of a putative radical intermediate involved in the reduction of benzoyl-CoA catalyzed by benzoyl-CoA reductase. In particular, the effect of  $^{33}\text{S}$ -labeling on the EPR line shape was studied at X- and Q-band frequencies in order to gain further evidence for a sulfur centered radical proposed to be the electron donor in the reduction of the aromatic ring of BCoA [1]. The spectral components observed at X-, Q- and G-band were overall consistent and showed at least three overlapping EPR signals. The signal postulated to be due to a disulfide radical anion showed no resolved  $g$ -values and a relaxation behaviour faster than expected for such a radical species. These observations together with the simulations suggest that the signal could arise from a radical exchange coupled to an [4Fe-4S] cluster located nearby. In the future, pulsed EPR and ENDOR spectroscopy on the  $^{57}\text{Fe}$ -labeled enzyme could help to solve this question.

The potential of high-field ENDOR in combination with  $^{13}\text{C}$ - and  $^{31}\text{P}$ -labeling for investigating the structure at the active site in proteins could be verified in the studies of the ligation sphere of the cofactor  $\text{Mn}^{2+}$  in Ras as reported in Chapter 4 [2]. Therein, high-field ENDOR performed at 94 GHz (W-band) was used to detect the hyperfine interactions between the electron spin mainly located on the metal ion and the phosphorous nuclei of the bound GDP and GppNHp as well as the carbon nuclei of bound amino acids in the wild-type Ras protein and its oncogenic mutant G12V. These studies aimed at searching for an additional free phosphate ion or amino acid ligand bound to the metal center in the wild type

GDP-bound protein with respect to its oncogenic mutant. From the  $^{13}\text{C}$ - and  $^{31}\text{P}$ -ENDOR spectra, the hyperfine couplings of directly bound amino acids and the bound nucleotides were compatible with the hyperfine couplings obtained from DFT calculations based on the crystal structure data. No differences in the  $^{13}\text{C}$ - and  $^{31}\text{P}$ -ENDOR spectra could be found for the wild-type GDP-bound protein in comparison to its oncogenic mutant in frozen solution. Therefore, no evidence for binding of an additional free phosphate ion or amino acid ligand in the wild-type GDP-bound protein was found. The distances between the detected nuclei and the metal ion were in agreement with the ones extracted from crystal structures reported in the literature. Future  $^{35}\text{Cl}$ -ENDOR studies could clarify whether a chloride ion from the buffer solution could be the ligand replacing one water molecule in the wild type GDP-bound Ras.

In Chapter 5, the implementation of a high-field ENDOR setup into a home-built pulsed EPR spectrometer operating at 180 GHz [3, 4] is reported and its performance for  $^1\text{H}$ -ENDOR demonstrated on the model system BDPA. Mims and Davies ENDOR spectra were also obtained for  $\text{Ras}(\text{wt}) \cdot \text{Mn}^{2+} \cdot \text{GDP}$ . The increased nuclear Zeeman resolution at 180 GHz may be further exploited in the future by extending the setup for studying hyperfine couplings of low- $\gamma$  nuclei such as  $^{33}\text{S}$ ,  $^{15}\text{N}$ ,  $^{17}\text{O}$  or  $^2\text{H}$ .

In the present work, the advantages of performing EPR and ENDOR experiments at high fields and frequencies could be nicely demonstrated with the 94 GHz ENDOR studies of Ras. Furthermore, the complementing information obtained at X- and Q-band frequencies in the multifrequency EPR studies on BCR demonstrated that the analysis of EPR spectra can be greatly facilitated by simulating the spectra measured at different MW frequencies with the same set of parameters consistent with a proposed radical. Overall, it could be shown that the use of different experimental techniques at multiple fields and frequencies renders EPR spectroscopy a powerful tool for structural studies in biological systems.

## References

- [1] Boll, M.; Schink, B.; Messerschmidt, A.; Kroneck, P. M. H. *Biol. Chem.* **2005**, *386*, 999–1006.
- [2] Bennati, M.; Hertel, M.; Fritscher, J.; Prisner, T. F.; Weiden, N.;



- Dinse, K. P.; Hofweber, R.; Spoerner, M.; Horn, G.; Kalbitzer, H. R. *Biochemistry* **2006**, *45*, 42–50.
- [3] Hertel, M. M.; Bennati, M.; Denysenkov, V.; Prisner, T. *Magn. Res. Chem.* **2005**, *43*, 248–255.
- [4] Rohrer, M.; Brüggmann, O.; Kinzer, B.; Prisner, T. F. *Appl. Magn. Res.* **2001**, *21*, 257–274.



# Chapter 7

## Zusammenfassung

Die vorliegende Arbeit befasst sich mit der Identifizierung von radikalischen Intermediaten, welche an der Reduktion von Benzoyl-CoA (BCoA) durch Benzoyl-CoA-Reduktase (BCR) beteiligt sind, sowie mit strukturellen Untersuchungen der aktiven Bindungsstelle im G-Protein Ras mit Hilfe von elektronenparamagnetischer Resonanz- (EPR) und Elektronen-Kern-Doppelresonanz- (ENDOR) Spektroskopie. Die zahlreichen Vorteile, EPR- und ENDOR-Experimente bei hohen Frequenzen und Feldern durchzuführen, im besonderen an Hochspin-Systemen wie Mn(II), lieferten die Motivation, einen ENDOR-Aufbau in ein gepulstes Eigenbau-180-GHz-EPR-Spektrometer zu implementieren [1, 2] .

EPR-spektroskopische Methoden haben sich in der Vergangenheit erfolgreich bewährt, um die Struktur und Funktion von aktiven Zentren in Metallproteinen zu untersuchen [3, 4]. Mit Hilfe von EPR-Spektroskopie können Hyperfeinkopplungen zwischen dem Elektronenspin und Kernspins von Kernen in der Nähe des paramagnetischen Metallions gewonnen werden [5, 6]. Hyperfeinkopplungen stellen eine bedeutende Informationsquelle bei der Untersuchung katalytischer Mechanismen, der Struktur sowie der Koordinationsgeometrie von paramagnetischen Metallzentren dar. Die Hyperfeinkopplungen können entweder aus der Aufspaltung der EPR-Linien oder über Doppelresonanzmethoden wie z.B. ENDOR-Spektroskopie gewonnen werden. In einem ENDOR-Experiment wird das kernmagnetische Resonanz- (NMR) Spektrum von Kernen, welche mit dem paramagnetischen Zentrum wechselwirken, über die Änderung der EPR-Signalintensität durch Anregung der Kernübergänge bei Radiofrequenz-Einstrahlung aufgenommen.

Bei der Untersuchung biologischer Systeme mittels EPR-Spektroskopie wird

die Interpretation der Spektren häufig durch die Überlagerung von mehreren überlappenden EPR-Signalen, welche von verschiedenen Spezies in der Probe stammen, erschwert. In diesem Zusammenhang haben sich in der Vergangenheit die Verwendung von hohen Mikrowellenfrequenzen sowie der Gebrauch von gepulsten Methoden als hilfreich erwiesen, um die von verschiedenen paramagnetischen Zentren stammenden EPR-Signale zu trennen. Dabei wird die erhöhte spektrale Auflösung bei hohen Feldern, sowie die zusätzliche Dimension der Zeit, welche gepulste Verfahren mit sich bringen, genutzt, um die Signale anhand ihres unterschiedlichen Relaxationsverhaltens zu trennen [7–9]. Ein wichtiges Werkzeug bei der Analyse von EPR-Spektren ist die Möglichkeit, die Spektren unter Verwendung eines Parametersatzes, welcher mit einem vorgeschlagenen Struktur-Modell kompatibel ist, bei verschiedenen Mikrowellenfrequenzen zu simulieren.

In den in Kapitel 3 beschriebenen EPR-spektroskopischen Untersuchungen wurden EPR-Experimente bei verschiedenen Frequenzen in Kombination mit Rapid-Freeze-Quench-Techniken angewandt, um radikalische Intermediate, welche an der Reduktion von Benzoyl-CoA durch Benzoyl-CoA-Reduktase beteiligt sind, zu identifizieren. Die Biochemie von BCR, einem zentralen Enzym im anaeroben Stoffwechsel aromatischer Komponenten in anaeroben Bakterien, wurde bis heute allein in der anaeroben Bakterie *Thauera aromatica* untersucht [10]. Im Gegensatz zu aeroben Bakterien verwenden anaerobe Mikroben aromatische Komponenten als Kohlenstoff-, Stickstoff-, oder Energiequelle, indem sie den aromatischen Ring nicht über oxidative sondern über reduktive Schritte abbauen. Seit der Entdeckung der anaeroben Spaltung aromatischer Komponenten in den 1980er Jahren wurden drei Schlüssel-Intermediate identifiziert, über welche mononukleare aromatische Komponenten abgebaut werden: Benzoyl-CoA, Resorcinol sowie Phloroglucinol [10]. Der BCoA-Weg erscheint der wichtigste zu sein, da eine große Vielzahl von Komponenten über diesen Weg abgebaut werden, unter ihnen Phenol. In den ersten Schritten des anaeroben Phenol-Stoffwechselweges wird BCoA mit Hilfe von BCR über eine ATP-abhängige Reduktion des Benzol-Rings zu einer nicht-aromatischen zyklischen Dienoyl-CoA-Komponente reduziert.

Es wurde vorgeschlagen, dass die Reduktion des aromatischen Rings von BCoA durch BCR über alternierende Schritte von Ein-Elektronen- und Protonen-Transfer verläuft, in Analogie zur chemischen Birchreduktion [11, 12]. In dieser Reaktionsfolge wird der erste Elektronentransfer auf das Substrat als geschwindigkeitsbestimmender Schritt betrachtet, welcher ein besonders niedriges Redox-

potential von  $-1.9$  V erfordert [13]. Es wurde gezeigt, dass BCR den Zwei-Elektronen-Übertrag von reduziertem Ferredoxin auf den aromatischen Ring an die Hydrolyse von zwei ATP-Molekülen zu ADP und  $P_i$  koppelt. Frühere Single-Turnover-Studien von BCR mit Hilfe von Rapid-Freeze-Quench-EPR, in denen radikalische Intermediate durch Zugabe des kompetitiven Inhibitors 4-Fluorobenzoyl-CoA (4-F-BCoA) zu einer Lösung von reduziertem BCR erfasst wurden, zeigten die Anwesenheit von zwei transienten Radikalen [14, 15]. Aufgrund der in diesen EPR- und Stopped-Flow-UV-Vis-Studien erzielten Daten wurde ein Disulfidradikalanion als Elektronendonator im ersten Schritt der Reduktion des aromatischen Rings von BCoA vorgeschlagen [16].

Das Ziel der vorliegenden Arbeit war es, mit Hilfe von Multifrequenz-EPR-Spektroskopie die  $g$ -Werte und Hyperfeinkopplungen des vermeintlichen radikalischen Intermediates zu bestimmen. Hierzu wurden EPR-Experimente bei verschiedenen Frequenzen, bei 9 GHz (X-Band), 34 GHz (Q-Band) und 180 GHz (G-Band), durchgeführt, und insbesondere den Einfluss von  $^{33}\text{S}$ -Markierung auf die EPR-Linienform untersucht. Die spektralen Komponenten, welche im X-, Q- und G-Band beobachtet wurden, waren in sich konsistent und zeigten mindestens drei EPR-Signale. Das vermeintlich von einem Disulfidradikalanion stammende Signal zeigte keine aufgelösten  $g$ -Werte und kürzere Relaxationszeiten als typisch für solch eine Spezies. Die experimentellen Beobachtungen zusammen mit den Simulationen legten nahe, dass das Signal von einem an einen [4Fe-4S]-Cluster austauschgekoppeltes Radikal stammt.

In Fällen, in denen die durch die Hyperfeinkopplungen erzeugten Aufspaltungen der EPR-Linien durch die Linienbreite verdeckt sind, können diese Kopplungen oft mit Hilfe von ENDOR-Spektroskopie erhalten werden. Im Vergleich zu EPR-spektroskopischen Methoden kann die Auflösung in ENDOR-Experimenten bis zu drei Größenordnungen größer sein, was es erlaubt, Hyperfeinwechselwirkungen in Systemen zu detektieren, deren zugehörige EPR-Spektren keine aufgelöste Hyperfeinstruktur aufweisen. Über die Hyperfeinkopplungskonstanten, welche aus den ENDOR Spektren gewonnen werden können, können mit Hilfe des Punkt-Dipol-Modells (siehe Kapitel 2) Abstände zwischen dem paramagnetischen Zentrum und umliegenden Kernen bestimmt und damit strukturelle Informationen über aktive Zentren in Proteinen erhalten werden [5].

Ähnlich wie in EPR-Experimenten entstehen zahlreiche Vorteile, wenn ENDOR-Spektren bei hohen Frequenzen und Feldern aufgenommen werden [17–19]. Zu den Vorteilen gehören z.B. die erhöhte Kern-Zeeman-Auflösung, welche zur Tren-

nung von ENDOR-Signalen von verschiedenen Kernen führt, und insbesondere die Detektion von Kernen mit geringem gyromagnetischen Verhältnis erleichtert. Des Weiteren kann in vielen Fällen die erhöhte Boltzmannpolarisation bei hohen Feldern und tiefen Temperaturen ausgenutzt werden, um das absolute Vorzeichen der Hyperfeinkopplungskonstanten zu bestimmen [20].

Die oben genannten Vorteile wurden in der vorliegenden Arbeit genutzt, um die Struktur des aktiven Zentrums im Ras-Protein zu bestimmen, wie in Kapitel 4 beschrieben [21]. Am aktiven Zentrum bindet ein  $Mg^{2+}$ -Ion an ein Guanosin-5'-Diphosphat (GDP) im inaktiven Zustand des Proteins und an ein Guanosin-5'-Triphosphat (GTP) im aktiven Zustand des Proteins [22]. Als Mitglied der Familie der kleinen G-Proteine (Guanosin-Nukleotid-bindende Proteine) schaltet Ras zwischen dem GDP-gebundenen inaktiven Zustand und dem GTP-gebundenen aktiven Zustand, um so als molekularer Schalter bei der Weiterleitung von Zellsignalen zu agieren, indem es wichtige Prozesse wie Zellteilung, -wachstum, und -apoptose reguliert. In der GTP-gebundenen Form interagiert das Protein mit sogenannten Effektoren, welche deren Aktivität innerhalb der Zelle lenken. Zur Aktivierung des inaktiven Proteins muss GDP durch GTP ausgetauscht werden. Diese Reaktion erfordert Guanosin-Nukleotid-Austauschfaktoren (GEFs), um die Abgabe des normalerweise fest gebundenem GDP zu katalysieren, welches anschließend durch reichlich in der Zelle enthaltenes GTP ausgetauscht wird. Durch die Hydrolyse von GTP wird das Protein wieder "ausgeschaltet", entweder durch die intrinsische GTPase-Aktivität von Ras oder durch GTPase-aktivierende Proteine (GAPs). Diese Reaktion befördert Ras in seinen inaktiven GDP-gebundenen Zustand zurück, wodurch die Bindung an die Effektoren gelöst wird und so die Weiterleitung von Signalen gestoppt wird.

Spezifische onkogene Mutanten von Ras enthalten Punktmutationen am aktiven Zentrum, welche die GTPase-Aktivität blockieren, zur Anreicherung von Ras im aktiven Zustand führen und dadurch zur Tumorbildung beitragen [23]. Da der Austausch der Nukleotide, welche die Aktivierung des Proteins kontrollieren, am aktiven Zentrum erfolgt, ist die Kenntnis der Struktur an diesem Zentrum besonders wichtig für das Verständnis der Entstehung von Krebs. In den veröffentlichten Kristallstrukturen von Ras in seinem GDP- sowie im GTP-gebundenen Zustand wurden keine Unterschiede in der Ligandensphäre des Metall-Ions im Wildtyp-Protein im Vergleich zu den onkogenen Mutante gefunden [24–31]. Die Struktur des aktiven Zentrums wurde bisher von einigen Gruppen mit Hilfe von EPR-spektroskopischen Methoden untersucht, nachdem das dia-

magnetische  $\text{Mg}^{2+}$ -Ion durch ein paramagnetisches  $\text{Mn}^{2+}$ -Ion ersetzt wurde [32–41]. Insbesondere haben Hochfeld-EPR-spektroskopische Studien, in welchen die  $^{17}\text{O}$ -induzierte Linienverbreiterung auf den  $m_S = +\frac{1}{2} \leftrightarrow -\frac{1}{2}$  EPR-Übergängen der GDP-Komplexe in  $^{17}\text{O}$ -markiertem Wasser analysiert wurde, einen Unterschied in der Ligandensphäre des Wildtyps im Vergleich zur onkogenen Mutante Ras(G12V) detektiert: nur drei Wassermoleküle wurden im Wildtyp-Protein gefunden im Vergleich zu vier in der G12V Mutante [1]. Desweiteren hatten frühere  $^{31}\text{P}$ -NMR Studien gezeigt, dass in flüssiger Lösung mehrere konformationelle Zustände im GDP- und im GTP-gebundenen Zustand nebeneinander existieren [32, 42].

In Kapitel 4 dieser Arbeit werden ENDOR-spektroskopische Untersuchungen bei 94 GHz (W-Band) beschrieben, welche vorgenommen wurden, um die Ligandensphäre des  $\text{Mn}^{2+}$ -Ions im GDP- sowie im GTP-gebundenen Zustand zu charakterisieren [21]. In Kombination mit  $^{13}\text{C}$ - und  $^{31}\text{P}$ -Markierung konnten die ENDOR-Resonanzen der Kerne in der ersten Ligandensphäre mit hoher spektraler Auflösung detektiert werden. Die Frage nach einem Liganden, welcher das Wassermolekül im GDP-gebundenen Wildtyp ersetzen könnte, wurde mit Hilfe von  $^{13}\text{C}$ - und  $^{31}\text{P}$ -ENDOR untersucht. Aus den ENDOR-Spektren konnten die Hyperfeinkopplungen von direkt gebundenen Aminosäuren sowie vom gebundenen Nukleotid bestimmt werden, in Übereinkunft mit aus Dichte-Funktional-Theorie-Rechnungen gewonnenen Werten. Es konnten keine Unterschiede in den ENDOR-Spektren des Wildtyp-Proteins und der onkogenen Mutanten gefunden werden und demnach kein Hinweis auf Bindung einer zusätzlich gebundenen Aminosäure oder eines freien Phosphat-Ions im Vergleich zur onkogenen Mutante in gefrorener Lösung gefunden werden. Die Abstände zwischen den detektierten Kernen und dem Metallzentrum waren in Übereinstimmung mit den Kristallstrukturdaten aus der Literatur. Zukünftige  $^{35}\text{Cl}$ -ENDOR-Experimente könnten helfen herauszufinden, ob ein Chlorid-Ion aus der Pufferlösung der Ligand ist, welcher ein Wassermolekül im Wildtyp-GDP-gebundenen Protein ersetzt.

Die Implementierung eines Hochfeld-ENDOR Aufbaus in ein Eigenbau-EPR-Spektrometer bei 180 GHz wird im letzten Teil der Arbeit beschrieben [2]. Zur Durchführung von ENDOR-Experimenten bei 180 GHz wurde ein breitbandiger Radiofrequenzkreis konstruiert und die Leistungsfähigkeit des Aufbaus für  $^1\text{H}$ -ENDOR am Modellsystem Bisdiphenylen-phenyl-allyl unter Verwendung der Mims- sowie der Davies-ENDOR-Pulssequenzen unter Beweis gestellt. Des weiteren wurde die Anwendbarkeit des ENDOR-Aufbaus auf biologische Systeme an

Ras • Mn<sup>2+</sup> • GDP getestet.

## References

- [1] Rohrer, M.; Brüggmann, O.; Kinzer, B.; Prisner, T. F. *Appl. Magn. Res.* **2001**, *21*, 257–274.
- [2] Hertel, M. M.; Bennati, M.; Denysenkov, V.; Prisner, T. *Magn. Res. Chem.* **2005**, *43*, 248–255.
- [3] Hoff, A. J. *Advanced EPR*; Elsevier, Amsterdam: 1990.
- [4] Hoffman, B. M. *Acc. Chem. Res.* **2003**, *36*, 522–529.
- [5] Abragam, A.; Bleaney, B. *Electron Paramagnetic Resonance of Transition Ions*; Dover Publications, New York: 1986.
- [6] Atherton, N. M. *Electron Spin Resonance*; Halstead, New York: 1973.
- [7] Bennati, M.; Prisner, T. F. *Rep. Prog. Phys.* **2005**, *68*, 411–448.
- [8] Grinberg, O.; Berliner, L. *Very High Frequency ESR/EPR*; volume 22 Plenum: New York, 2005.
- [9] Prisner, T. F. *Adv. Magn. Opt. Res.* **1997**, *20*, 245–300.
- [10] Heider, J.; Fuchs, G. *Eur. J. Biochem.* **1997**, *243*, 577–596.
- [11] Koch, J.; Eisenreich, W.; Bacher, A.; Fuchs, G. *Eur. J. Biochem.* **1993**, *211*, 649–661.
- [12] Buckel, W.; Keese, R. *Angew. Chem. Int. Ed.* **1995**, *34*, 1502–1506.
- [13] Boll, M.; Fuchs, G. *Eur. J. Biochem.* **1995**, *234*, 921–933.
- [14] Boll, M.; Laempe, D.; Eisenreich, W.; Bacher, A.; Mittelberger, T.; Heinze, J.; Fuchs, G. *J. Biol. Chem.* **2000**, *275*, 21889–21895.
- [15] Boll, M.; Fuchs, G.; Lowe, D. J. *Biochemistry* **2001**, *40*, 7612–7620.
- [16] Boll, M.; Fuchs, G. *Biol. Chem.* **2005**, *386*, 989–997.



- [17] Gromov, I.; Krymov, V.; Manikandan, P.; Arieli, D.; Goldfarb, D. *J. Magn. Res.* **1999**, *139*, 8–17.
- [18] Goldfarb, D.; Krymov, V. In *Very High Frequency ESR/EPR*, Vol. 22; Grinberg, O.; Berliner, L., Eds.; Plenum: New York, 2005.
- [19] Bennati, M.; Farrar, C. T.; Bryant, J. A.; Inati, S. J.; Weis, V.; Gergen, G. J.; Riggs-Gelasco, P.; Stubbe, J.; Griffin, R. G. *J. Magn. Res.* **1999**, *138*, 232–243.
- [20] Bennebroek, M.-T.; Schmidt, J. *J. Magn. Res.* **1997**, *128*, 199–206.
- [21] Bennati, M.; Hertel, M.; Fritscher, J.; Prisner, T. F.; Weiden, N.; Dinse, K. P.; Hofweber, R.; Spoerner, M.; Horn, G.; Kalbitzer, H. R. *Biochemistry* **2006**, *45*, 42–50.
- [22] Wittinghofer, A.; Waldmann, H. *Angew. Chem. Int. Ed.* **2000**, *39*, 4173–4390.
- [23] Barbacid, M. *Annu. Rev. Biochem.* **1987**, *56*, 779–827.
- [24] Pai, E. F.; Kregel, U.; Goody, R. S.; Kabsch, W.; Wittinghofer, A. *EMBO J.* **1990**, *9*, 2351–2359.
- [25] Tong, L.; deVos, A. M.; Milburn, M. V.; Brunger, A.; Kim, S.-H. *J. Mol. Biol.* **1991**, *217*, 503–516.
- [26] Kregel, U.; Schlichting, I.; Scherer, A.; Schumann, R.; Frech, M.; John, J.; Kabsch, W.; Pai, E. F.; Wittinghofer, A. *Cell* **1990**, *62*, 539–548.
- [27] Milburn, M. V.; Tong, L.; de Vos, A. M.; Brünger, A.; Yamaizumi, Z.; Nishimura, S.; Kim, S.-H. *Science* **1990**, *247*, 939–945.
- [28] Schlichting, I.; Almo, S. C.; Rapp, G.; Wilson, K.; Petratos, K.; Lentfer, A.; Wittinghofer, A.; Kabsch, W.; Pai, E. F.; Petsko, G.; Goody, R. S. *Nature* **1990**, *345*, 309–315.
- [29] Prive, G. G.; Milburn, M. V.; Tong, L.; de Vos, A. M.; Yamaizumi, Z.; Nishimura, S.; Kim, S.-H. *Proc. Natl. Acad. Sci. USA* **1992**, *89*, 3649–3653.
- [30] Wittinghofer, F.; Kregel, U.; John, J.; Kabsch, W.; Pai, E. F. *Environ. Health Perspect.* **1991**, *93*, 11–15.

- [31] Hall, B. E.; Bar-Sagi, D.; Nassar, N. *Proc. Natl. Acad. Sci. USA* **2002**, *99*, 12138–12142.
- [32] Rohrer, M.; Prisner, T.; Brüggmann, O.; Käss, H.; Spörner, M.; Wittinghofer, A.; Kalbitzer, H. R. *Biochemistry* **2001**, *40*, 1884–1889.
- [33] Halkides, C.; Farrar, C. T.; Larsen, R. G.; Redfield, A. G.; Singel, D. J. *Biochemistry* **1994**, *33*, 4019–4035.
- [34] Haller, M.; Hoffmann, U.; Schanding, T.; Goody, R. S.; Vogel, P. D. *J. Biol. Chem.* **1997**, *48*, 30103–30107.
- [35] Farrar, C. T.; Halkides, C. J.; Singel, D. J. *Structure* **1997**, *5*, 1055–1066.
- [36] Feuerstein, J.; Kalbitzer, H. R.; John, J.; Goody, R. S.; Wittinghofer, A. *Eur. J. Biochem.* **1987**, *162*, 49–55.
- [37] Smithers, G. W.; Poe, M.; Latwesen, D. G.; Reed, G. H. *Arch. Biochem. Biophys.* **1990**, *280*, 416–420.
- [38] Latwesen, D. G.; Poe, M.; Leigh, J. S.; Reed, G. H. *Biochemistry* **1992**, *31*, 4946–4950.
- [39] Larsen, R. G.; Halkides, C. J.; Redfield, A. G.; Singel, D. J. *J. Am. Chem. Soc.* **1992**, *114*, 9608–9611.
- [40] Halkides, C. J.; Farrar, C. T.; Redfield, A. G.; Singel, D. J. In *Biological Structure and Dynamics*, Vol. 1; Sarma, R. H.; Sarma, M. H., Eds.; Adenine Press: 1995.
- [41] Bellew, B.; Halkides, C. J.; Gerfen, G. J.; Griffin, R. G.; Singel, D. J. *Biochemistry* **1996**, *35*, 12186–12193.
- [42] Geyer, M.; Schweins, T.; Herrmann, C.; Prisner, T. F.; Wittinghofer, A.; Kalbitzer, H. R. *Biochemistry* **1996**, *35*, 10308–10320.

# Appendix A

## DFT Methods

All quantum chemical calculations were performed by J. Fritscher using unrestricted Kohn-Sham density functional theory (DFT) methods as implemented in Gaussian 03 (Frisch, M. J. et al. Gaussian 03, revision B.03; Gaussian Inc.: Pittsburgh, PA, 2003) and Q-Chem 2.0 (Q-Chem 2.0, Kong, J. et al., J. Comput. Chem. 2000, 21, 1532). All structure optimizations were carried out with Q-Chem employing the BP86 functional together with the 3-21G(d) basis set for all atoms. The structural models for the  $\text{Mn}^{2+}$  binding sites were generated using relevant parts of the crystal structures 1Q21 [25] and 5P21 [24] for the GDP- and GTP(GNP)-bound states, respectively, and replacing Mg by Mn as well as adding all necessary H atoms. The models consist of the  $\text{Mn}^{2+}$  ion, the directly bound water molecules, the di- or triphosphate chain of the GDP or GTP(GNP), the Ser17 residue and in the case of the GTP(GNP)-bound state also the directly ligated Thr35 residue. For these structures partial optimizations of the H atom positions were performed while all other atoms were kept fixed. For the computation of the hyperfine coupling tensors with Gaussian 03, the B3PW91 hybrid functional was chosen. A 9s7p4d basis set specially developed for the calculation of  $^{55}\text{Mn}$  hyperfine couplings (Munzarová, M. et al. J. Phys. Chem. 1999, 103, 9966) was used for Mn and the IGLO-II basis sets (Kutzelnigg, W. et al. in NMR - Basic Principles and Progress; Springer Verlag: Heidelberg, Germany, 1990; Vol. 23, p. 165ff) were used for all other atoms.



## Appendix B

### Frequency Dependence of VSWR

The frequency dependence of the voltage standing wave ratio (VSWR) of the RF transmission system was measured for different coil geometries with the ENDOR probe outside and inside the cryostat. The VSWR dependence on the frequency range measured outside the cryostat is shown in Figure B.1, for which a non-linear dependence of the VSWR was observed, similar as found inside the cryostat (data not shown). As predicted from the calculated reflection coefficient via Equation 5.2, at high frequencies as well as for an increasing number of turns an increase in the VSWR is observed. However, at frequencies below 100 MHz, the VSWR is still well below 1.5, such that for future ENDOR experiments with low- $\gamma$  nuclei, more turns appear to be suitable. In contrast, for high frequencies, a compromise between minimum VSWR and maximum  $\mathbf{B}_2$  yielded an optimum ENDOR effect using a 4.5-turn flat coil with 0.5 mm wire width.

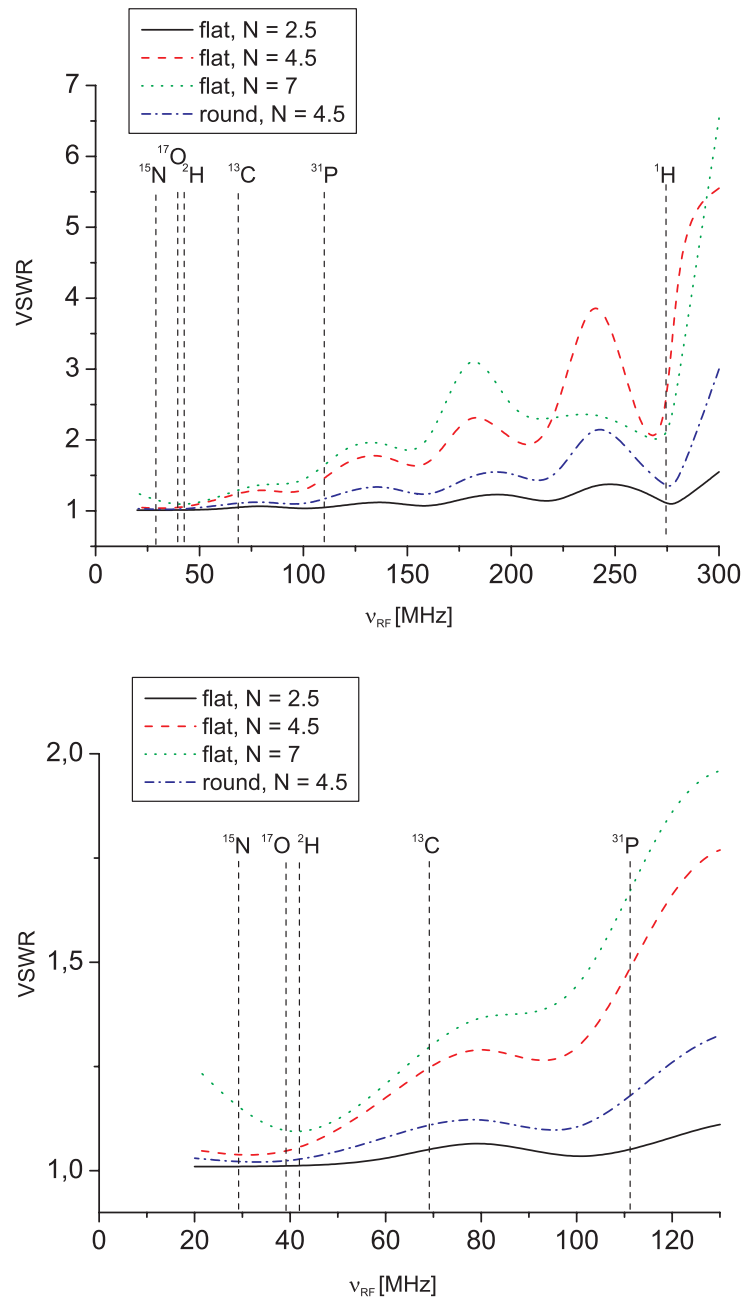


**Figure B.1** Measured voltage standing wave ratios (VSWRs) of three flat and one round coil, with different numbers of turns, in dependence of the RF frequency from 20–300 MHz (top) and from 20–130 MHz, the low- $\gamma$  frequency range (bottom). Indicated with the dotted lines are the frequencies of selected nuclei.

# Appendix C

## Supporting Information for BCR Studies

### Comparison of X- and Q-Band Samples

In order to find out whether the X-band samples contain the same (contribution of) species as the Q-band samples and therefore to estimate to which extent the observations at X- and Q-band can be compared with each other, the Q-band samples were measured at X-band at 20 K as shown in Figure C.1.

### Comparison of Spectra From BCR Reduced With Different Amounts of Dithionite

Similar as found for the  $^{33}\text{S}$ -labeled enzyme, the spectra of the unlabeled enzyme reduced with one equivalent of dithionite showed an increased contribution of the  $g = 2.035$  signal (at 10 K, with respect to the  $g = 2.025$  signal), as well an increased signal intensity at  $g = 2.030$  (at 30 K, with respect to the 2.006 signal) as observable in Figure C.2. The subtraction of the spectrum from BCR reduced with 0.5 equivalents of dithionite from the one of the enzyme reduced with one equivalent of dithionite at 20 K, yields a spectrum with singularities at  $g = 2.036$ ,  $g = 2.024$ ,  $g = 2.010$  and a minor shoulder at  $g = 2.017$  as indicated in the bottom graph.

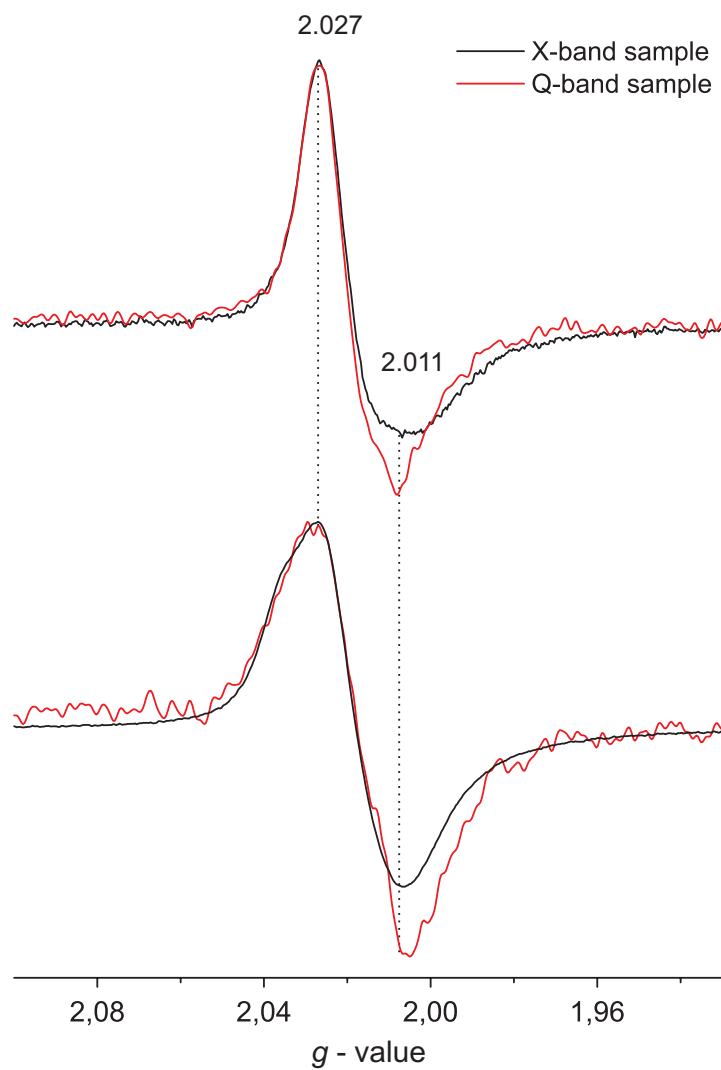


**Figure C.1** Comparison of CW X-band EPR signals at 20 K obtained from X- and Q-band samples containing the unlabeled (top) and <sup>33</sup>S-labeled (bottom) enzyme measured under equivalent experimental conditions as used in Figure 3.5.



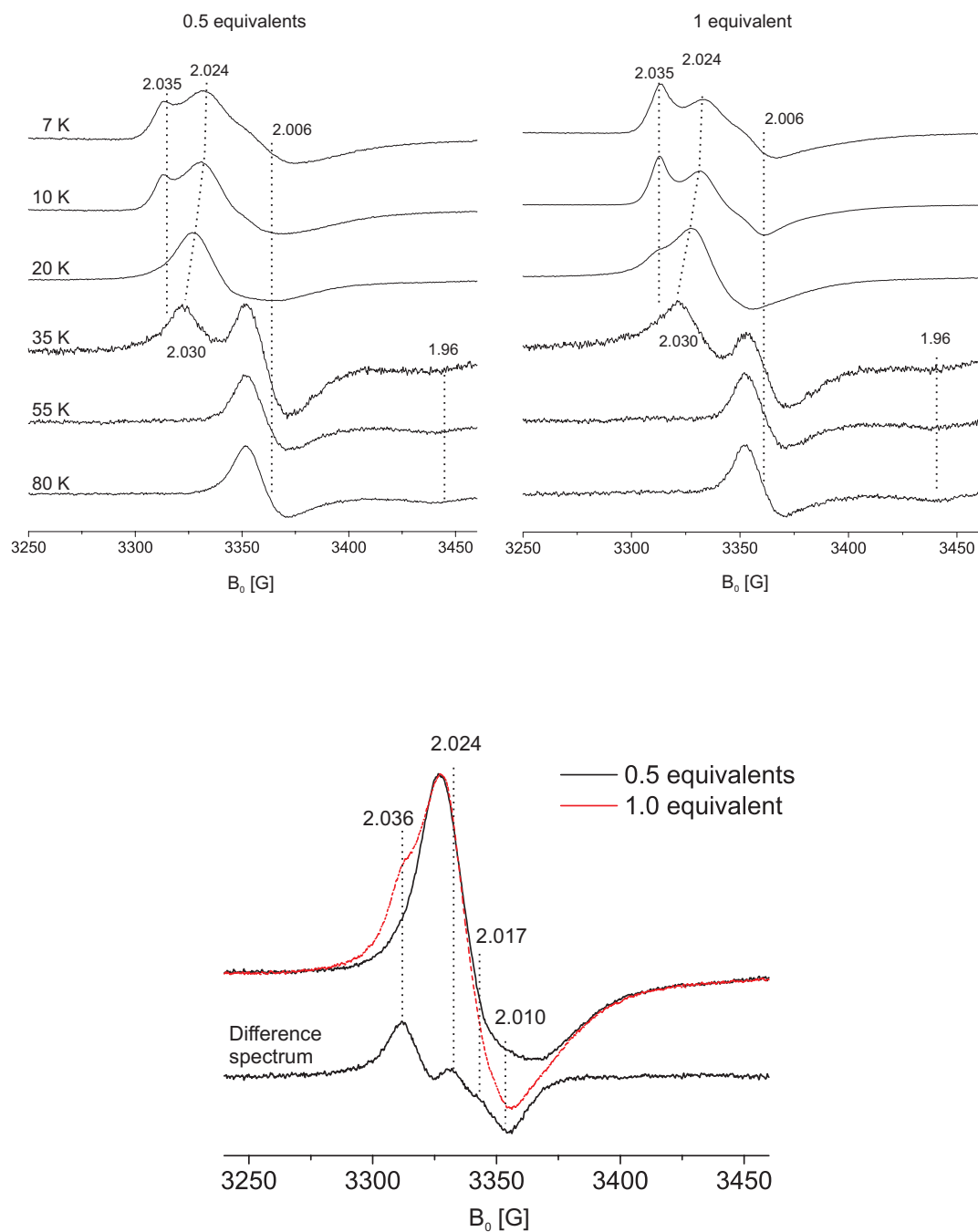


**Figure C.2** Top: Comparison of temperature-dependent X-band EPR spectra from the unlabeled enzyme reduced with 0.5 equivalents of dithionite (left) and one equivalent of dithionite (right). Bottom: Subtraction of the spectrum from BCR reduced with 0.5 equivalents of dithionite from the one of the enzyme reduced with one equivalent of dithionite at 20 K, yielding a spectrum with singularities at  $g = 2.036$ ,  $g = 2.024$ ,  $g = 2.010$  and a minor shoulder at  $g = 2.017$  as indicated. For experimental details see Figure 3.3.



# List of Figures

1.1	Enzymatic reactions involved in phenol metabolism. . . . .	2
1.2	Ribbon plot of wild-type Ras in the triphosphate form with the GTP analogue GppNHp according to X-ray data. . . . .	5
2.1	Energy levels EPR and ENDOR spectra. . . . .	20
2.2	Energy level diagram of Mn(II). . . . .	22
2.3	Pulse sequences for separating EPR signals. . . . .	24
2.4	Mims and Davies ENDOR pulse sequences. . . . .	25
3.1	Chemical and biological Birch reduction. . . . .	29
3.2	Pulsed G-band EPR spectrum of unlabeled BCR. . . . .	35
3.3	Temperature-dependent CW X-Band EPR spectra of unlabeled and <sup>33</sup> S-labeled BCR. . . . .	36
3.4	Deconvolution of CW X-band EPR spectra from unlabeled and <sup>33</sup> S-labeled BCR at 20 K. . . . .	39
3.5	Temperature-dependent CW and pulsed Q-band EPR spectra from unlabeled and <sup>33</sup> S-labeled BCR. . . . .	40
3.6	CW and pulsed Q-Band EPR spectra from unlabeled and <sup>33</sup> S-labeled BCR. . . . .	42
3.7	Simulation of X- and Q-band EPR spectra from unlabeled BCR. . . . .	44
3.8	Simulation of X- and Q-band EPR spectra from <sup>33</sup> S-labeled BCR. . . . .	46
3.9	Sum of 45 K spectrum from <sup>33</sup> S-labeled BCR and 20 K spectrum of the unlabeled enzyme. . . . .	48
3.10	CW X-band EPR spectra from unlabeled and <sup>33</sup> S-labeled BCR at different temperatures. . . . .	50
3.11	CW X-band, pulsed Q- and G-band spectra from unlabeled BCR . . . . .	52
4.1	Activation and deactivation cycle of Ras. . . . .	61

---

4.2	Switch I and switch II regions in Ras(wt)•GppNHp, Ras(wt)-GppNHp•Raf and Ras•GDP according to X-ray data. . . . .	62
4.3	Nucleotide binding site of Ras(wt)•GppNHp and Ras(wt)•GDP. . . . .	63
4.4	Comparison of <sup>31</sup> P-Davies ENDOR spectra from Ras(wt)•GppNHp and Ras(wt)•Mn <sup>2+</sup> •GDP. . . . .	70
4.5	<sup>13</sup> C-Mims ENDOR spectra of uniformly <sup>13</sup> C-labeled and of selectively 1,4- <sup>13</sup> C- aspartate labeled Ras(wt)•GDP. . . . .	72
4.6	<sup>13</sup> C-Mims ENDOR spectra of uniformly <sup>13</sup> C-labeled wild-type Ras-GDP and its oncogenic mutant G12V as well as of Ras(wt)•Raf-GppNHp. . . . .	74
5.1	Schematic drawing of the 180 GHz ENDOR cavity holder. . . . .	88
5.2	Schematic drawing of the ENDOR resonator. . . . .	89
5.3	Design of the radio frequency coil. . . . .	90
5.4	Schematic drawing of the radio frequency transmitter unit. . . . .	93
5.5	<sup>1</sup> H-Mims and Davies G-band ENDOR spectra of BDPA. . . . .	94
5.6	<sup>1</sup> H-Mims and Davies G-band ENDOR spectra of Ras•Mn <sup>2+</sup> •GDP. . . . .	96
5.7	<sup>1</sup> H-Mims G-band ENDOR spectra of Ras•Mn <sup>2+</sup> •GDP dissolved in H <sub>2</sub> O and D <sub>2</sub> O. . . . .	97
B.1	Frequency dependence of voltage standing wave ratio. . . . .	118
C.1	CW X-band EPR spectra at 20 K from X- and Q-band samples. . . . .	120
C.2	Temperature-dependent CW X-band EPR spectra from unlabeled BCR reduced with 0.5 and 1.0 equivalents of dithionite. . . . .	121

# List of Tables

3.1	Literature $g$ - and hyperfine tensor components for disulfide radical anions. . . . .	45
4.1	Hyperfine tensor components obtained from $^{31}\text{P}$ -ENDOR studies of Ras(wt)•GDP and Ras(wt)•GppNHp. . . . .	70
4.2	Hyperfine tensor components obtained from $^{13}\text{C}$ -ENDOR studies of Ras•GDP and Ras•Raf•GppNHp complexes . . . . .	73





## Abbreviations

4-F-BCoA	4-fluorobenzoyl-CoA
ADP	adenosin diphosphate
ATP	adenosin triphosphate
BCoA	benzoyl-CoA
BCR	benzoyl-CoA reductase
BDPA	bisdiphenylene-phenyl-allyl
BP	Breit–Pauli
CW	continuous-wave
<i>D</i>	axial ZFS term
DFT	density functional theory
DPPH	2,2-diphenyl-1-picrylhydrazyl
<i>E</i>	rhombic ZFS term
ELDOR	electron–electron double resonance
ENDOR	electron–nuclear double resonance
EPR	electron paramagnetic resonance
ESEEM	electron spin-echo envelope modulation
FADH	reduced product of flavin adenine dinucleotide
FTIR	Fourier-transform infra-red
G12V	mutation of glycine 12 from Ras to valine
GAP	GTPase-activating protein
GD(T)P	guanosine-5'-di(tri)phosphate
GEF	guanine nucleotide exchange factor
GNP	guanosine-di/tri-phosphate
GNBP	guanosine-nucleotide binding protein
GppCH <sub>2</sub> p	guanosine-5'-( $\beta,\gamma$ -methylene)triphosphate
GppNHp	guanosine-5'-( $\beta,\gamma$ -imido)triphosphate
GTP	guanosine-5'-triphosphate



---

G-band	180 GHz
H-ras	Harvey ras
HF	high-field
HFC	hyperfine coupling
HYSCORE	hyperfine sublevel correlation
IGLO	individual gauge for localized orbitals
IR	infra-red
MD	molecular dynamics
MgADP	magnesium adenosine diphosphate
M-ras	Muscle ras
MW	microwave
NMR	nuclear magnetic resonance
PI(3)K	phosphatidylinositol 3-kinase
Q-band	34 GHz
Raf gene	regulation of alpha-fetoprotein gene
Raf	c-Raf kinase protein
RalGDS	guanine nucleotide dissociation stimulator of the small GTPase Ral
Ras	protein product of human H-Ras (rat sarcoma)
RBD	Ras binding domain of the effector molecule
REFINE	relaxation filtered hyperfine
RF	radiofrequency
RFQ	rapid freeze-quenche
RhoA	product of rhoA gene
RNA	ribonucleic acid
RNR	ribonucleotide reductase
SF	stopped-flow
SH	spin Hamiltonian
SoS	Son of the sevenless
SRT	shot repetition time
UV-Vis	ultra-violet/visible
wt	wild-type
W-band	94 GHz
X-band	9 GHz
ZFS	zero-field splitting



# Acknowledgment

At this place I would like to thank all the people who have contributed to enable this work and supported me throughout my PhD.

First of all, I wish to thank Prof. Thomas F. Prisner for providing me with the opportunity to work in his group as well as for giving me two very interesting projects to work on. It was a pleasure to work in such a well equipped laboratory.

Furthermore, I am very grateful to Dr. Marina Bennati for her motivating support throughout my PhD, for giving me another very interesting biological project to work on, for the help with the ENDOR setup, in particular during the beginning phase of the setup, and for many helpful and interesting discussions about ENDOR and more. Also, I have to thank her for organizing financial support during parts of my PhD.

The ENDOR setup wouldn't have been running as it is today without the help of several people. Foremost, I wish to thank Dr. Vasyl Denysenkov for his collaboration and great support as well as for helping out with any problems on the spectrometer at any time. Mr. Jäger and Mr. Van Tankeren from the mechanical workshop are thanked for making the ENDOR resonators and for implementing the changes in the ENDOR probehead. Bernhard Kinzer and Bernhard Thiem are thanked for technical support with the equipment.

The Ras project was performed in collaboration with Dr. Norbert Weiden from the group of Prof. Klaus Peter Dinse from the University of Darmstadt, as well as with the group of Prof. Hans-Robert Kalbitzer from the University of Regensburg. Dr. Norbert Weiden is thanked for his help with the ENDOR measurements on the Ras protein. Measuring with him was always very stimulating. From the group of Prof. Hans-Robert Kalbitzer I wish to thank Dr. Michael Spörner not only for preparing and providing the Ras samples very reliable and promptly, but also for many interesting discussions about Ras on the phone and via email and for always being willing to answer any biological or biochemical

question. Furthermore, Roland Hofweber is thanked for preparing the selectively  $^{13}\text{C}$ -aspartate-labeled samples. Thank you also to Jörg Fritscher for performing the DFT calculations.

The BCR samples were prepared in the group of Prof. Matthias Boll to whom I wish to thank as well as to the PhD students who prepared the samples, which are Dr. Henrik Möbitz and Jörg Johannes. Furthermore, thanks goes also to the people who have helped to measure the Q-band spectra: Dr. Pat Carl, Dr. Peter Höfer and Silke Kummer from Bruker Biospin GmbH, as well as Dr. Christian Teutloff from the group of Prof. Robert Bittl from the Free University of Berlin.

Furthermore, I wish to thank Jörg Fritscher and Dr. Thorsten Maly for many inspiring discussions about EPR theory, computer networks and mensa desserts. Jörg Fritscher is further thanked for his detailed and prompt corrections of my thesis and for his constructive criticism. Thanks also to Thorsten Maly for introducing me to Matlab and to Offenbach. Sevdalina Lyubenova is thanked for many helpful discussions of biochemical nature and about how to treat biological samples, as well as for many enjoyable evenings on the balcony.

Thanks also to Dr. Oliver Brüggemann for introducing me into the high-field lab and some tricks on the spectrometer in the beginning. Further I wish to thank Dr. Raanan Carmieli for many fruitful discussions about ENDOR experiments in particular on Mn(II).

Natalie Kisseleva and Dr. Vasyl Denysenkov are thanked for the Russian and most pleasant atmosphere in the office, and for teaching me some basics of the Russian language and culture.

The remaining group members are thanked for the good working atmosphere: Bela Bode, Adrian Cernescu, Dr. Burkhardt Endeward, Dr. Emiliano Feresin, Susanna Frtus, Dr. Stéphane Grimaldi, Sigrid Kämmerer, Hildegard Matthis, Dominik Margraf, Dr. Fraser MacMillan, Astrid Noll, Dr. Olav Schiemann, Dr. Jörn Plackmayer and Marloes Penning de Vries.

Finally, I wish to thank my parents, Erika and Ingolf Hertel, for their loving support throughout the years.

# Curriculum Vitae

## Persönliche Daten

Name	Melanie Hertel
Nationalität	Deutsch
Geburtsdatum	17.08.1976
Geburtsort	Kaiserslautern
Eltern	Ingolf und Erika Hertel, geb. Schneppat
Familienstand	Ledig

## Hochschulstudium

Seit Febr. 2002	Doktorarbeit Physikalische Chemie an der J.W.Goethe-Universität Frankfurt a. M., bei Prof. T.F. Prisner.
Jan. 2002	Physikdiplom an der Freien Universität (FU) Berlin
2000 – 2001	Auslandsstudium und experimentelle Diplomarbeit an der University of Oxford, UK, bei Prof. P. Hore, externe Betreuung durch Prof. K. Möbius, FU Berlin auf dem Gebiet der Kernmagnetischen Resonanz (NMR). Thema: A CIDNP study of the tryptophan radical.
1996 – 2002	Physikstudium an der FU Berlin
1995	Französischstudium an der FU Berlin

## Schulische Ausbildung

Juni 1995	Allgemeine Hochschulreife
1992 – 1995	Canisius Kolleg, Berlin-Tiergarten
1990	College Alain-Fournier, Orsay, Frankreich

---

1987 – 1992	Kolleg St. Sebastian, Stegen bei Freiburg i. Brsg.
1986 – 1987	Heese-Gymnasium, Berlin-Steglitz
1983 – 1984	Table Mesa Elementary School, Boulder, USA
1982 – 1986	Erich-Kästner Grundschule, Berlin-Dahlem

### Academic Teachers

M. Bennati, A. Fring, F. Forstmann, H. Gabriel, B. Hamprecht, M. P. Heyn, P. J. Hore, M. Karowski, V. Linke, J. J. Lopez, K. Möbius, T.-C. Meng, K. Starke, T. F. Prisner, R. Schrader, D. Stehlik, C. Timmel, D. Quitmann

### Veröffentlichungen

1. Bennati, M.; Hertel, M. M.; Fritscher, J.; Prisner, T. F.; Weiden, N.; Hofweber, R.; Spörner, M.; Horn, G.; Kalbitzer, H.-R. *Biochemistry* **2006**, *45*, 42–50.
2. Hertel, M. M.; Denysenkov, V. P.; Bennati, M., Prisner, T. P. *Magn. Reson. Chem.* **2005**, *43*, 248–255.
3. Spörner, M.; Prisner, T. F.; Bennati, M.; Hertel, M. M.; Weiden, N.; Schweins, T.; Kalbitzer, H. R. *Magn. Reson. Chem.* **2005**, *43*, 74–83.
4. Arieli, D.; Prisner, T. P.; Hertel, M.; Goldfarb, D. *Phys. Chem. Chem. Phys.* **2004**, *6*, 172–181.